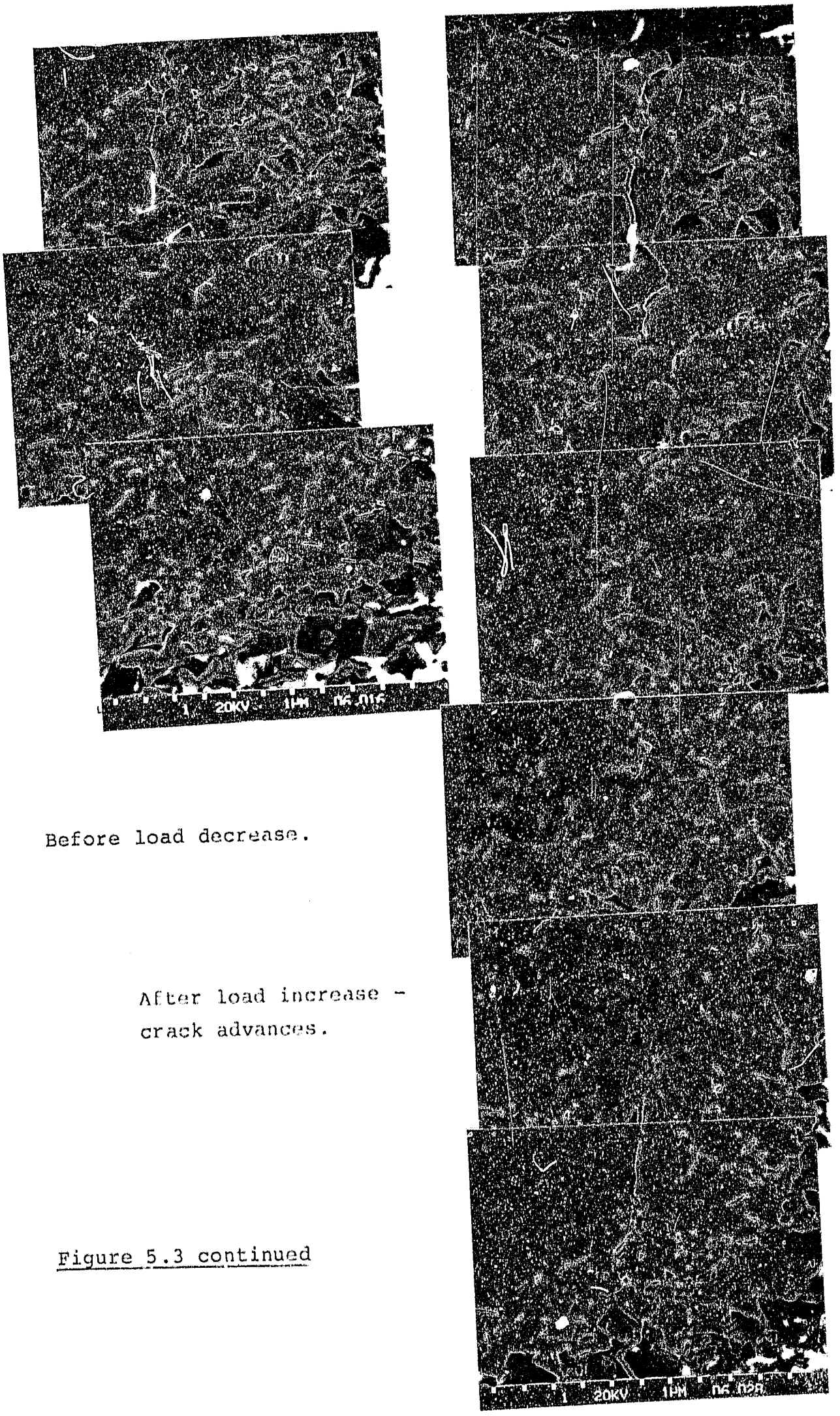

Before load decrease.

After load increase - crack advances.

Figure 5.3 continued

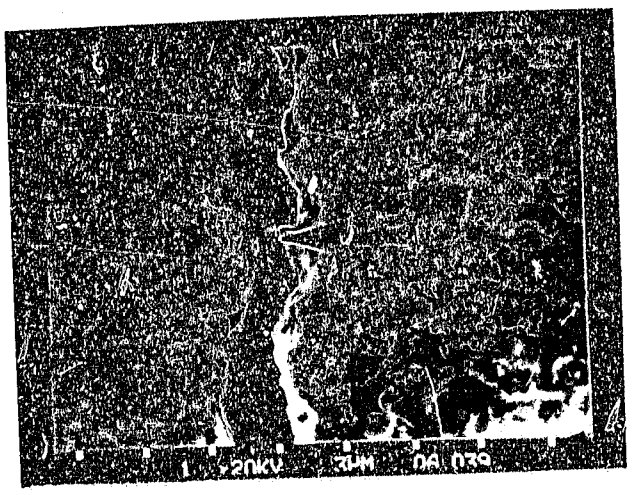

(a) Load applied

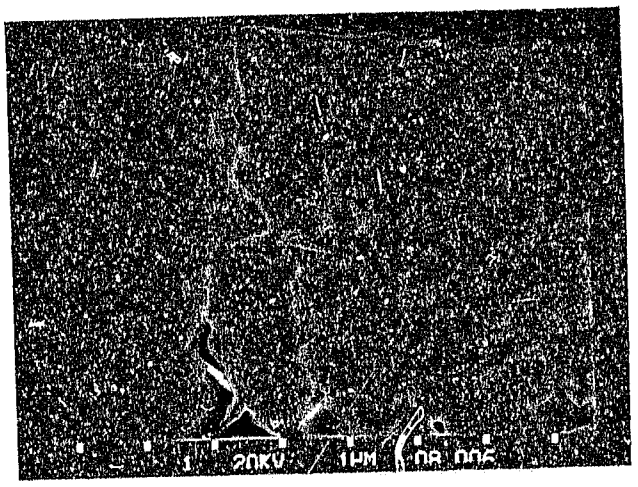

(a) Load applied

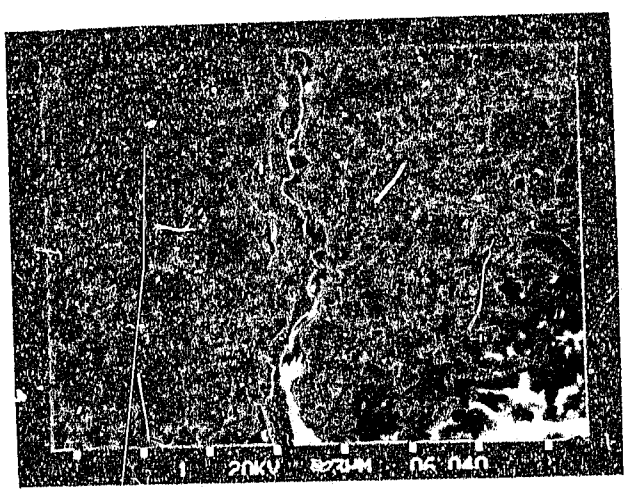

(b) No load, crack opening reduced but not closed

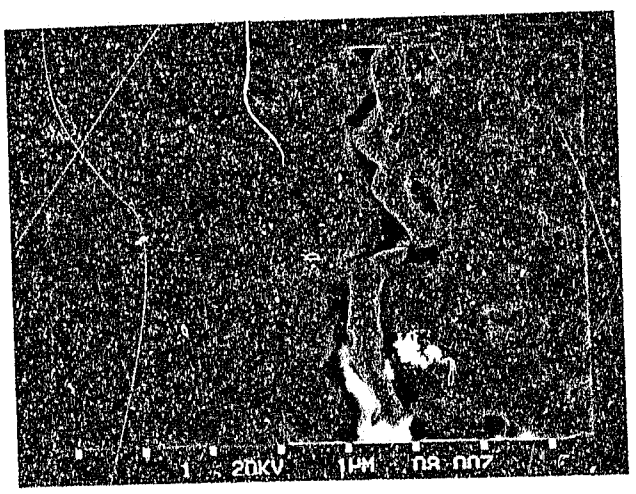

(b) No load, crack opening reduced but not closed

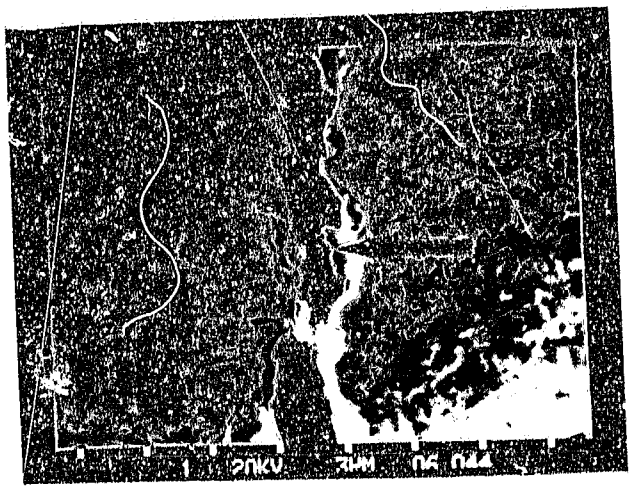

(c) Load reapplied

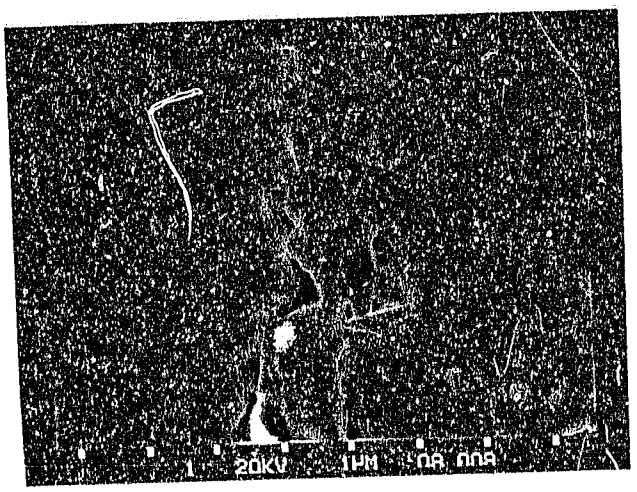

(c) Load reapplied

Figure 5.4

Figure 5.5

(a) Load applied

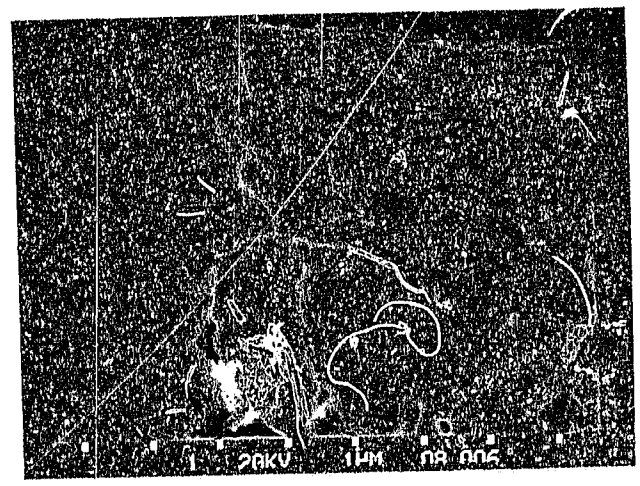

(a) Load applied

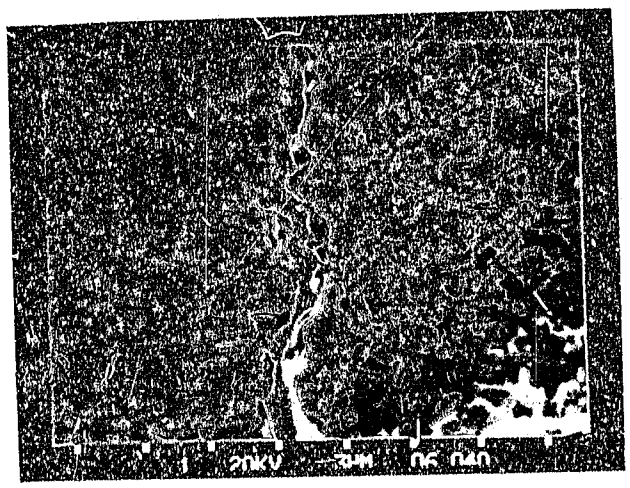

(b) No load, crack opening reduced but not closed

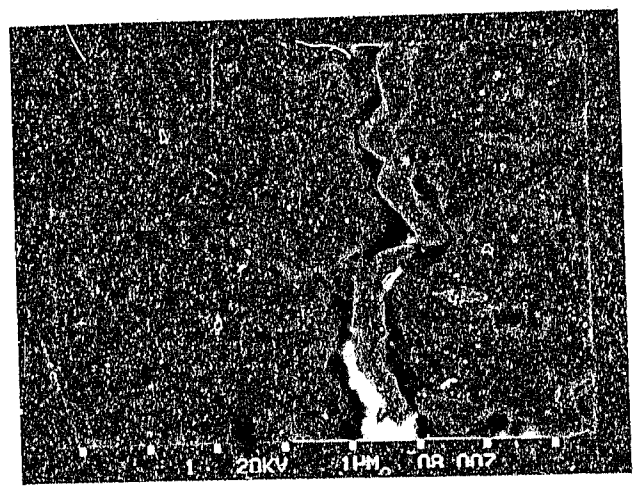

(b) No load, crack opening reduced but not closed

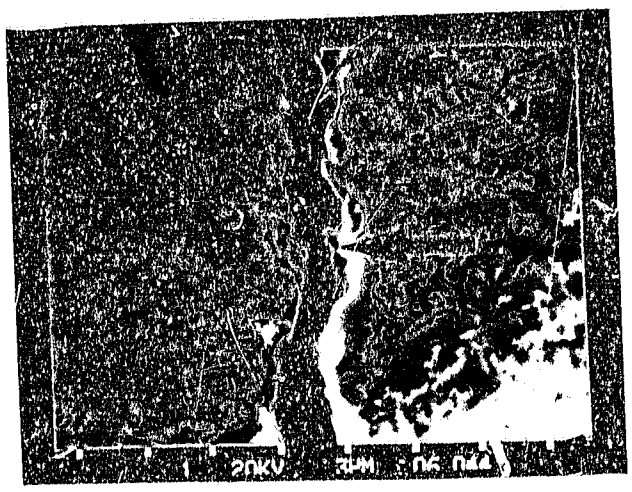

(c) Load reapplied

Figure 5.4

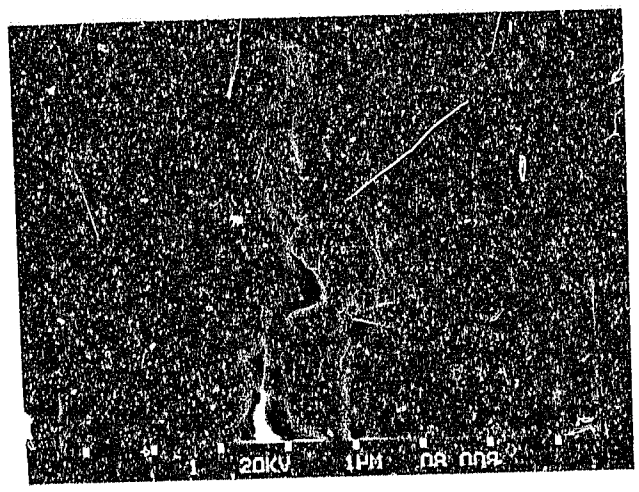

(c) Load reapplied

Figure 5.5

5.2 FATIGUE

Extensive fatigue testing of the tungsten carbide-cobalt alloys has produced da/dN vs ΔK_I curves for a wide range of load conditions. The effects of: mean stress intensity (K_{Iav}), stress intensity amplitude (ΔK_I), R ratio (K_{Imin}/K_{Imax}) frequency, temperature, carbide grain size ($\bar{d}$), and cobalt content have been investigated. Most of the results obtained can be adequately summarised graphically.

5.2.1 Fatigue Crack Growth Rates for R Ratio < 0,1

In many applications of WC-Co alloy components (drill bits, dies, anvils, rolls, etc.) the load is either on or off i.e. an R ratio (P_{min}/P_{max}) of zero. In the first series of tests a low R ratio was selected so that crack growth effects observed would be consistent with those expected under conditions commonly encountered in practice.

When using the double torsion test it is undesirable to have impacting of the load points which may cause the specimen to shift out of alignment. A constant minimum load of 0,1 kN was therefore maintained while the maximum was varied to obtain the stress intensity range required, giving an R ratio less than 0,1, (actual values 0,03 - 0,08).

The 'constant K' characteristic of the double torsion geometry enabled numerous results to be obtained from one specimen.

The crack growth rates for the range of alloys investigated are summarised in Figure 5.6. (The individual graphs and data points are given in Appendix 6). In order to avoid confusion and crowding of the graph the results for alloy G6 are not included, however the curve fits between the G10 and GJ0 data as would be

expected.

It is immediately obvious that as the cobalt content and carbide grain size increase, the corresponding fatigue resistance increases. Hence, for a particular stress intensity range, ($R < 0,1$), the crack growth rate decreases as the mean free path increases. (Figures 5.7 - 5.9). In addition it is clear that the value of the exponent 'm' decreases as the mean free path increases. (Figure 5.10).

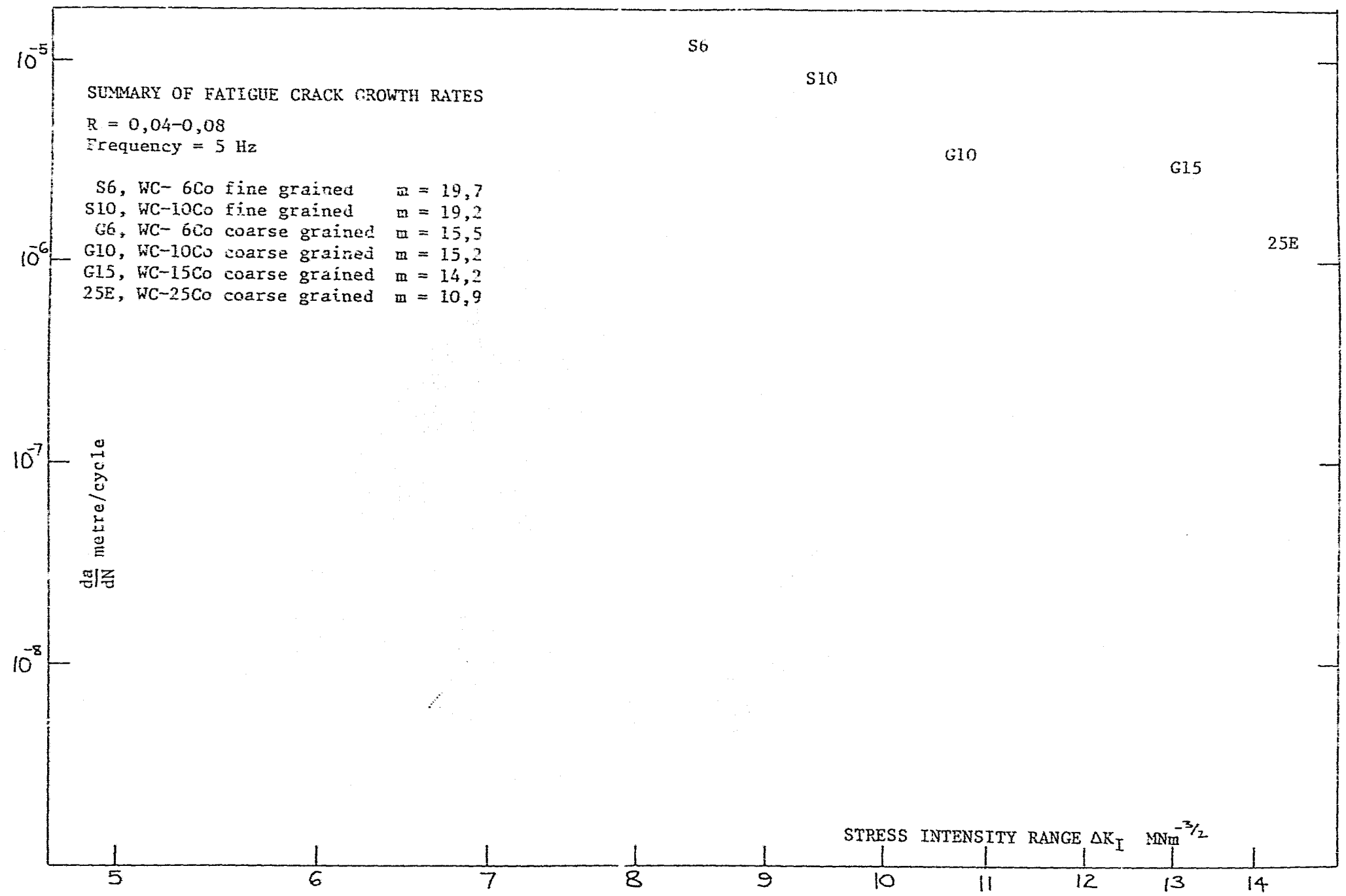
SUMMARY OF FATIGUE CRACK GROWTH RATES
R = 0,04-0,08
Frequency = 5 Hz
S6, WC- 6Co fine grained m = 19,7
S10, WC-10Co fine grained m = 19,2
G6, WC- 6Co coarse grained m = 15,5
G10, WC-10Co coarse grained m = 15,2
G15, WC-15Co coarse grained m = 14,2
25E, WC-25Co coarse grained m = 10,9
S6
S10
G10
G15
25E
10^{-5}
10^{-6}
10^{-7}
10^{-8}
$\frac{da}{dN}$ metre/cycle
STRESS INTENSITY RANGE ΔK_I $MNm^{-3/2}$
5
6
7
8
9
10
11
12
13
14

Figure 5.6

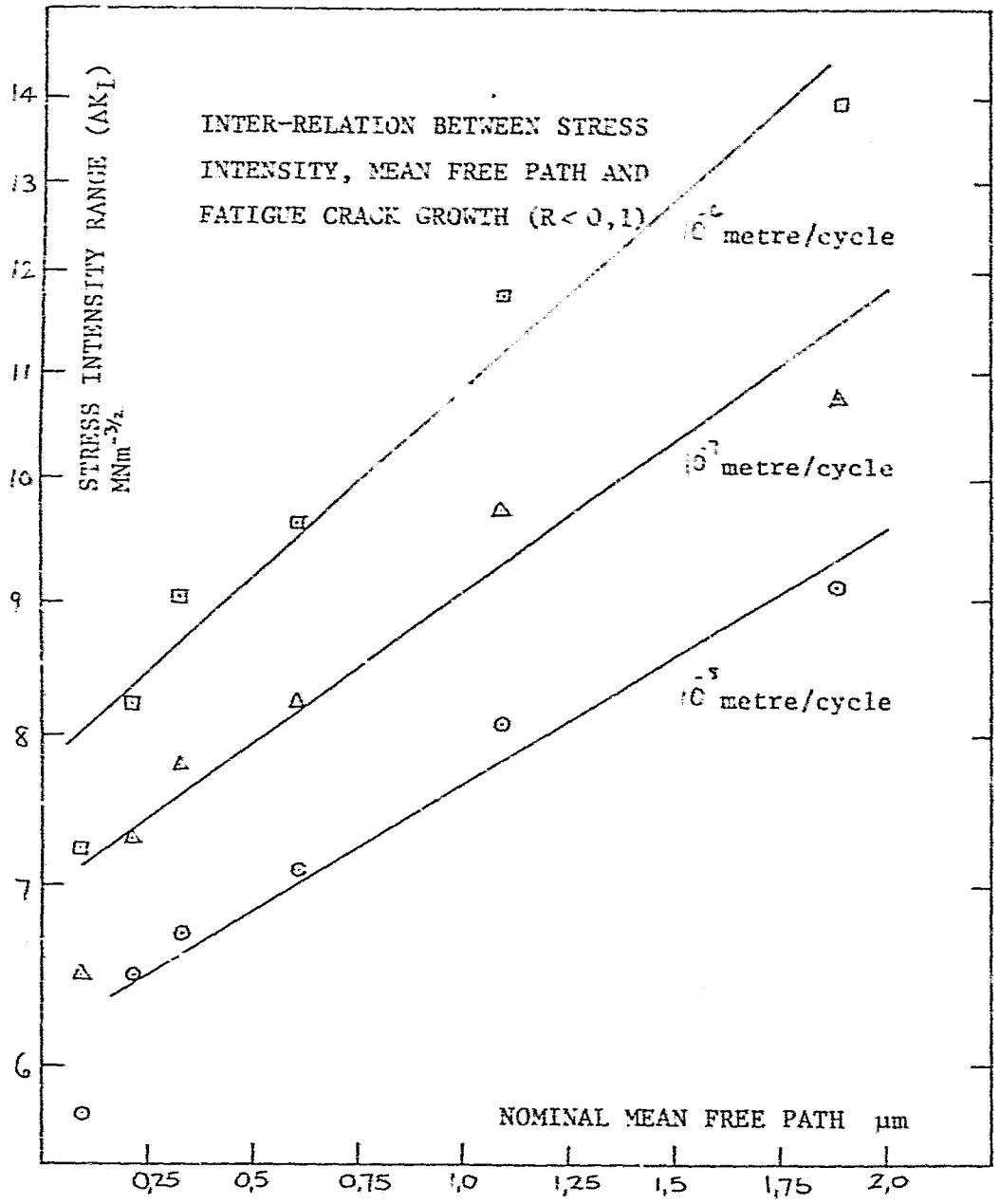

Figure 5.7

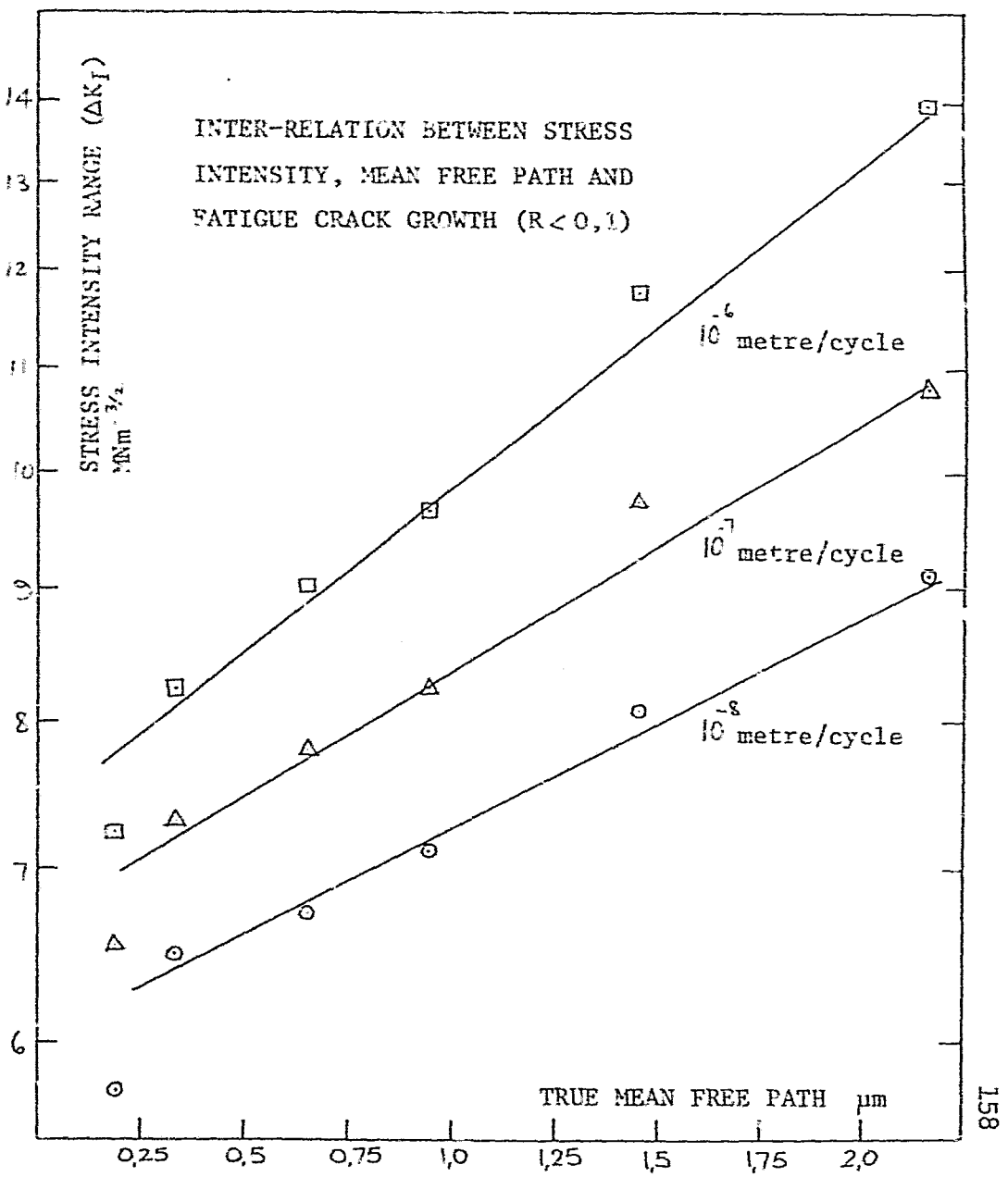

Figure 5.8

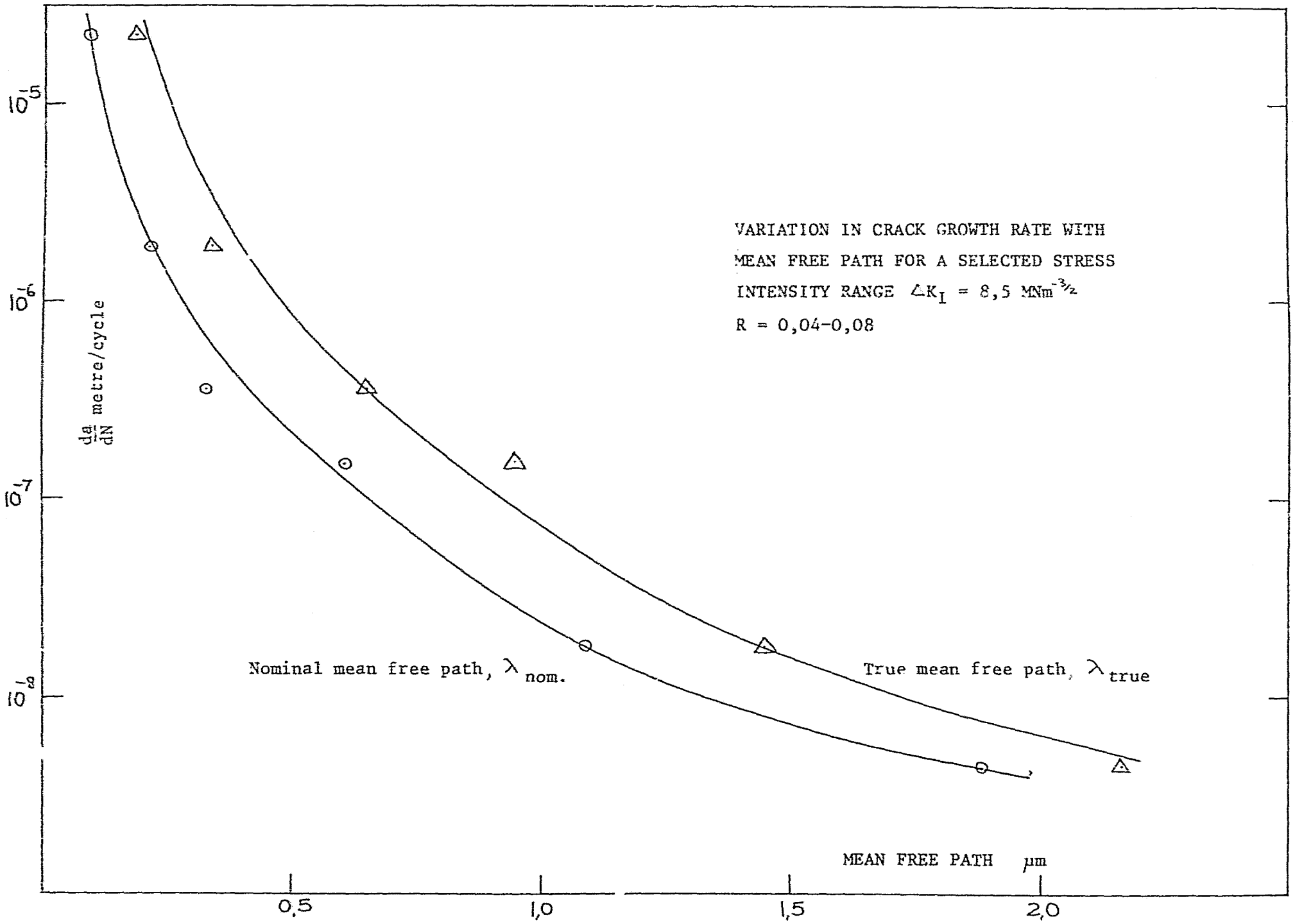
VARIATION IN CRACK GROWTH RATE WITH
MEAN FREE PATH FOR A SELECTED STRESS
INTENSITY RANGE ΔK_I = 8,5 $MNm^{-3/2}$
R = 0,04-0,08
10^{-5}
10^{-6}
10^{-7}
10^{-8}
$\frac{da}{dN}$ metre/cycle
Nominal mean free path, $\lambda_{nom.}$
True mean free path, λ_{true}
MEAN FREE PATH μm
0,5
1,0
1,5
2,0

Figure 5.9

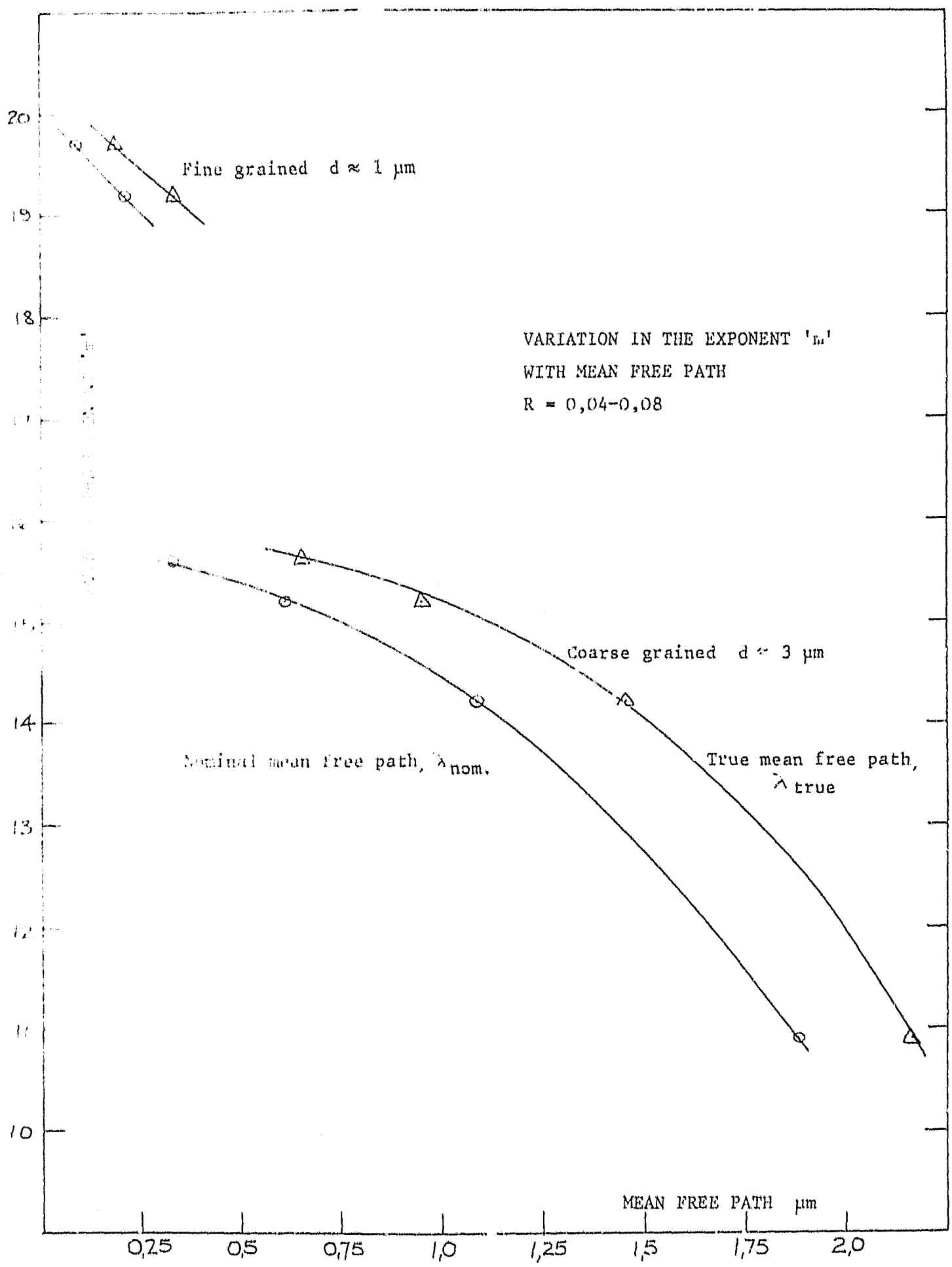
Fine grained d ≈ 1 μm
VARIATION IN THE EXPONENT 'n'
WITH MEAN FREE PATH
R = 0,04-0,08
Coarse grained d ≈ 3 μm
Nominal mean free path, λnom.
True mean free path,
λ true
20
19
18
17
16
15
14
13
12
11
10
MEAN FREE PATH μm
0,25
0,5
0,75
1,0
1,25
1,5
1,75
2,0

Figure 5.10

5.2.2 Fatigue at Constant Mean Stress Intensity

Fatigue testing at an R value less than 0,1 may represent industrial applications most accurately but it does not provide useful mechanistic information. In order to maintain a constant R value both the stress intensity range and the mean stress intensity are increased, the individual influences of ΔK_I and K_{Iav} are not isolated.

In an attempt to determine the mechanisms of fatigue crack growth in WC-Co alloys tests have been carried out on three alloys, S10, G6 and G10 at a constant average stress intensity with stress intensity range increasing (K_{Iav} constant, ΔK_I increasing). The load ranges used are summarised schematically in Figures 5.11, 5.12.

Crack growth rates in the alloys tested increase as the stress intensity range increases, and are mean stress intensity dependent (Figures 5.13,5.14 and 5.15). Most significant is the result that the exponent 'm' in the Paris 'law' increases with increasing K_{Iav}. The tests carried out on the G10 alloy (2 specimens used) show that below a certain mean stress intensity 'm' remains constant. This is supported by the results from the S10 and G6 alloys although less data were obtained for these two alloys. (Figures 5.16 - 5.18).

It is probable that 'm' starts increasing when the peak stress intensity (K_{Imax}) is sufficiently large to enter the regime of static crack growth. (Figures 5.11,5.12). (Static crack growth tests have not been carried out on G6).

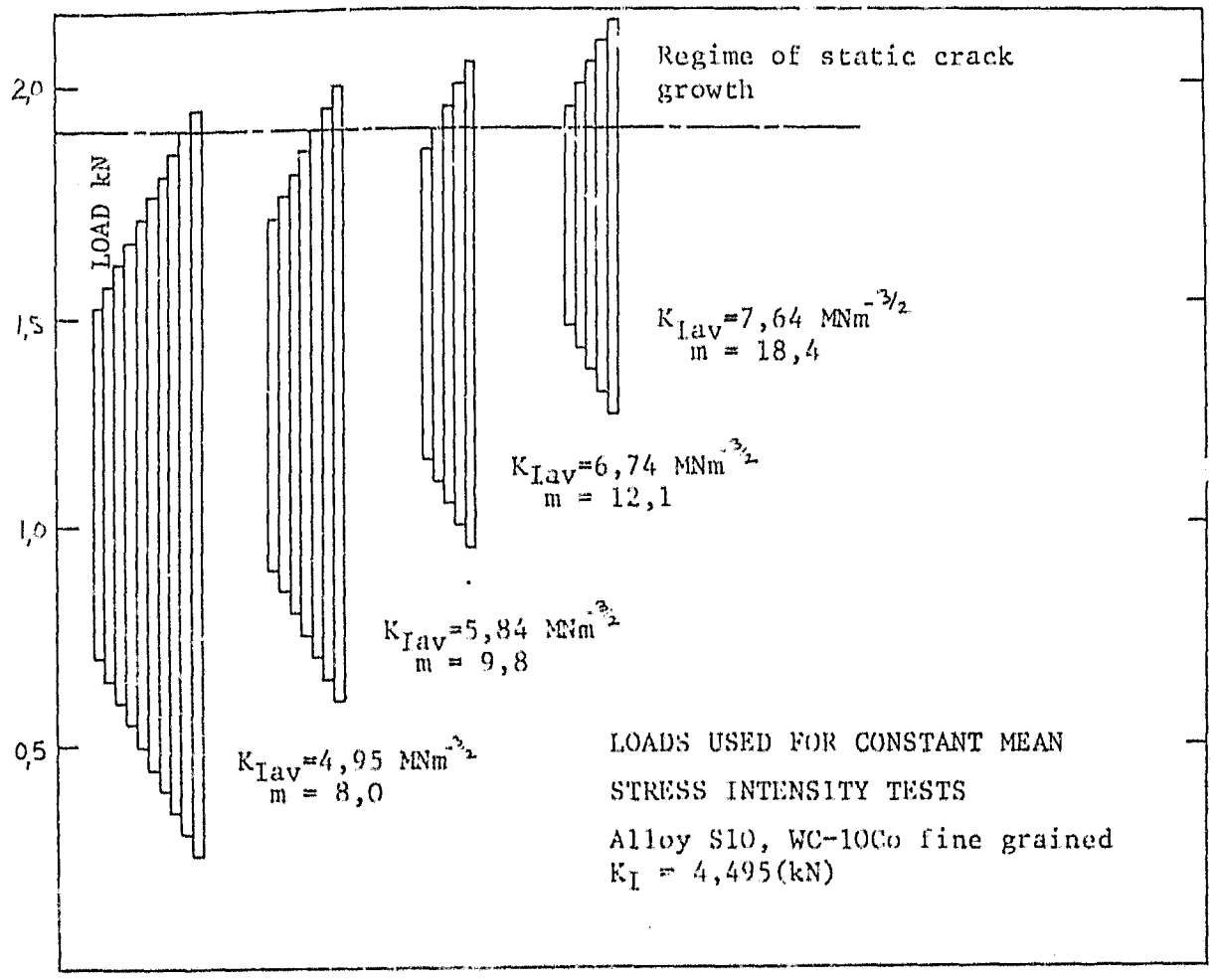

Figure 5.11

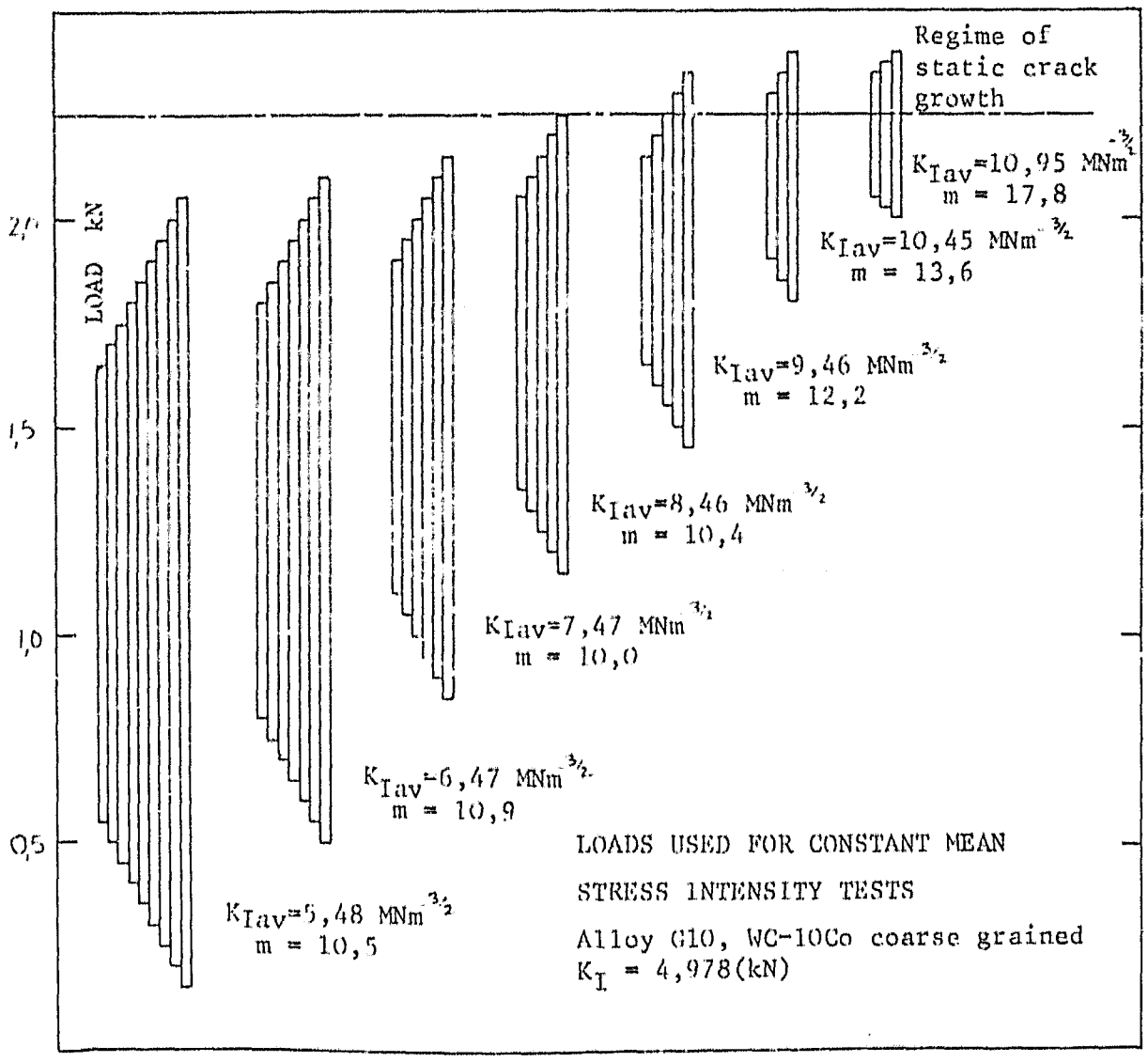

Figure 5.12

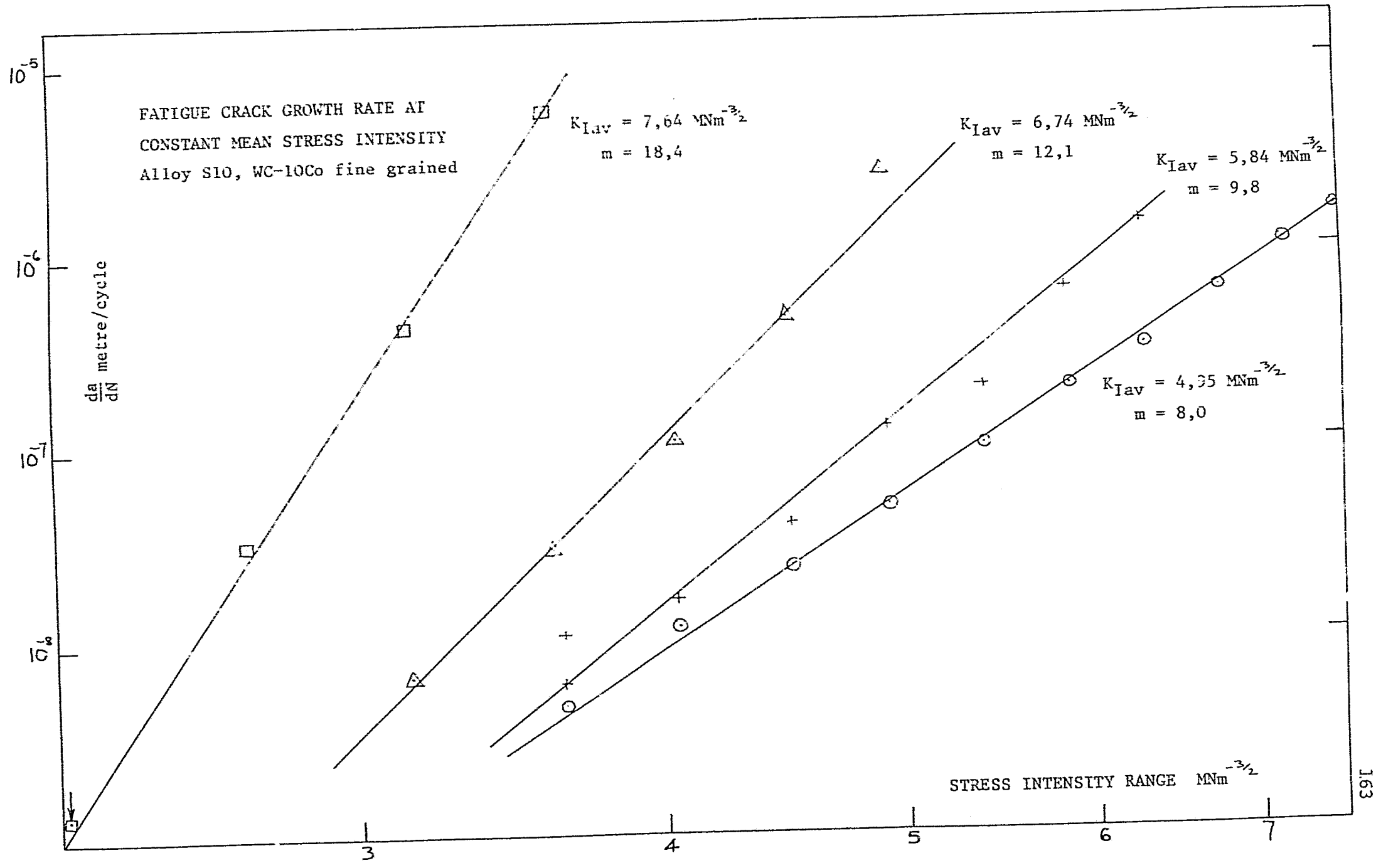
FATIGUE CRACK GROWTH RATE AT
CONSTANT MEAN STRESS INTENSITY
Alloy S10, WC-10Co fine grained
K_{Iav} = 7,64 $MNm^{-3/2}$
m = 18,4
K_{Iav} = 6,74 $MNm^{-3/2}$
m = 12,1
K_{Iav} = 5,84 $MNm^{-3/2}$
m = 9,8
K_{Iav} = 4,95 $MNm^{-3/2}$
m = 8,0
10^{-5}
10^{-6}
10^{-7}
10^{-8}
$\frac{da}{dN}$ metre/cycle
STRESS INTENSITY RANGE $MNm^{-3/2}$
3
4
5
6
7
163

Figure 5.13

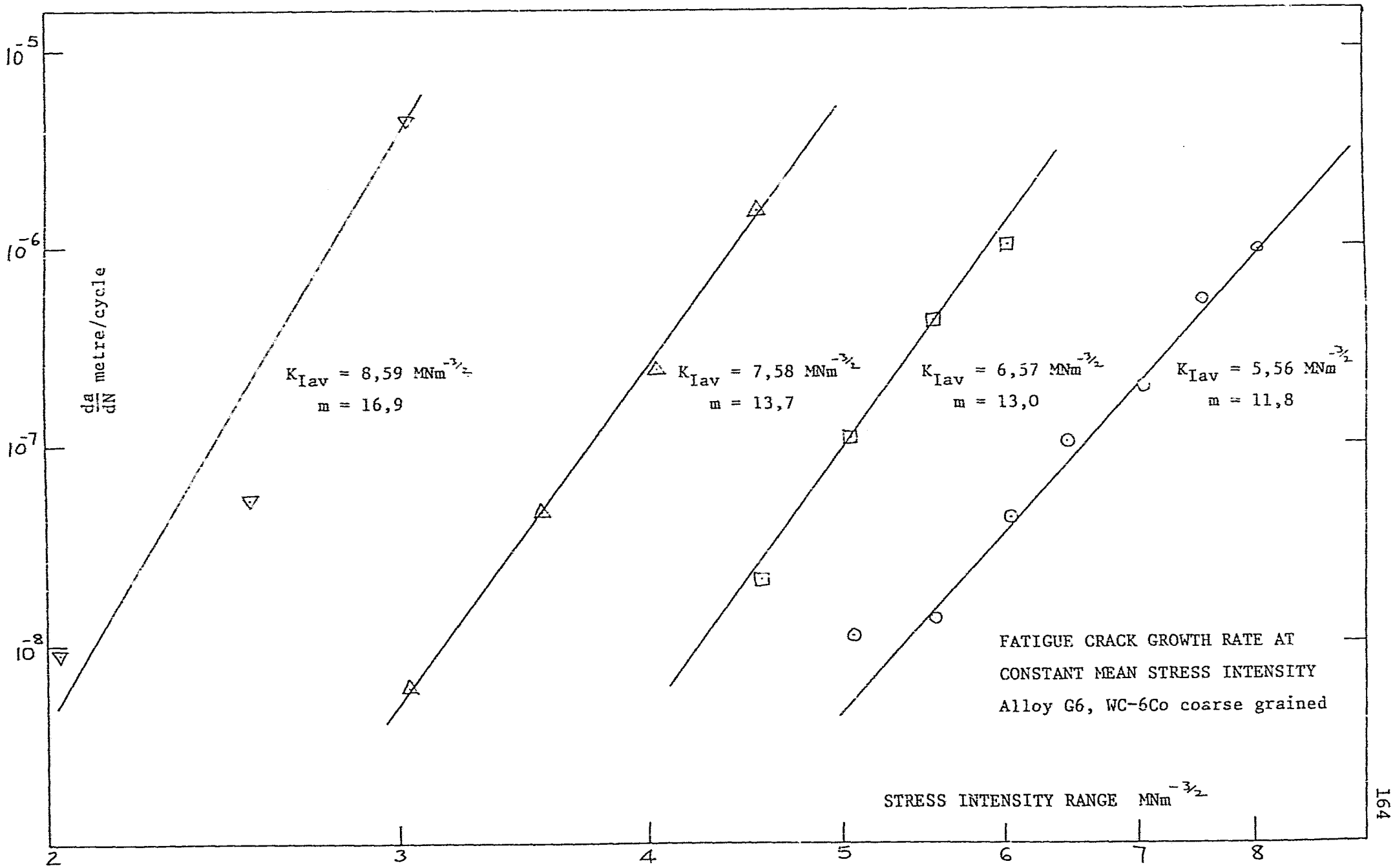
10^{-5}
10^{-6}
10^{-7}
10^{-8}
$\frac{da}{dN}$ metre/cycle
K_{Iav} = 8,59 $MNm^{-3/2}$
m = 16,9
K_{Iav} = 7,58 $MNm^{-3/2}$
m = 13,7
K_{Iav} = 6,57 $MNm^{-3/2}$
m = 13,0
K_{Iav} = 5,56 $MNm^{-3/2}$
m = 11,8
FATIGUE CRACK GROWTH RATE AT
CONSTANT MEAN STRESS INTENSITY
Alloy G6, WC-6Co coarse grained
STRESS INTENSITY RANGE $MNm^{-3/2}$
2
3
4
5
6
7
8

Figure 5.14

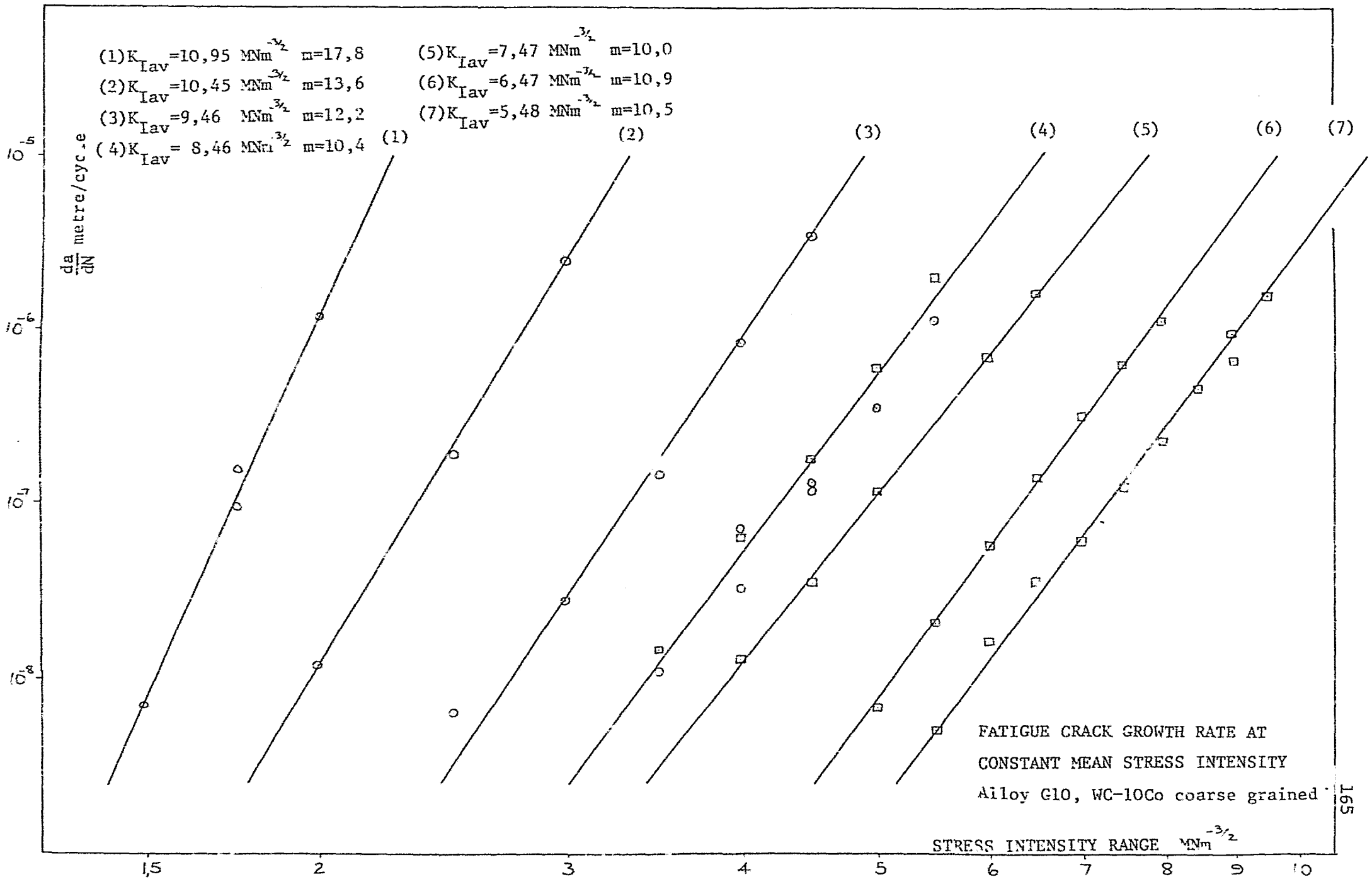
(1)K_Iav=10,95 MNm^-3/2 m=17,8
(2)K_Iav=10,45 MNm^-3/2 m=13,6
(3)K_Iav=9,46 MNm^-3/2 m=12,2
(4)K_Iav= 8,46 MNm^-3/2 m=10,4
(5)K_Iav=7,47 MNm^-3/2 m=10,0
(6)K_Iav=6,47 MNm^-3/2 m=10,9
(7)K_Iav=5,48 MNm^-3/2 m=10,5
da/dN metre/cycle
10^-5
10^-6
10^-7
10^-8
(1)
(2)
(3)
(4)
(5)
(6)
(7)
FATIGUE CRACK GROWTH RATE AT
CONSTANT MEAN STRESS INTENSITY
Alloy G10, WC-10Co coarse grained
STRESS INTENSITY RANGE MNm^-3/2
1,5
2
3
4
5
6
7
8
9
10

Figure 5.15

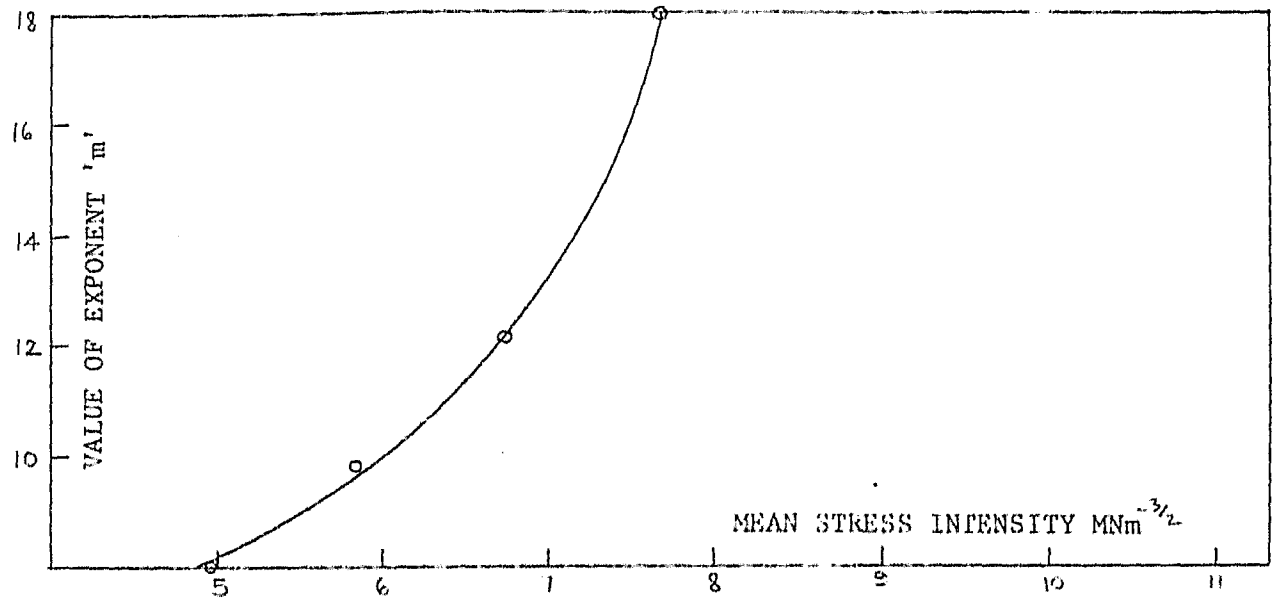

Figure 5.16 Alloy S10, WC-10Co fine grained

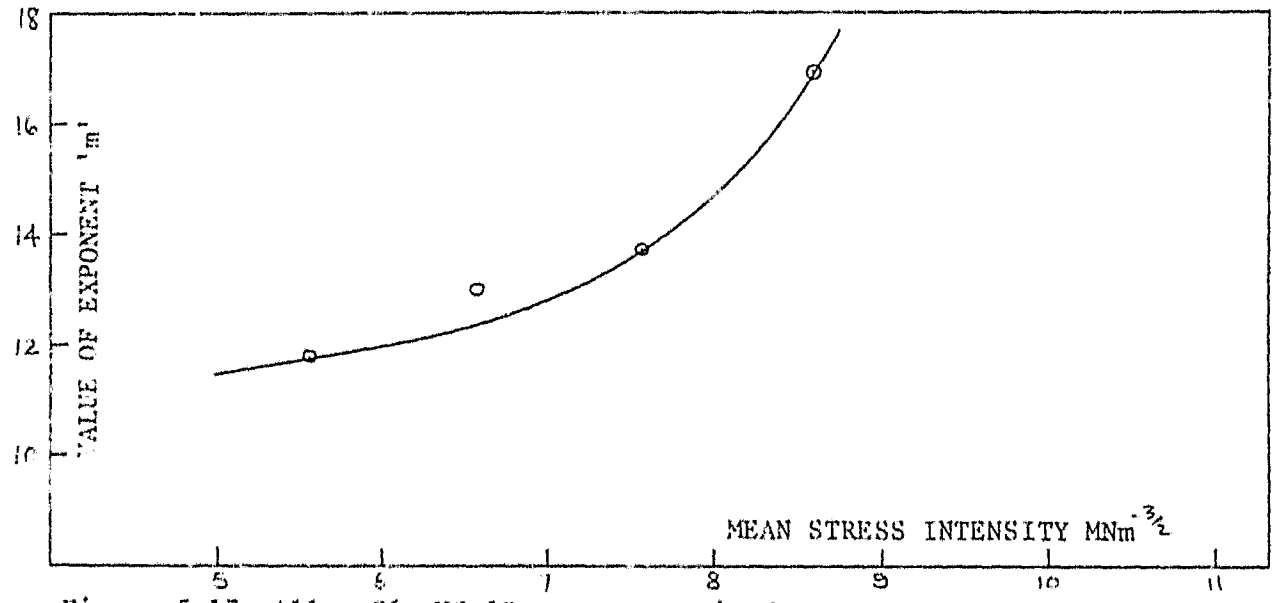

Figure 5.17 Alloy G6, WC-6Co coarse grained

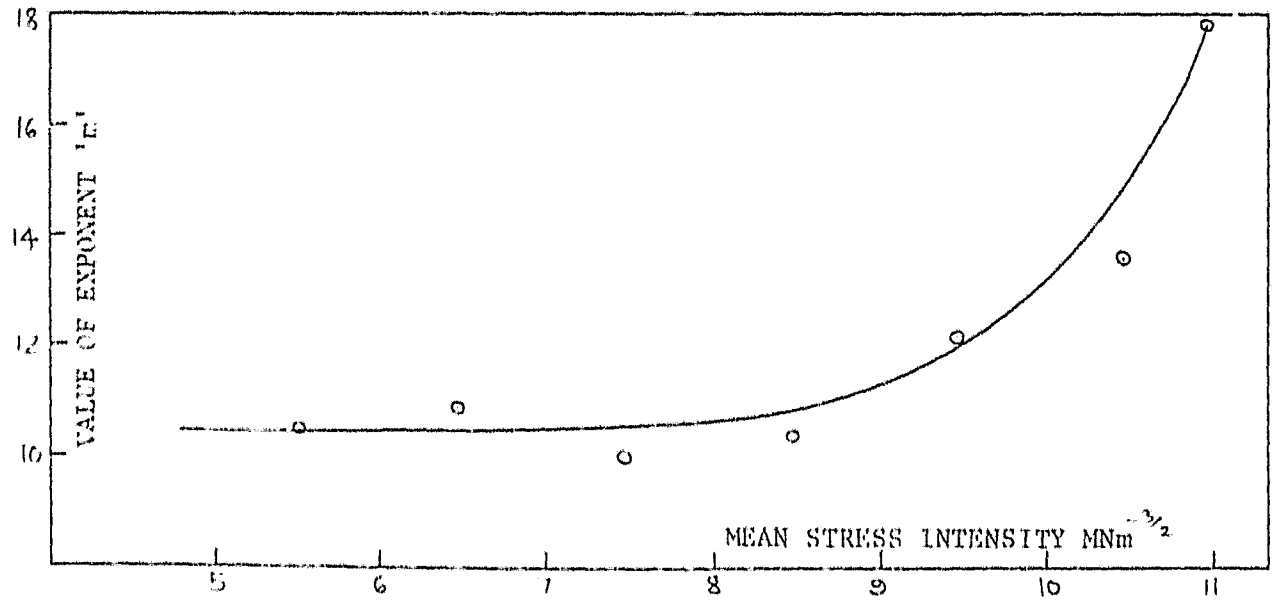

Figure 5.18 Alloy G10, WC-10Co coarse grained

GRAPHS SHOWING VARIATION IN THE VALUE OF THE EXPONENT 'm' AS THE MEAN STRESS INTENSITY INCREASES

5.2.3 Fatigue at Constant Stress Intensity Range

In order to determine the effect of mean stress intensity, independent of the stress intensity range, alloys S10 and G10 were tested at a constant stress intensity range, with the mean stress intensity increasing (Figure 5.19). The results show that provided K_{Imax} is below the static crack growth regime, the fatigue crack growth rate increases linearly (on a log-log plot) as K_{Iav} increases (Figures 5.20,5.21). This in itself shows that da/dN is not a simple function of ΔK_I but has a significant dependence on K_{Iav}.

The influence of K_{Iav} on crack growth rate in fact reflects the effect of the absolute values of K_{Imax} and K_{Imin} and is not in itself a controlling mechanistic parameter, (discussed in Chapter 6).

It would be quite feasible to plot graphs based only on K_{Imax} or K_{Imin}, but ΔK_I and K_{Iav} are the most convenient parameters for defining the cyclic loading.

As the peak stress intensity K_{Imax} reaches the static crack growth regime (Section 5.1.1, Figure 5.1) the rate of propagation increases dramatically, the gradients tending towards the very high values obtained for static growth. (Figures 5.22, 5.23).

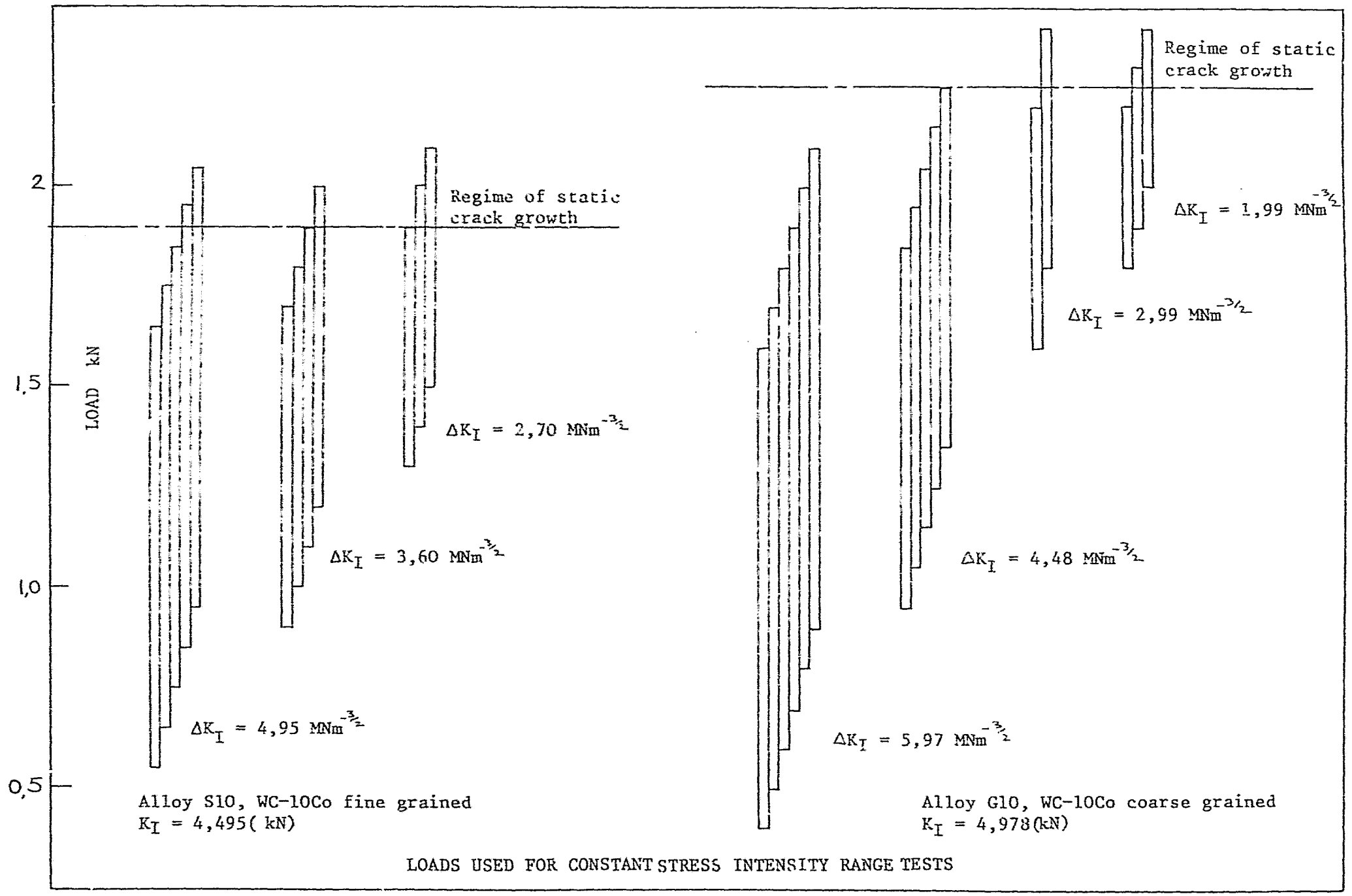
2
1.5
1,0
0,5
LOAD kN
Regime of static crack growth
ΔK_I = 2,70 MNm$^{-3/2}$
ΔK_I = 3,60 MNm$^{-3/2}$
ΔK_I = 4,95 MNm$^{-3/2}$
Alloy S10, WC-10Co fine grained
K_I = 4,495(kN)
Regime of static crack growth
ΔK_I = 1,99 MNm$^{-3/2}$
ΔK_I = 2,99 MNm$^{-3/2}$
ΔK_I = 4,48 MNm$^{-3/2}$
ΔK_I = 5,97 MNm$^{-3/2}$
Alloy G10, WC-10Co coarse grained
K_I = 4,978(kN)
LOADS USED FOR CONSTANT STRESS INTENSITY RANGE TESTS
168

Figure 5.19

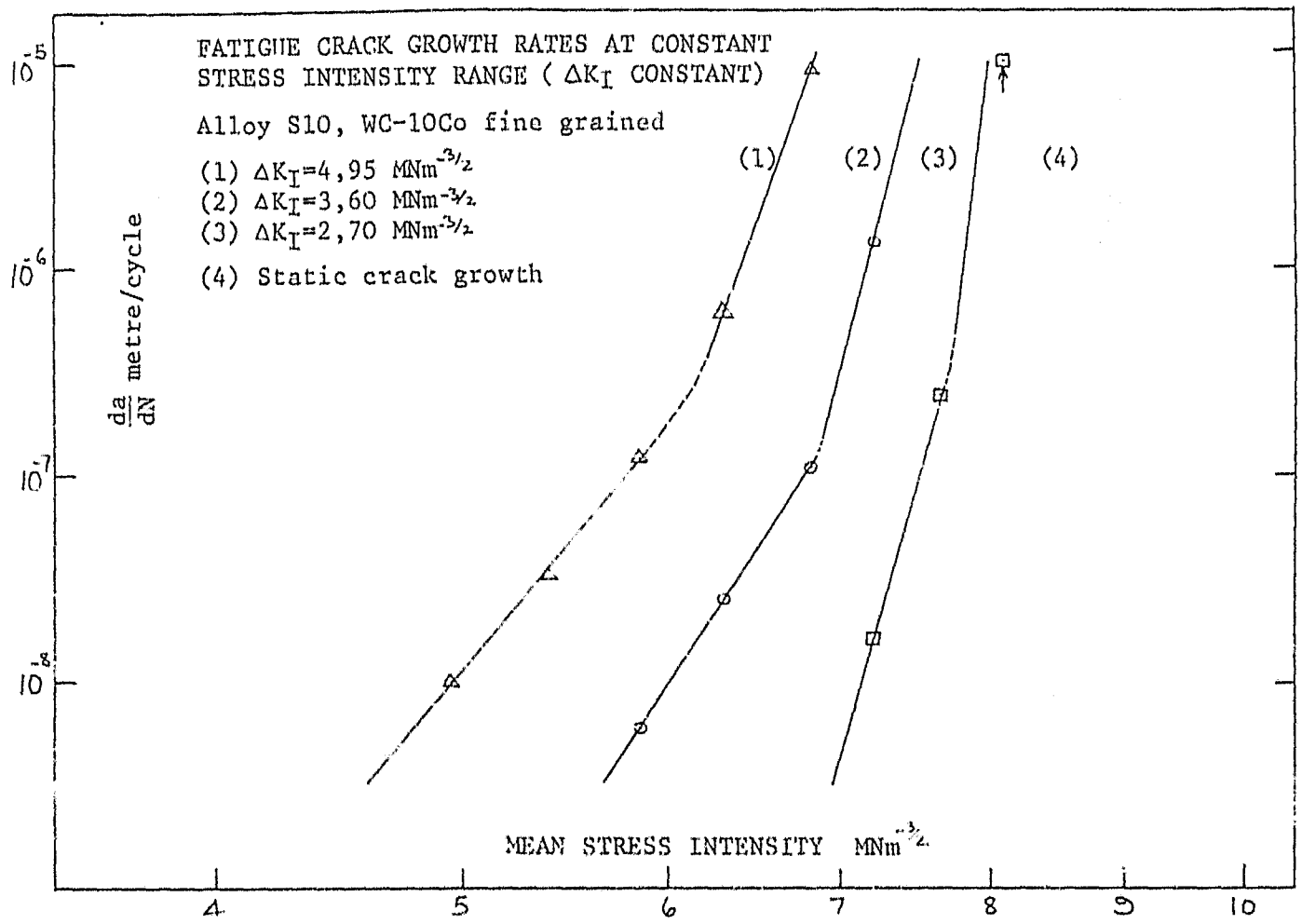

Figure 5.20

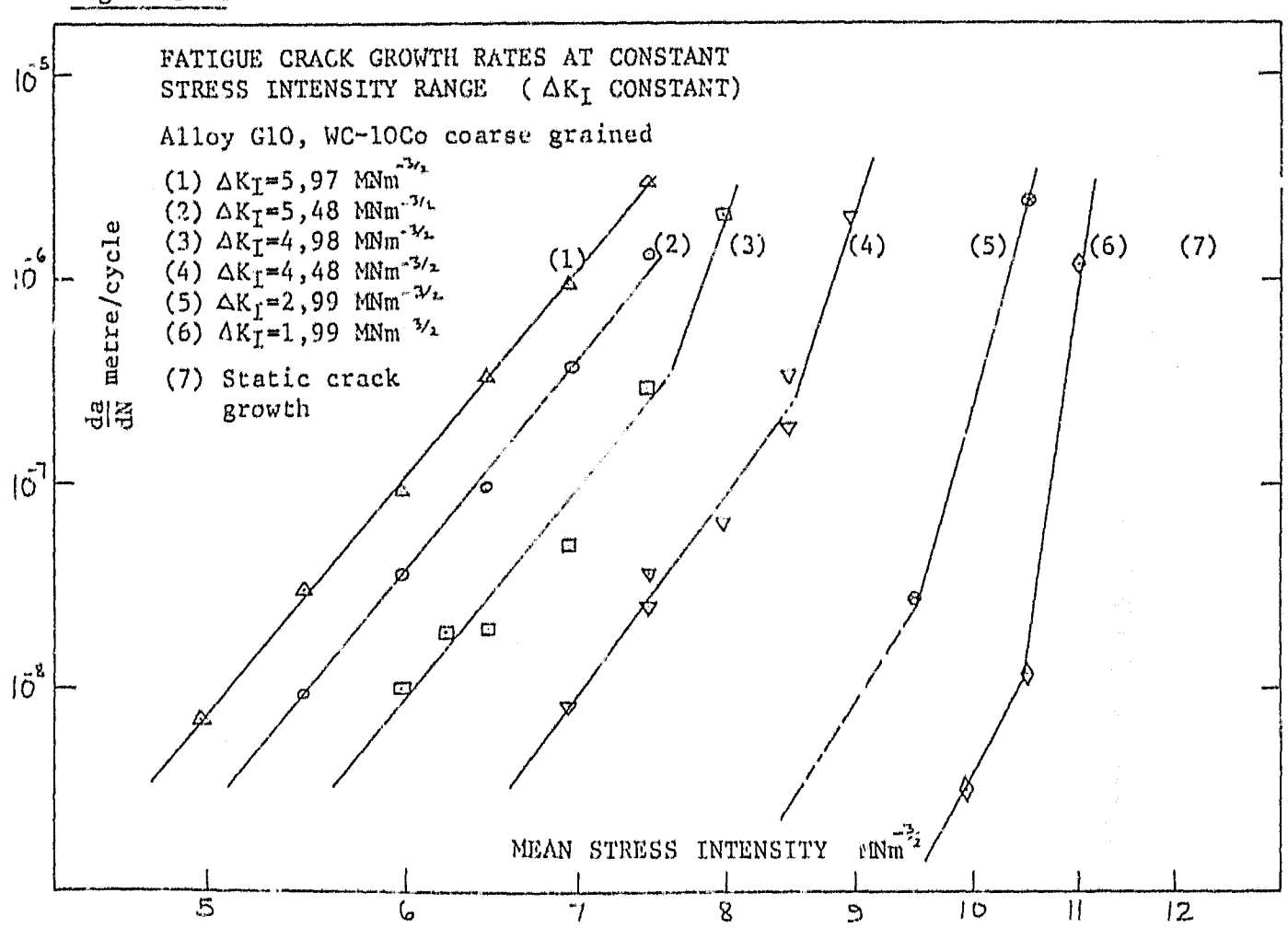

Figure 5.21

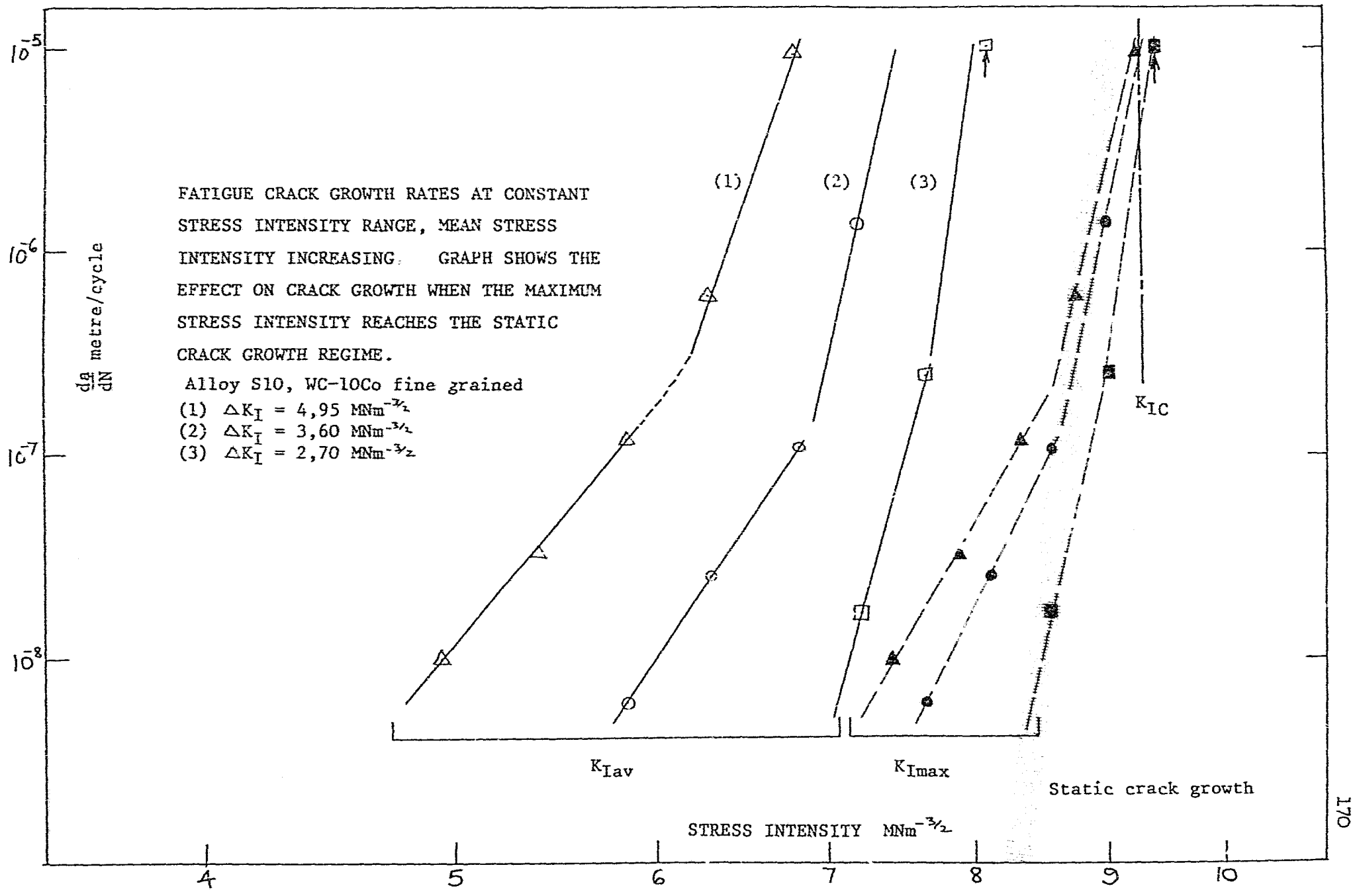
FATIGUE CRACK GROWTH RATES AT CONSTANT STRESS INTENSITY RANGE, MEAN STRESS INTENSITY INCREASING. GRAPH SHOWS THE EFFECT ON CRACK GROWTH WHEN THE MAXIMUM STRESS INTENSITY REACHES THE STATIC CRACK GROWTH REGIME.
Alloy S10, WC-10Co fine grained
(1) ΔK_I = 4,95 MNm^-3/2
(2) ΔK_I = 3,60 MNm^-3/2
(3) ΔK_I = 2,70 MNm^-3/2
da/dN metre/cycle
10^-5
10^-6
10^-7
10^-8
(1)
(2)
(3)
K_IC
K_Iav
K_Imax
Static crack growth
STRESS INTENSITY MNm^-3/2
4
5
6
7
8
9
10
170

Figure 5.22

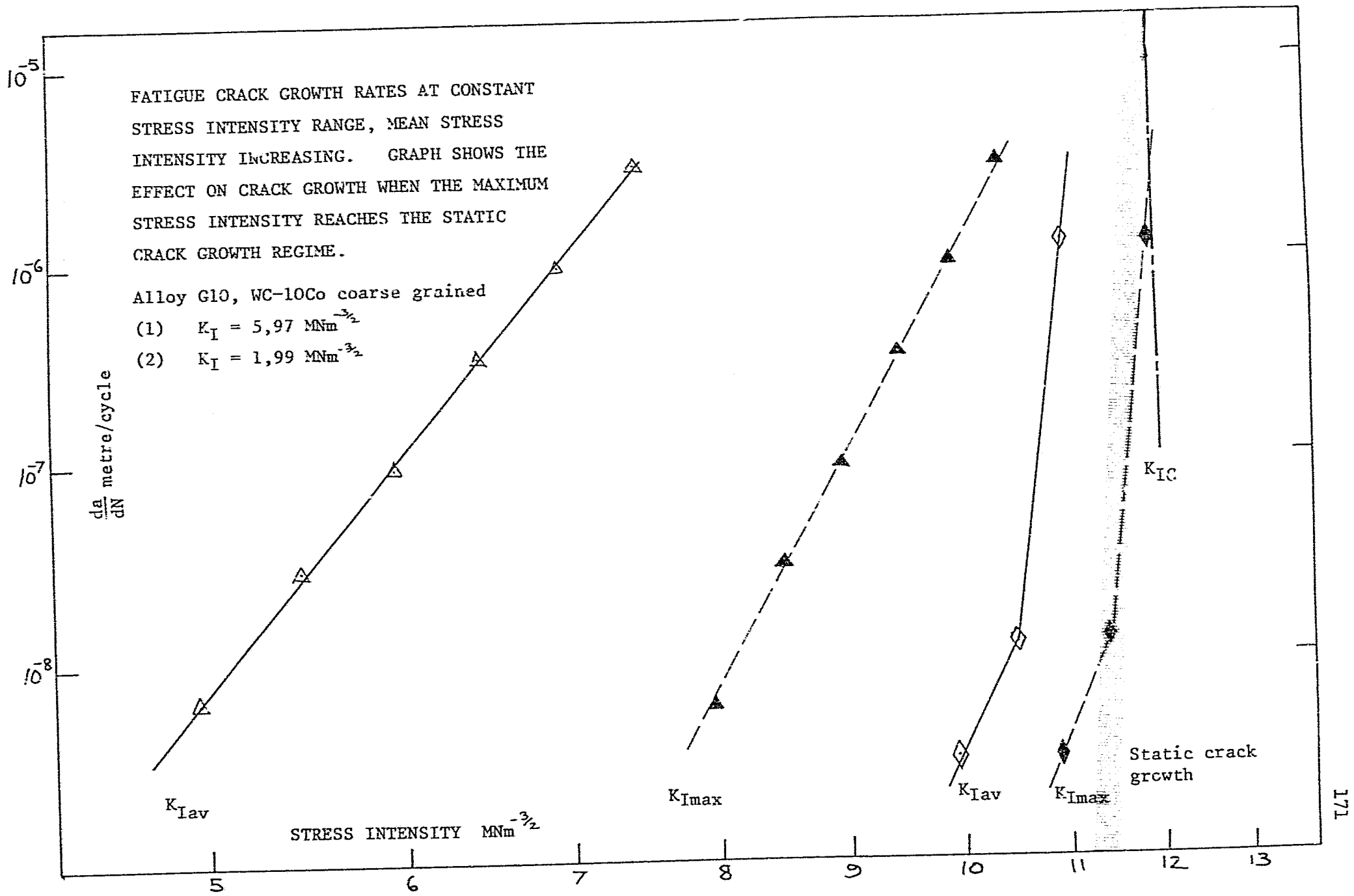
FATIGUE CRACK GROWTH RATES AT CONSTANT STRESS INTENSITY RANGE, MEAN STRESS INTENSITY INCREASING. GRAPH SHOWS THE EFFECT ON CRACK GROWTH WHEN THE MAXIMUM STRESS INTENSITY REACHES THE STATIC CRACK GROWTH REGIME.
Alloy G10, WC-10Co coarse grained
(1) K_I = 5,97 $MNm^{-3/2}$
(2) K_I = 1,99 $MNm^{-3/2}$
10^{-5}
10^{-6}
10^{-7}
10^{-8}
$\frac{da}{dN}$ metre/cycle
K_{Iav}
K_{Imax}
K_{Iav}
K_{Imax}
K_{IC}
Static crack growth
STRESS INTENSITY $MNm^{-3/2}$
5
6
7
8
9
10
11
12
13
171

Figure 5.23

5.2.4 Constant R Values

As previously mentioned in Section 5.2.2 the ratio of K_{Imin}/K_{Imax} is not very useful for interpreting mechanisms of crack growth because at a constant R value both ΔK_I and K_{Iav} increase. Engineering fatigue data is however still widely quoted in terms of the R ratio. The reason for this is that in a component containing a crack subjected to a mean load with a superimposed cyclic load both the mean and cyclic stress intensity range increase as the crack grows.

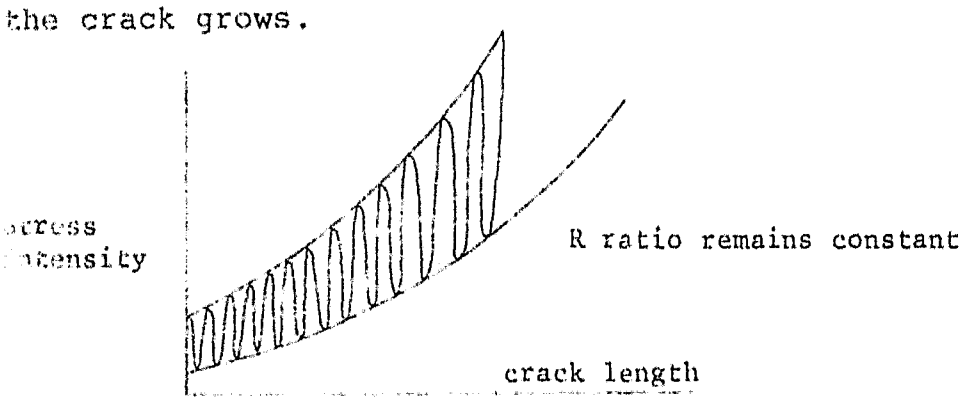

Graphs of constant R have been derived from the constant K_{Iav} results using the equation:

$$\Delta K_I = \frac{2(1 - R)}{(1 + R)} K_{Iav}$$

An R value is selected and using one of the K_{Iav} values plotted ΔK_I calculated. (Figures 5.24-5.26):

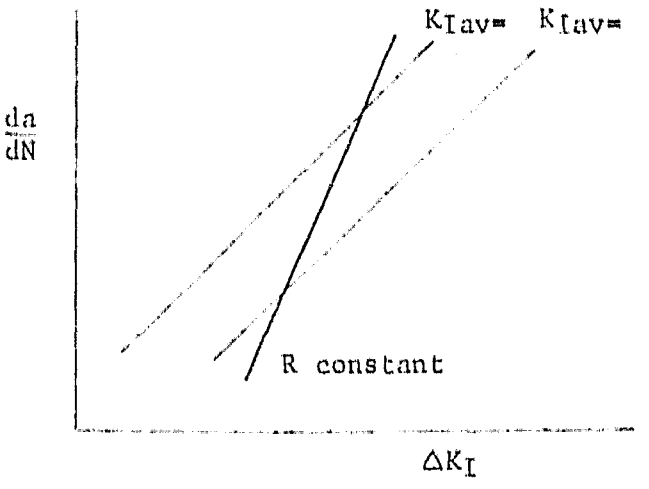

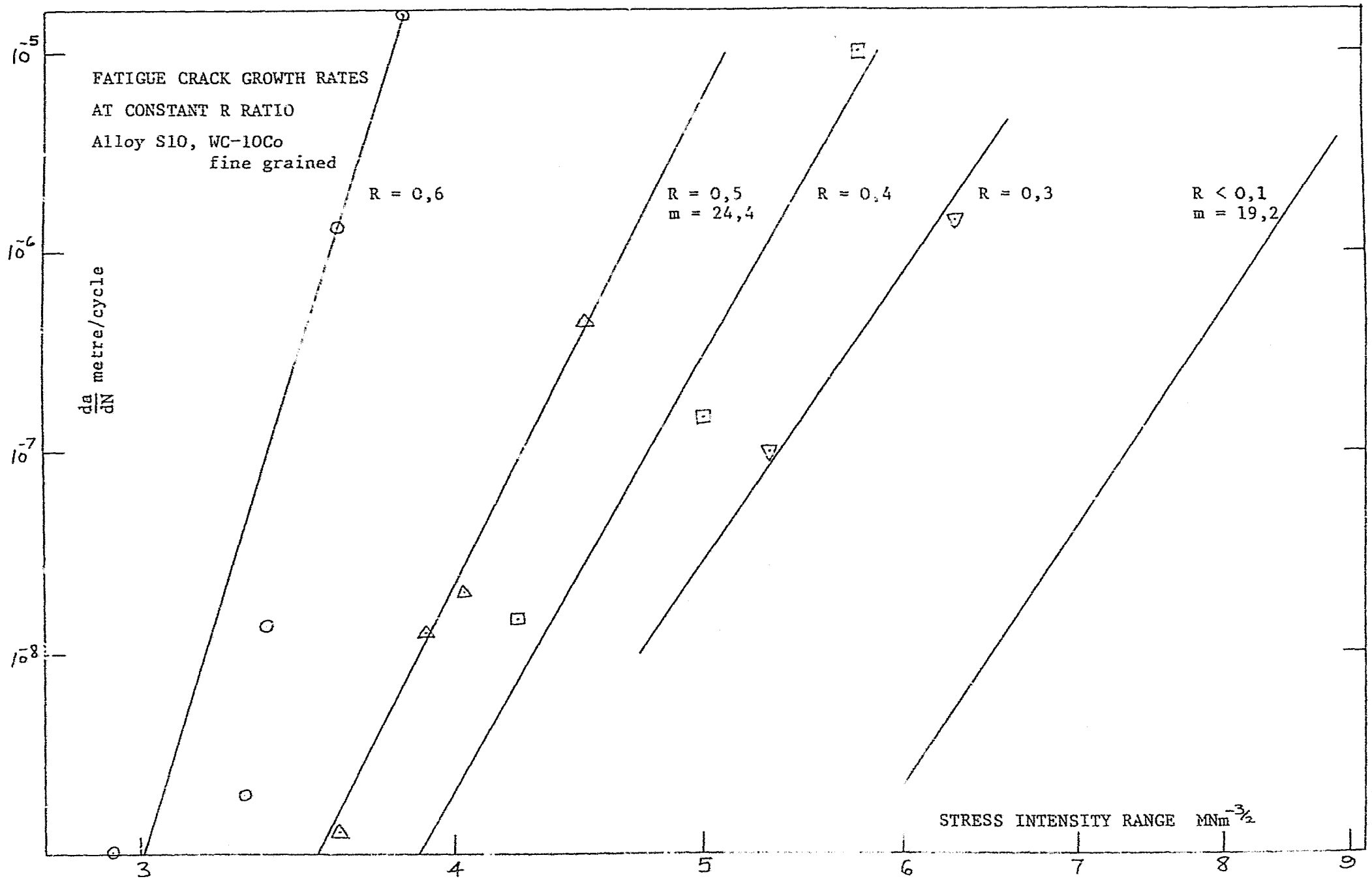
FATIGUE CRACK GROWTH RATES
AT CONSTANT R RATIO
Alloy S10, WC-10Co
fine grained
R = 0,6
R = 0,5
m = 24,4
R = 0,4
R = 0,3
R < 0,1
m = 19,2
10^{-5}
10^{-6}
10^{-7}
10^{-8}
$\frac{da}{dN}$ metre/cycle
3
4
5
6
7
8
9
STRESS INTENSITY RANGE MNm$^{-3/2}$

Figure 5.24

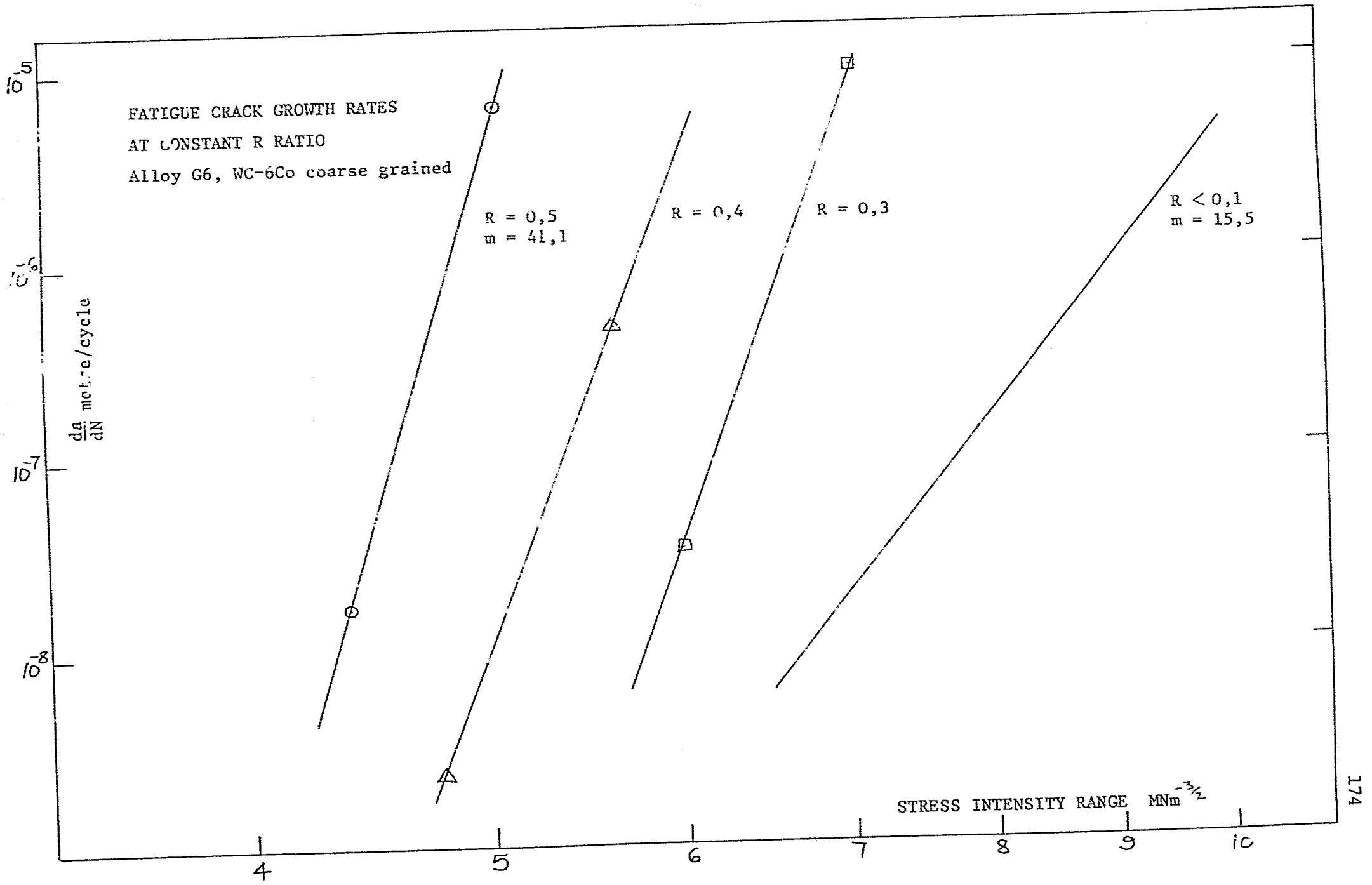
FATIGUE CRACK GROWTH RATES
AT CONSTANT R RATIO
Alloy G6, WC-6Co coarse grained
R = 0,5
m = 41,1
R = 0,4
R = 0,3
R < 0,1
m = 15,5
10^{-5}
10^{-6}
10^{-7}
10^{-8}
$\frac{da}{dN}$ metre/cycle
4
5
6
7
8
9
10
STRESS INTENSITY RANGE MNm$^{-3/2}$

Figure 5.25

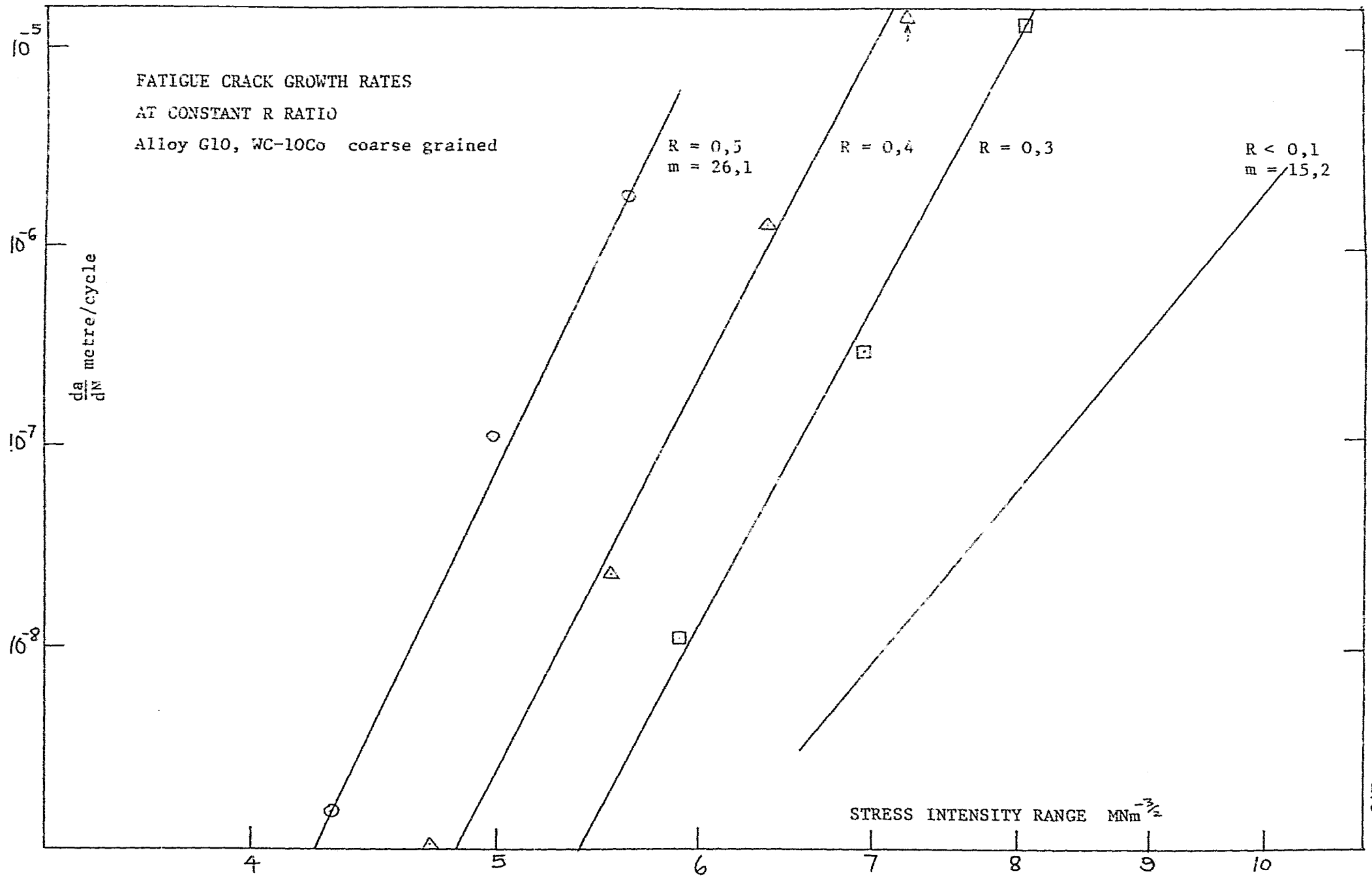
FATIGUE CRACK GROWTH RATES
AT CONSTANT R RATIO
Alloy G10, WC-10Co coarse grained
R = 0,5
m = 26,1
R = 0,4
R = 0,3
R < 0,1
m = 15,2
10^{-5}
10^{-6}
10^{-7}
10^{-8}
$\frac{da}{dN}$ metre/cycle
4
5
6
7
8
9
10
STRESS INTENSITY RANGE $MNm^{-3/2}$

Figure 5.26

5.2.5 Frequency Effects at R < 0,1

The effect of frequency on crack growth rate can be used to indicate whether time dependent static crack growth contributes to the fatigue propagation rate.

The technique employed to determine whether frequency has an effect was the 'change-over' test. Fatigue crack growth was monitored at a selected load range and frequency, and without changing any other conditions the frequency is increased or decreased by a factor of 10. Alloys S10, G10, G15 and 25E were tested at 50 Hz, 5 Hz and 0,5 Hz.

The results are somewhat confusing, since crack growth per cycle was observed both to increase and decrease as the frequency was reduced, (Figures 5.27 - 5.31). The changes in da/dN are however small, always less than 2x, which is well within the scatter expected from successive tests at the same frequency. (Figures 5.32,5.33).

In the load ranges tested there is no significant frequency effect on the crack growth rate (da/dN), (Figure 5.34). However, increasing the frequency from 5 to 50 Hz increases the crack growth rate w.r.t <u>time</u> da/dt, by a factor of 10. (Figure 5.35). This is strong evidence for a fatigue mechanism that is not time dependent.

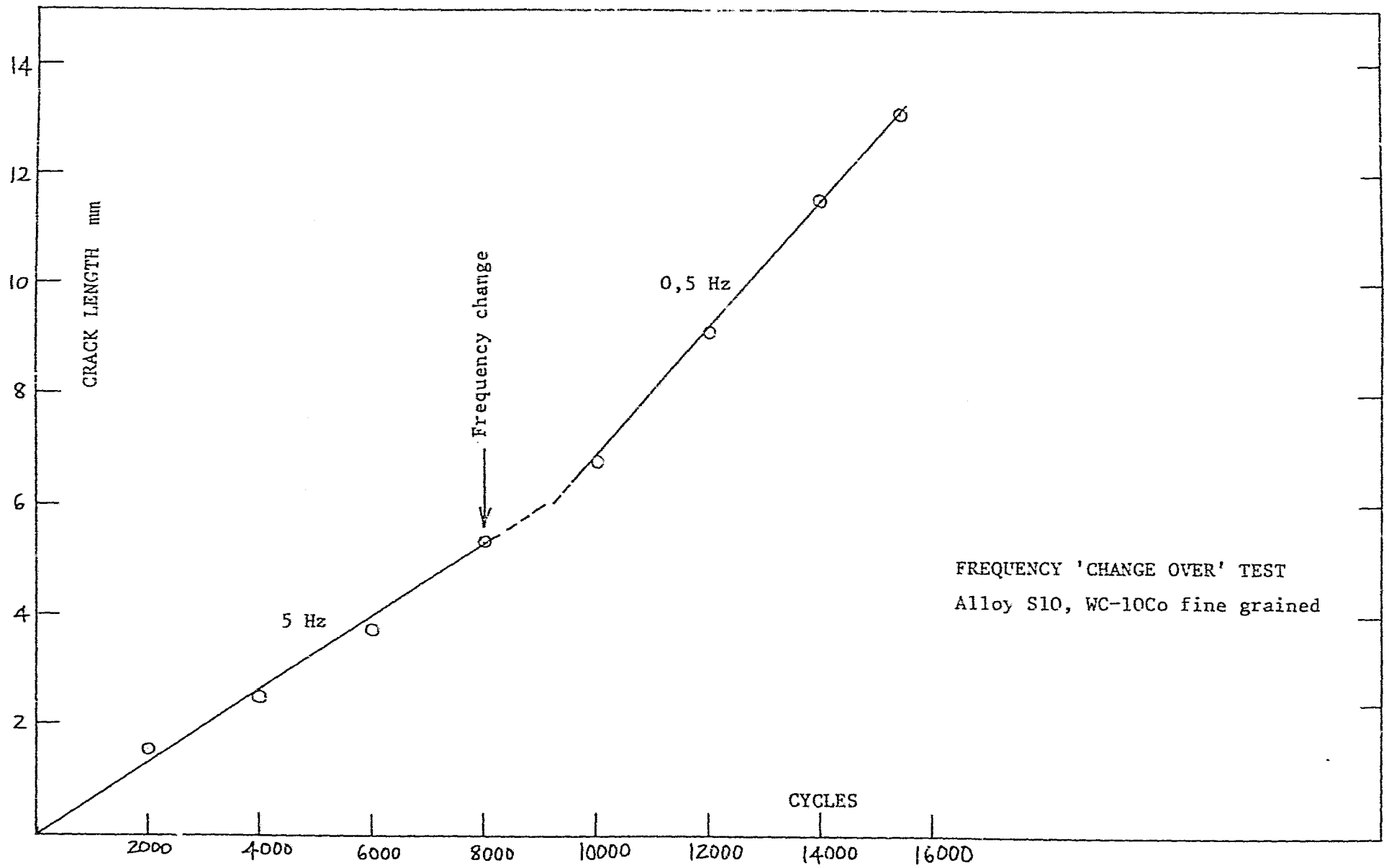
14
12
10
8
6
4
2
CRACK LENGTH mm
Frequency change
0,5 Hz
5 Hz
CYCLES
2000
4000
6000
8000
10000
12000
14000
16000
FREQUENCY 'CHANGE OVER' TEST
Alloy S10, WC-10Co fine grained

Figure 5.27

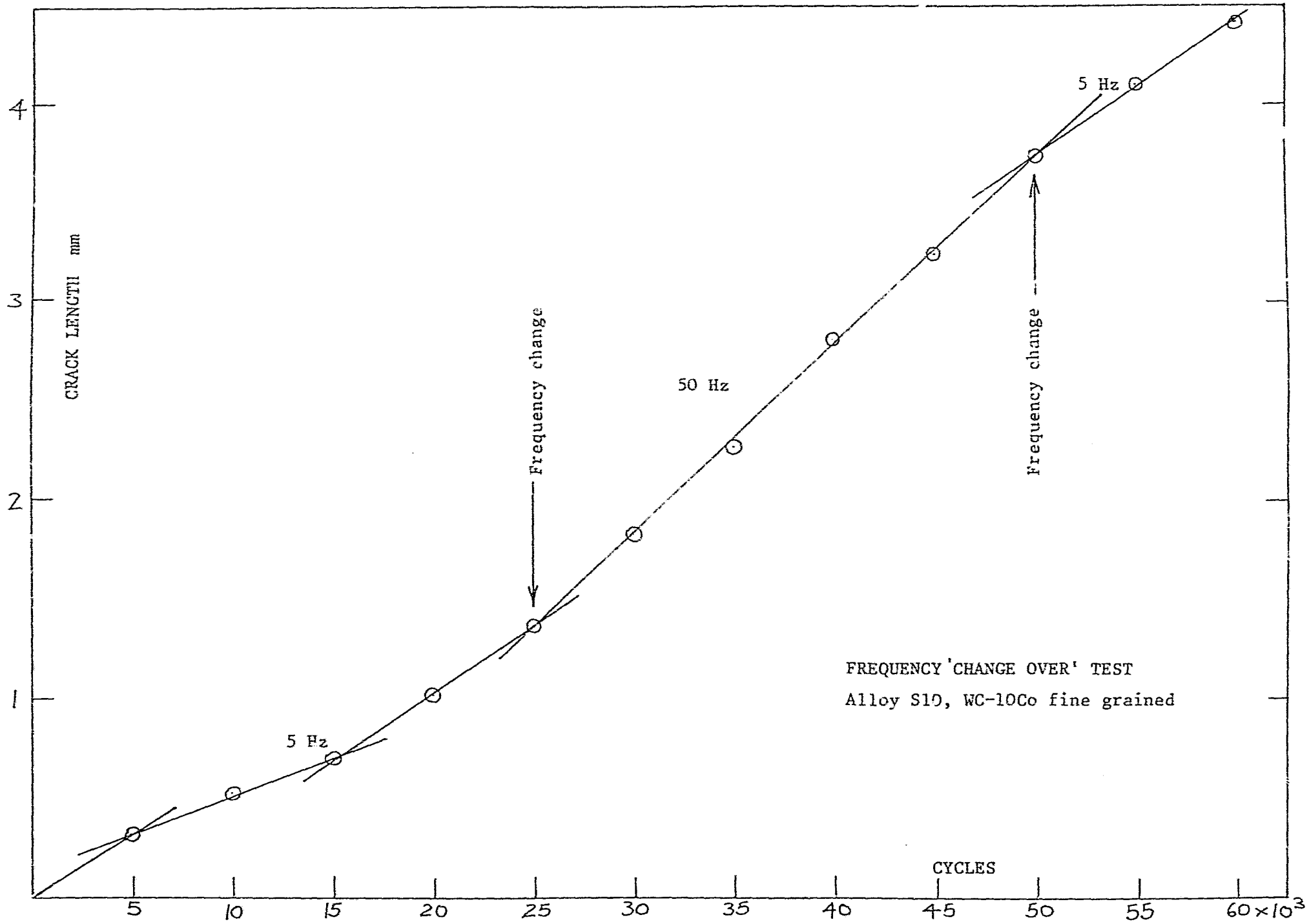
CRACK LENGTH mm
4
3
2
1
5 Hz
50 Hz
Frequency change
Frequency change
5 Hz
FREQUENCY 'CHANGE OVER' TEST
Alloy S10, WC-10Co fine grained
CYCLES
5
10
15
20
25
30
35
40
45
50
55
60×10³

Figure 5.28

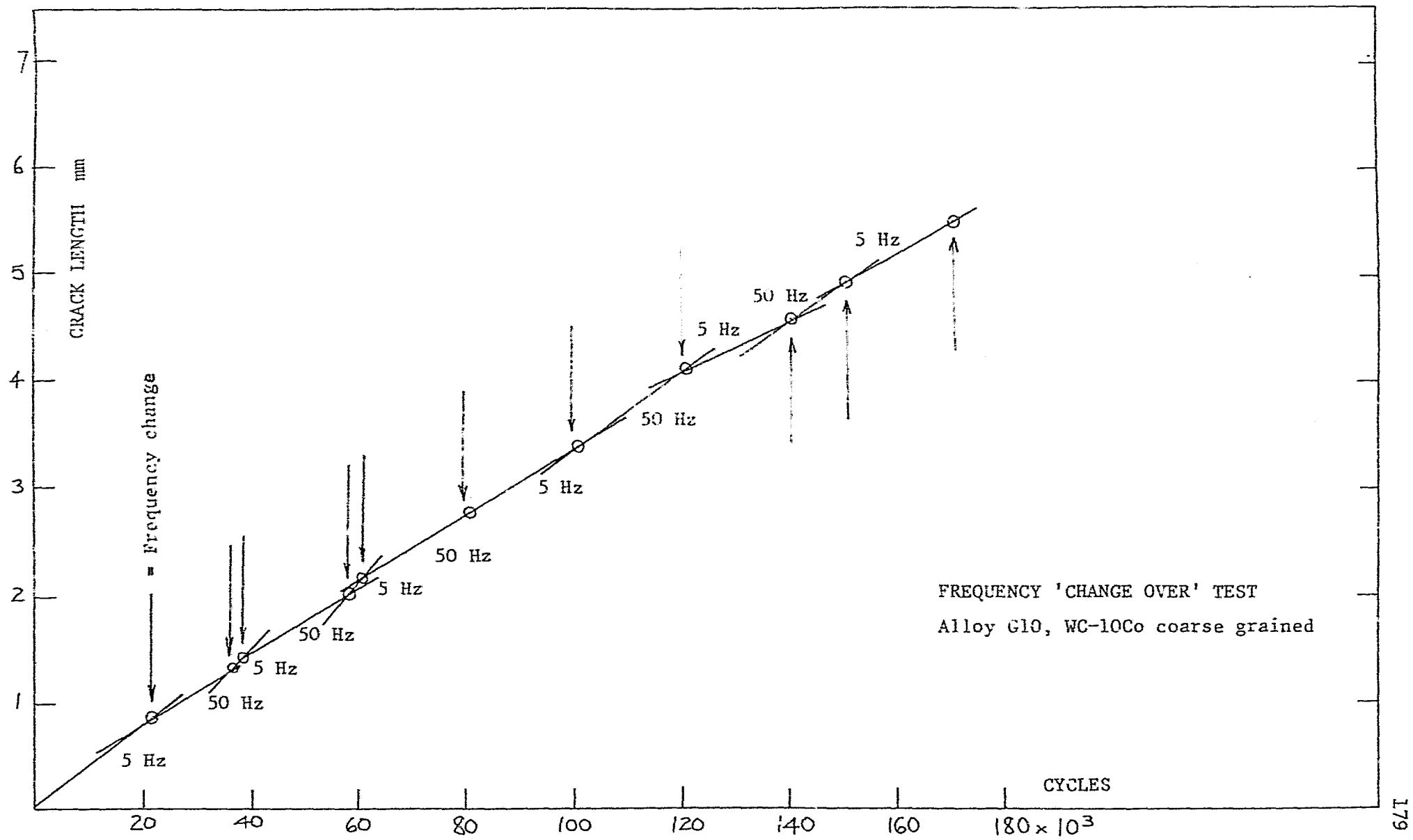
CRACK LENGTH mm
= Frequency change
5 Hz
50 Hz
CYCLES
20
40
60
80
100
120
140
160
180 x 10³
1
2
3
4
5
6
7
FREQUENCY 'CHANGE OVER' TEST
Alloy G10, WC-10Co coarse grained
179

Figure 5.29

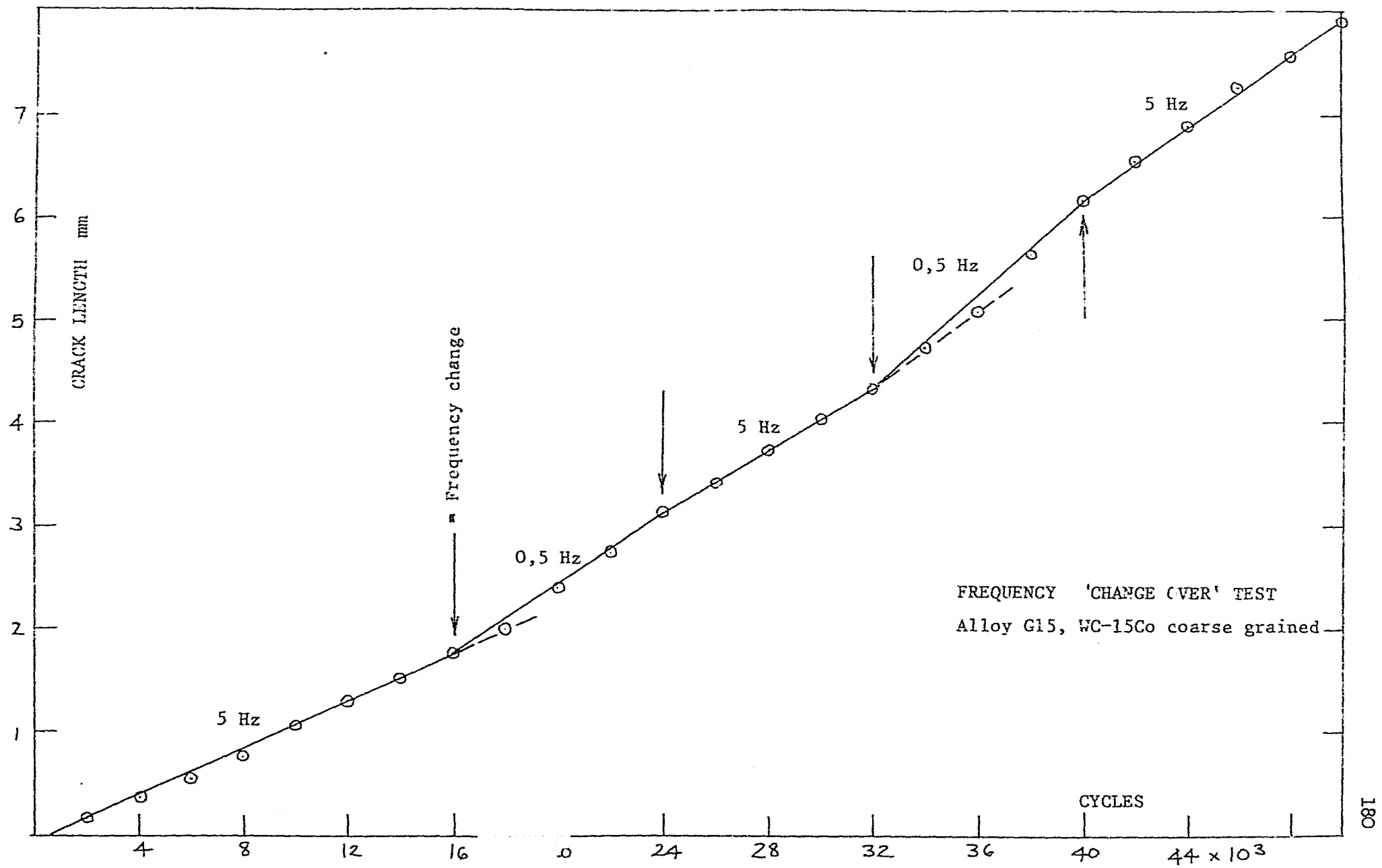
CRACK LENGTH mm
7
6
5
4
3
2
1
Frequency change
5 Hz
0,5 Hz
5 Hz
0,5 Hz
5 Hz
FREQUENCY 'CHANGE OVER' TEST
Alloy G15, WC-15Co coarse grained
CYCLES
4
8
12
16
20
24
28
32
36
40
44 x 10³

Figure 5.30

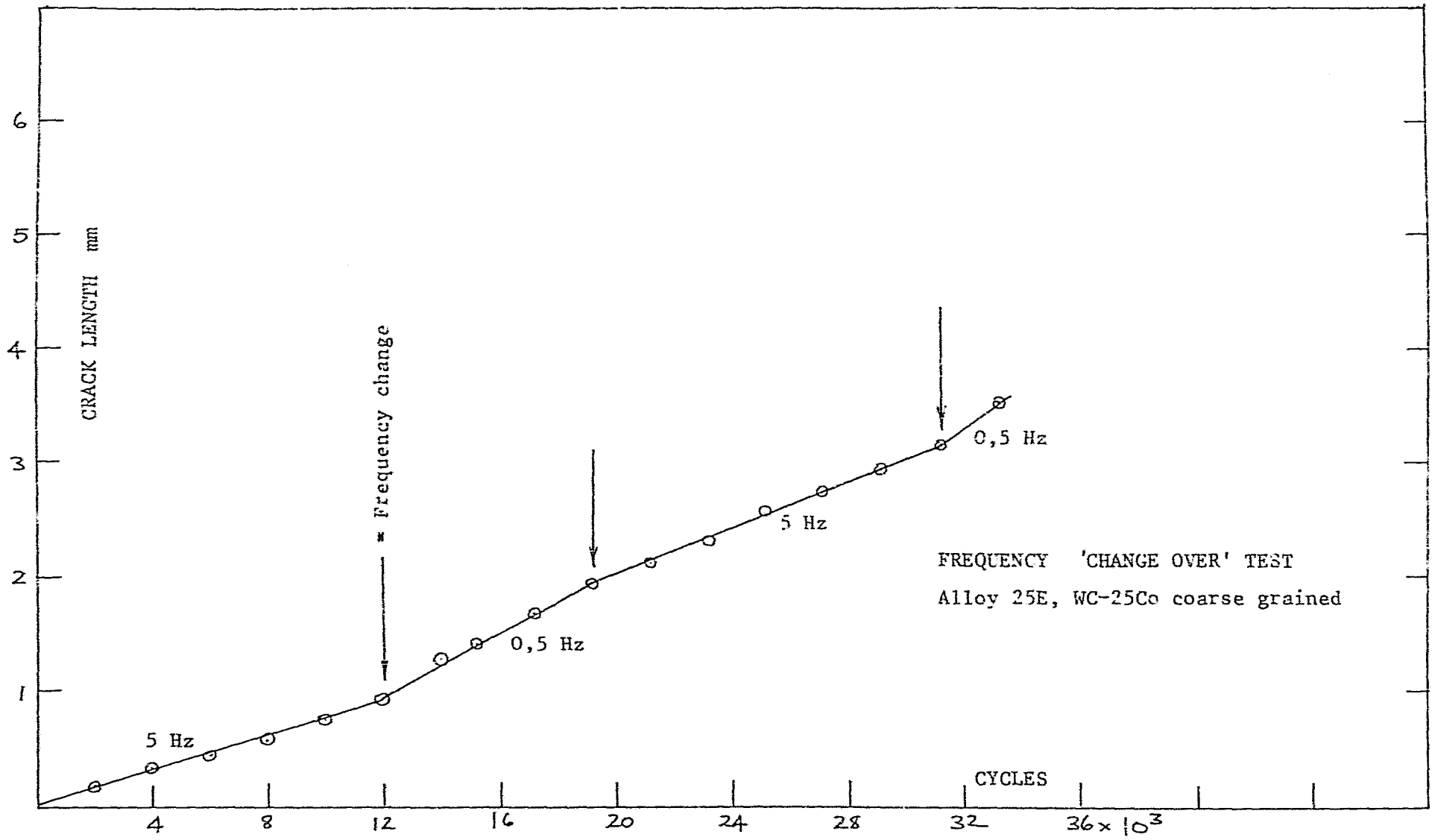
CRACK LENGTH mm
1
2
3
4
5
6
* Frequency change
5 Hz
0,5 Hz
5 Hz
0,5 Hz
FREQUENCY 'CHANGE OVER' TEST
Alloy 25E, WC-25Co coarse grained
CYCLES
4
8
12
16
20
24
28
32
36 x 10³

Figure 5.31

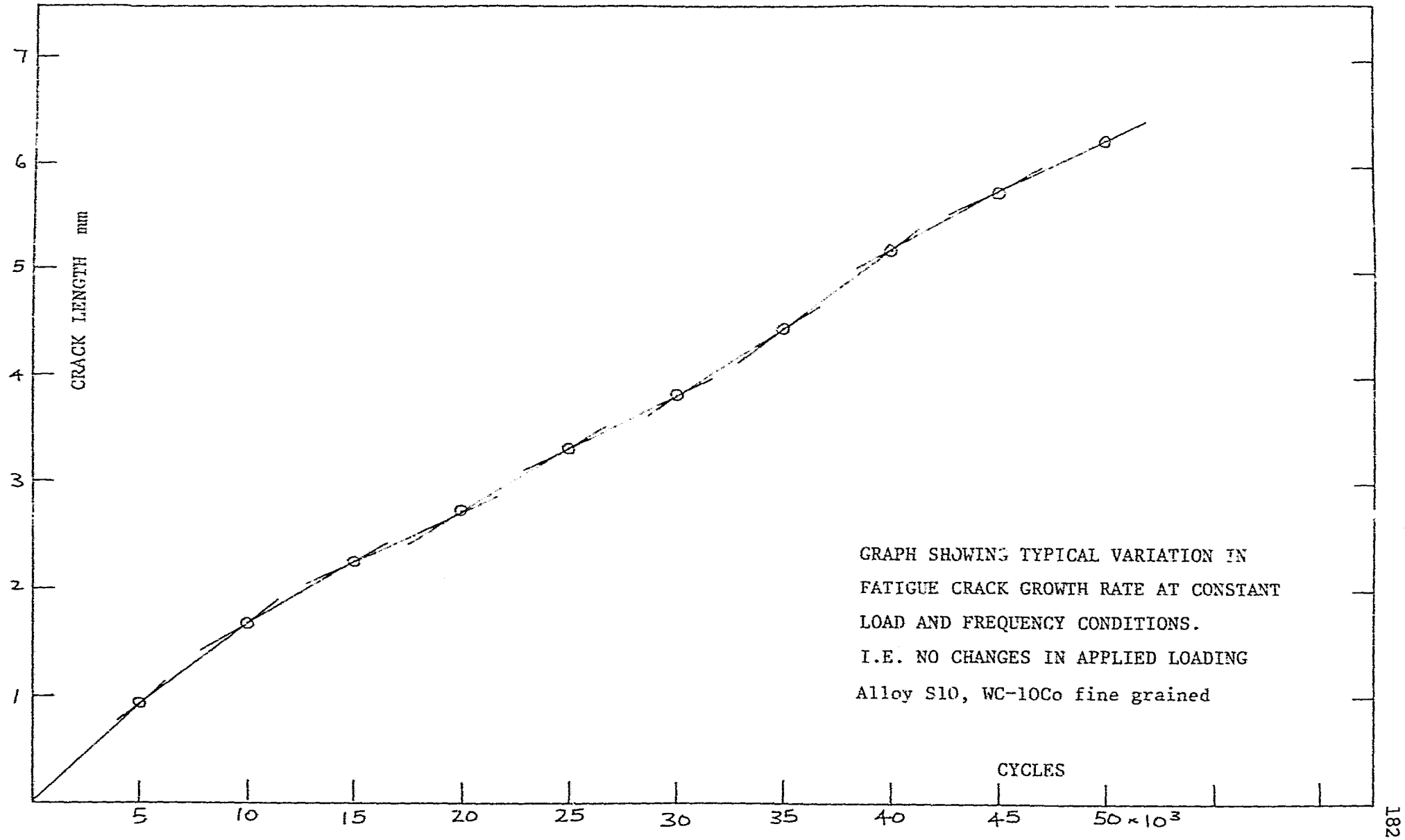
CRACK LENGTH mm
1
2
3
4
5
6
7
5
10
15
20
25
30
35
40
45
50 × 10³
CYCLES
GRAPH SHOWING TYPICAL VARIATION IN
FATIGUE CRACK GROWTH RATE AT CONSTANT
LOAD AND FREQUENCY CONDITIONS.
I.E. NO CHANGES IN APPLIED LOADING
Alloy S10, WC-10Co fine grained

Figure 5.32

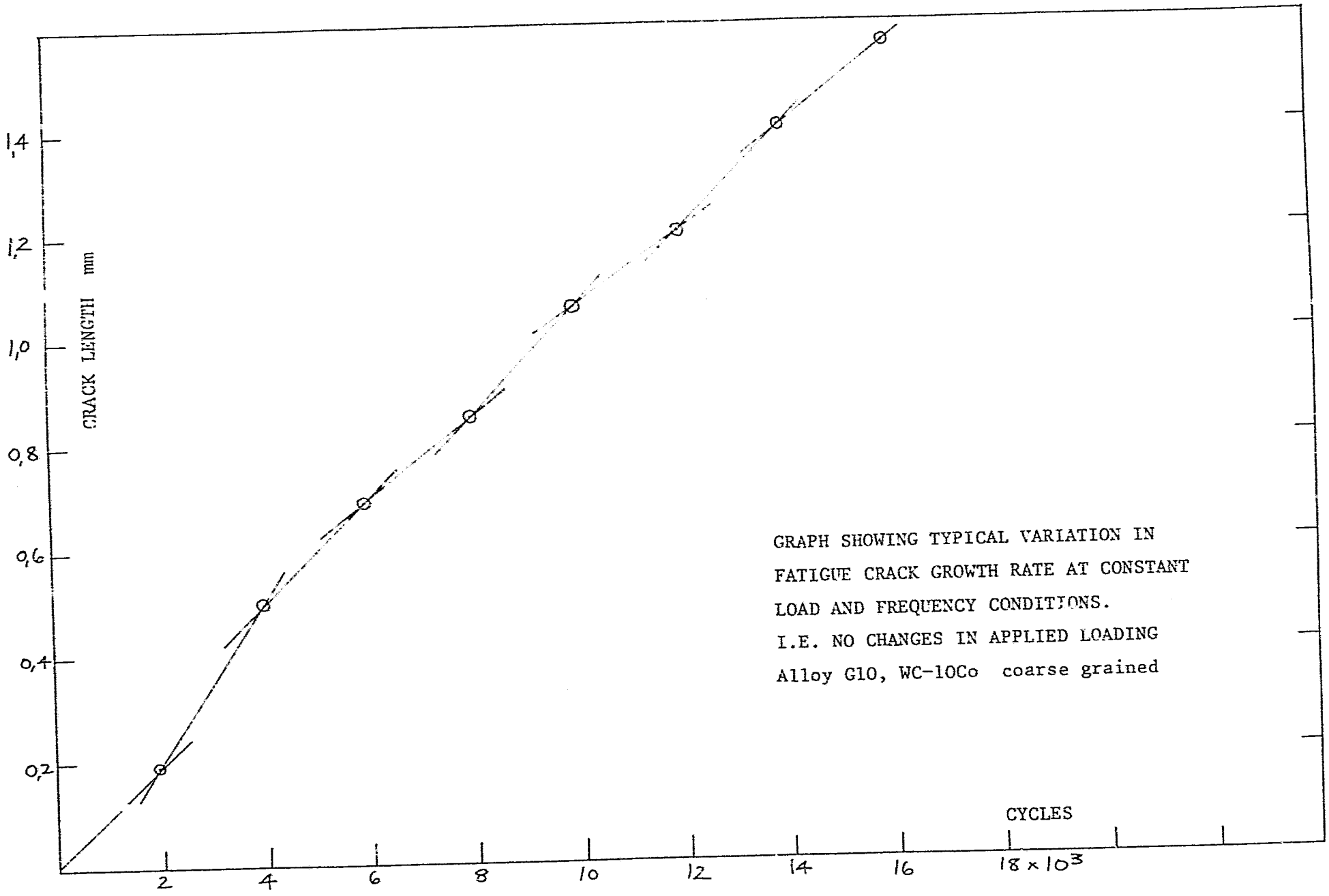
CRACK LENGTH mm
1,4
1,2
1,0
0,8
0,6
0,4
0,2
2
4
6
8
10
12
14
16
18 x 10³
CYCLES
GRAPH SHOWING TYPICAL VARIATION IN
FATIGUE CRACK GROWTH RATE AT CONSTANT
LOAD AND FREQUENCY CONDITIONS.
I.E. NO CHANGES IN APPLIED LOADING
Alloy G10, WC-10Co coarse grained

Figure 5.33

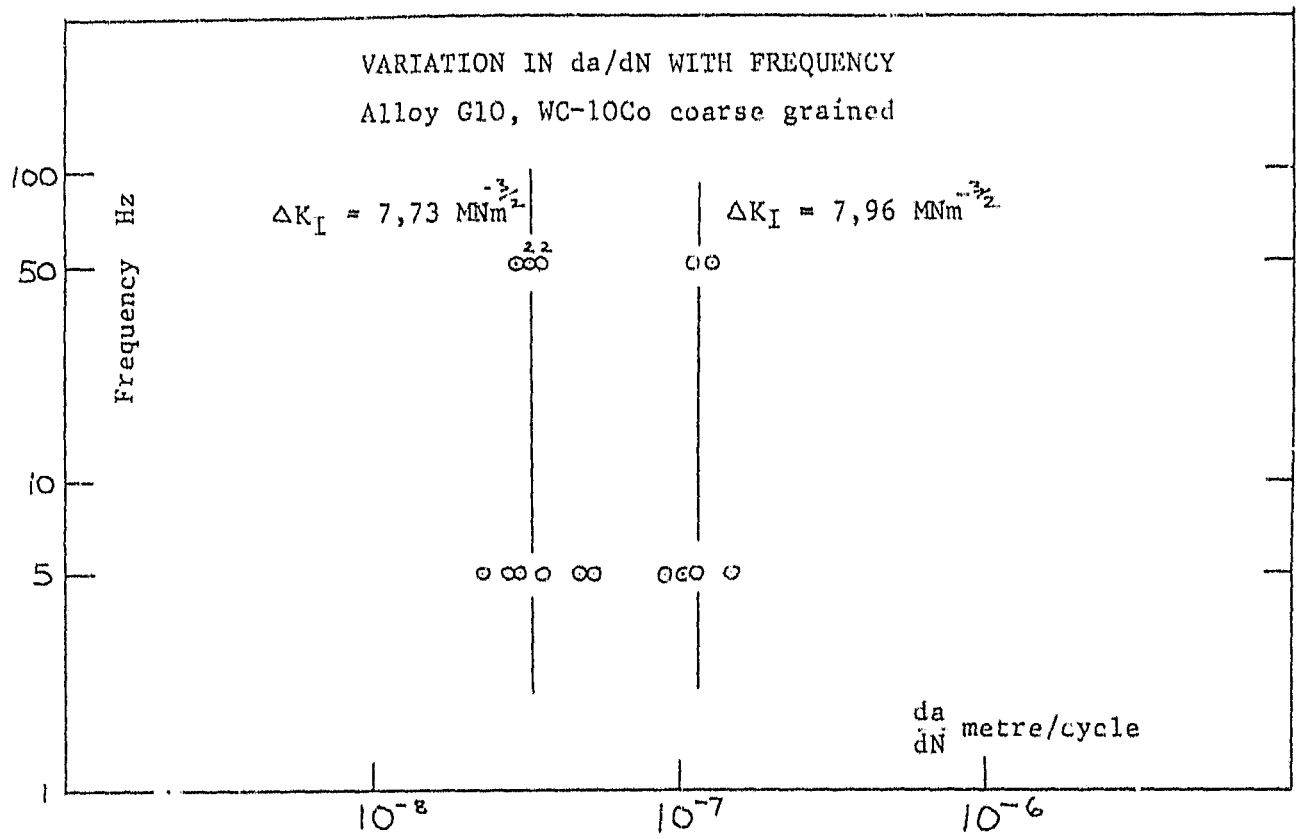

Figure 5.34 Graph shows no significant change in crack growth rate per cycle as frequency increases.

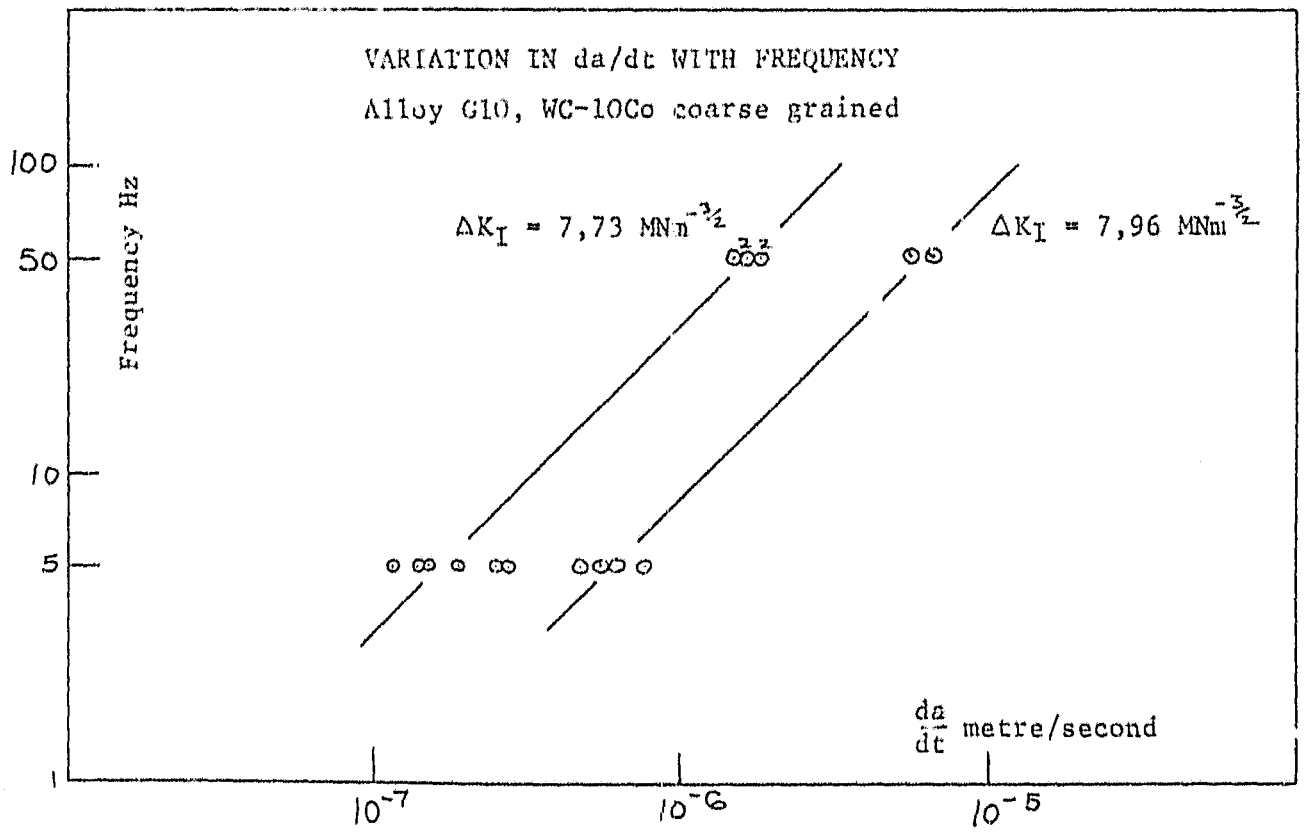

Figure 5.35 Graph shows significant influence of frequency on crack growth rate with respect to time.

5.2.6. Fatigue Fracture Path

It is extremely difficult to determine from fracture surface studies whether the fracture is predominantly intergranular or transgranular. The method of matching surfaces developed by Luyckx[116] is extremely tedious and has not been used in this study, although it could well be considered advantageous in any future work.

An alternative technique was used to study the path of the fatigue fracture. The region of the crack tip is first cut from the double torsion specimen. Approximately 0,5 mm is then ground off the surface which is then polished and etched for optical and scanning electron microscopy.

The micrographs (Figures 5.36 - 5.38) show that the crack is primarily intergranular, propagating either through the cobalt binder or at the WC-Co and WC-WC boundaries. Transgranular fracture of the carbide grains is however not uncommon. If there is free carbon present close to the line of propagation the crack deviates through it, selecting the line of least resistance. (Figure 5.36).

There is evidence to suggest that the binder spans the crack behind the tip, but these apparent ligaments (as arrowed in Figure 5.39) may only be asperities that have bridged the crack surfaces when the displacement has decreased due to load removal. (It should also be remembered that debris and damage may be introduced to the crack during grinding and polishing.)

The extremely tortuous nature of the crack shows that local fracture comprises a combination of mode I and mode II opening.

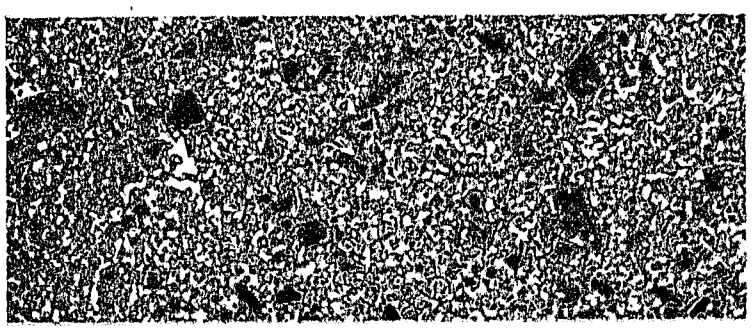

Figure 5.36 Alloy S 10 Optical 1000 X

$da/dN = 5,0 \times 10^{-7}$ m/cycle

$\Delta K_I = 7,64$ $MNm^{3/2}$

$K_{Iav} = 8,54$ $MNm^{-3/2}$

$R = 0,056$

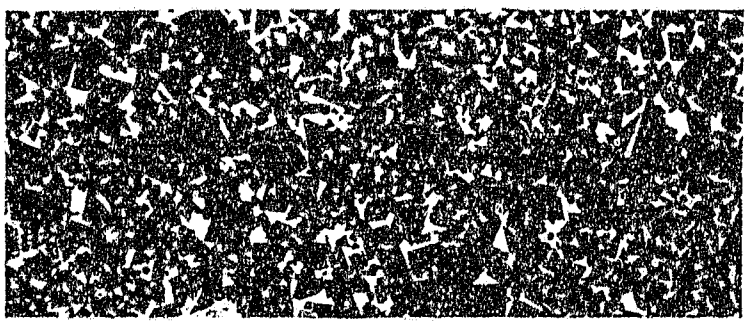

Figure 5.37 Alloy G 10 Optical 1000 X

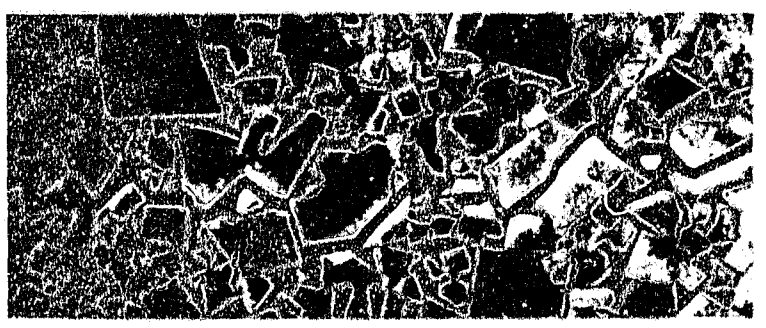

Figure 5.38 Alloy G 10 SEM 2200 X

$da/dN = 3,67 \times 10^{-6}$ m/cycle

$\Delta K_I = 4,49$ $MNm^{3/2}$

$K_{Iav} = 8,22$ $MNm^{-3/2}$

$R = 0,57$

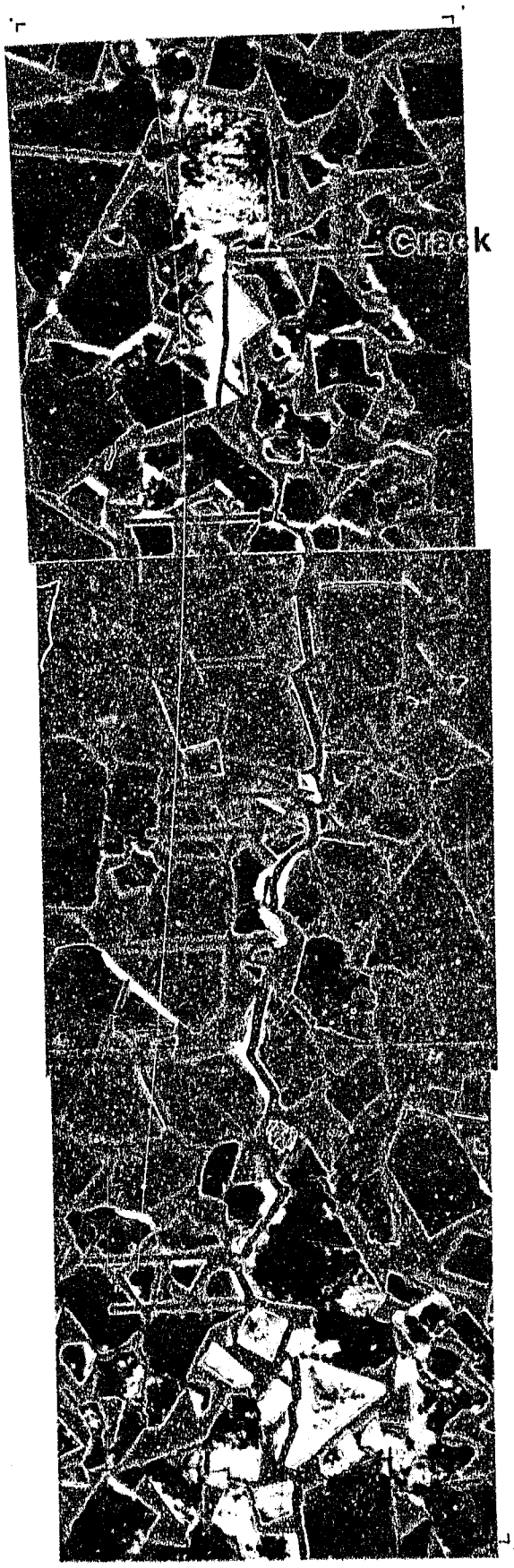

Figure 5.39 Fatigue fracture path at crack tip, alloy G10, WC-10Co coarse grained, loading details as for Figure 5.38. Arrows indicate sites where ligaments seem to span the crack.

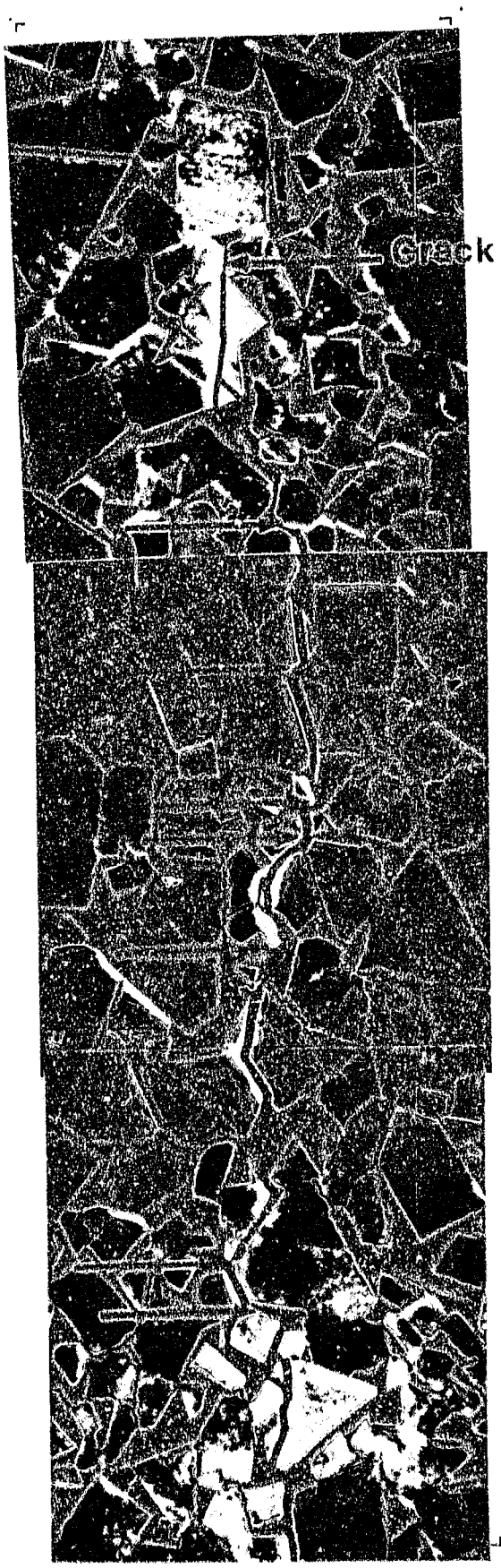

Figure 5.39 Fatigue fracture path at crack tip, alloy G10, WC-10Co coarse grained, loading details as for Figure 5.38. Arrows indicate sites where ligaments seem to span the crack.

5.2.7 Fatigue at Elevated Temperature

Many cemented carbide components are subjected either to fatigue loading at elevated temperatures or thermal cycling, or indeed a combination of both. It is therefore desirable to determine the effect of temperature on the rate of crack propagation. Some preliminary results have therefore been obtained for alloys S10 and G10 which have been tested using the procedure detailed in Section 4.7, at an R ratio < 0,1.

5.2.7.1 Effect of Thermal Cycling

Before carrying out elevated temperature fatigue loading the effect of thermal cycling was checked. This was particularly necessary because the method of monitoring high temperature fatigue crack growth involved periodic thermal cycling. Crack growth was monitored in two S10 alloy specimens at room temperature using a ΔK_I of 7,18 $MNm^{-3/2}$ and K_{Iav} of 4,04 $MNm^{-3/2}$. Once the rate had stabilised the cyclic load was switched off and while the mean stress intensity of 4,04 $MNm^{-3/2}$ was maintained (in load control) the specimen heated to 500°C for half an hour. After cooling, the heating element was moved and the position of the crack tip carefully located using the microscope cross hairs.

In 10 tests carried out on two different specimens no change in crack length due to heating and cooling only could be detected.

In addition the crack growth rate before and after a heating cycle was essentially identical, (Figure 5.40). This result confirms that no crack advance occurs during the thermal cycling; if it did, there would an apparent increase in the growth rate in the subsequent measurement. It also shows that the combined effects of static load ($K_{Istatic}$ = 4,04 $MNm^{-3/2}$ during heating) and temperature do not alter the subsequent crack growth rate.

The variations in growth rate are typical of the range observed in the material during standard fatigue testing, (Section 5.2.5, Figures 5.32,5.33).

5.2.7.2. Elevated Temperature Fatigue Testing

The most effective method of checking for the effect of temperature on cyclic crack propagation was to determine growth rate at ambient, then to heat the specimen to the required elevated temperature and subject it to the identical applied loading, i.e. a 'change-over' test.

(i) WC-10Co, fine grained (alloy S10)

A typical result for an S10 alloy shows that there is a slight increase in growth rate at 250°C, but that the same loading at 500°C results in a growth rate more than 100 times greater than that measured at ambient temperature. (Figure 5.41).

After cycling at 500°C there is occasionally a no growth situation for a number of cycles. This may be due to crack tip plasticity, created at 500°C, which subsequently retards the propagation at ambient temperature.

Graphs of crack growth rate vs stress intensity range (da/dN vs ΔK_I) were obtained at both 250°C and 500°C although more tests were carried out at 500°C. The scatter is considerable. (Figures 5.42, 5.43).

(ii) WC-10Co, coarse grained (alloy G10)

The 10 wt% cobalt, coarse grained alloy behaves differently to the fine grained equivalent. Below a certain stress intensity range there is no increase in the growth rate due to the elevated temperature. However once above this ΔK_I level the increase is considerable and on a par with that observed in alloy

S10. Thus a negligible increase in da/dN is shown at ΔK_I = 8,47 $MNm^{-3/2}$ but at a stress intensity range only slightly greater, ΔK_I = 8,97 $MNm^{-3/2}$, a marked increase in growth rate is apparent (Figure 5.44, 5.45).

Tests at 250°C show no change in da/dN.

After the 500°C loading a region of retarded growth normally occurs. When the data from tests at 500°C are plotted in the form of a da/dN vs ΔK_I graph, it appears that the elevated temperature only influences the crack growth rate at a stress intensity range greater than ~9 $MNm^{-3/2}$. (Figure 5.46).

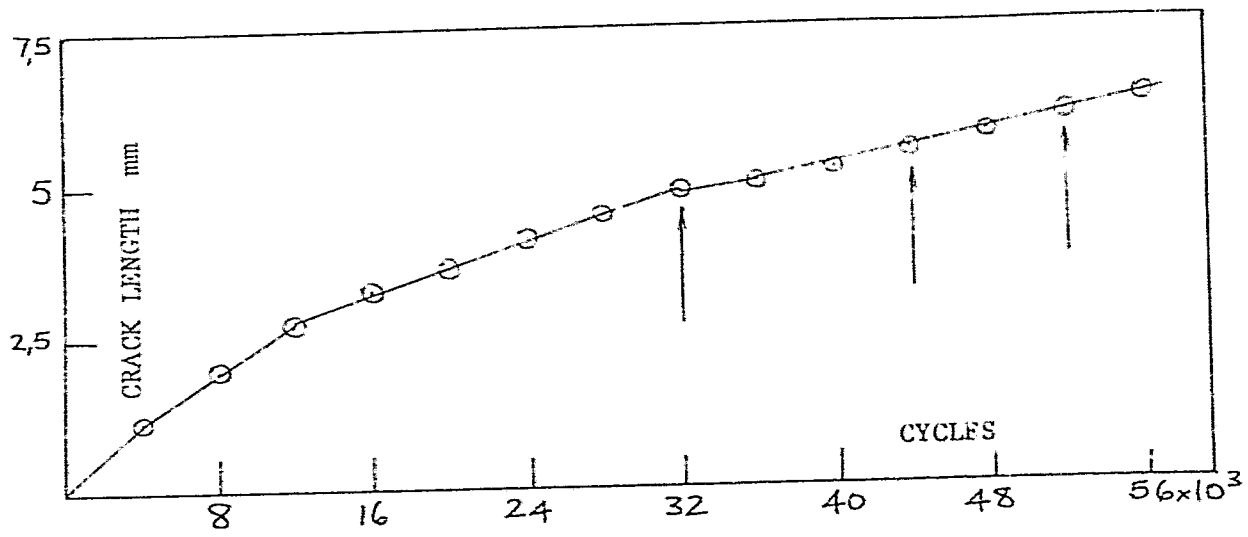

VARIATION IN CRACK GROWTH DUE TO HEATING ONLY IN TWO SPECIMENS. RESULTS SHOW NO EFFECT DUE TO THE HEAT-UP COOL-DOWN CYCLE.
Alloy S10, WC-10Co fine grained

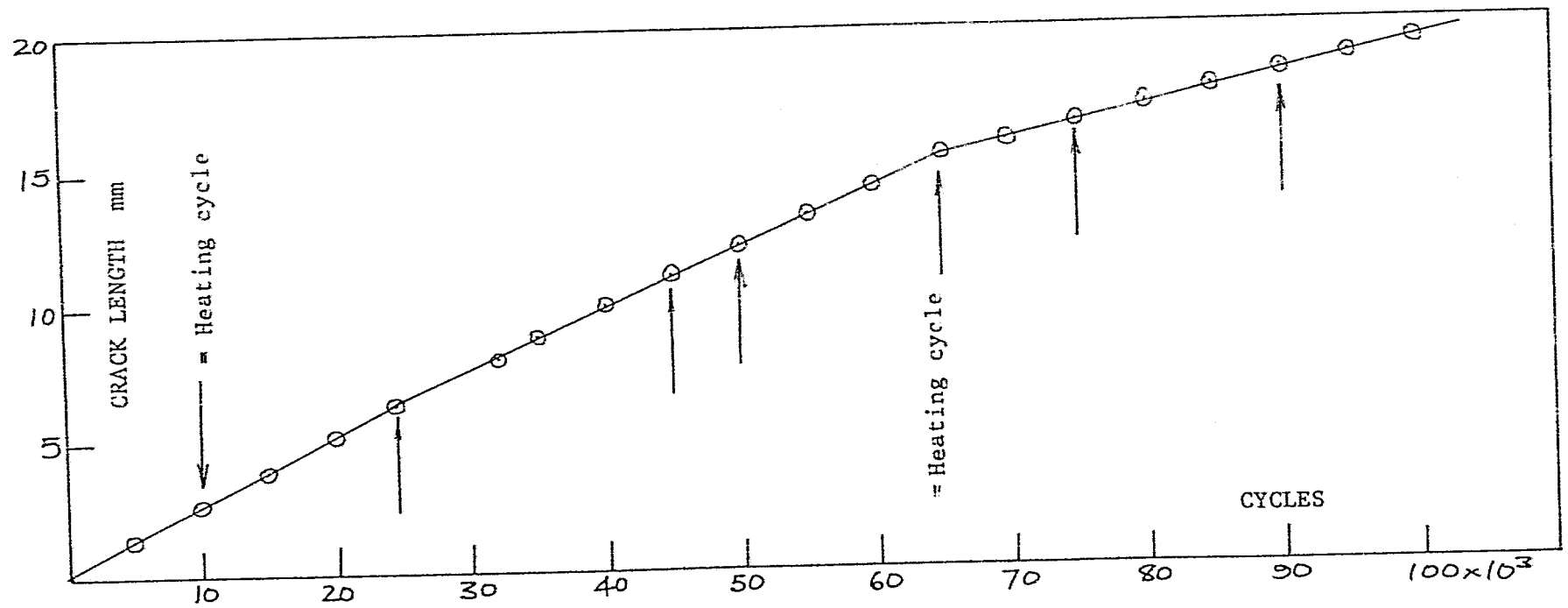

Figure 5.40

GRAPH SHOWING TYPICAL VARIATION IN FATIGUE
CRACK GROWTH WITH TEMPERATURE
Alloy S10, WC-10Co fine grained

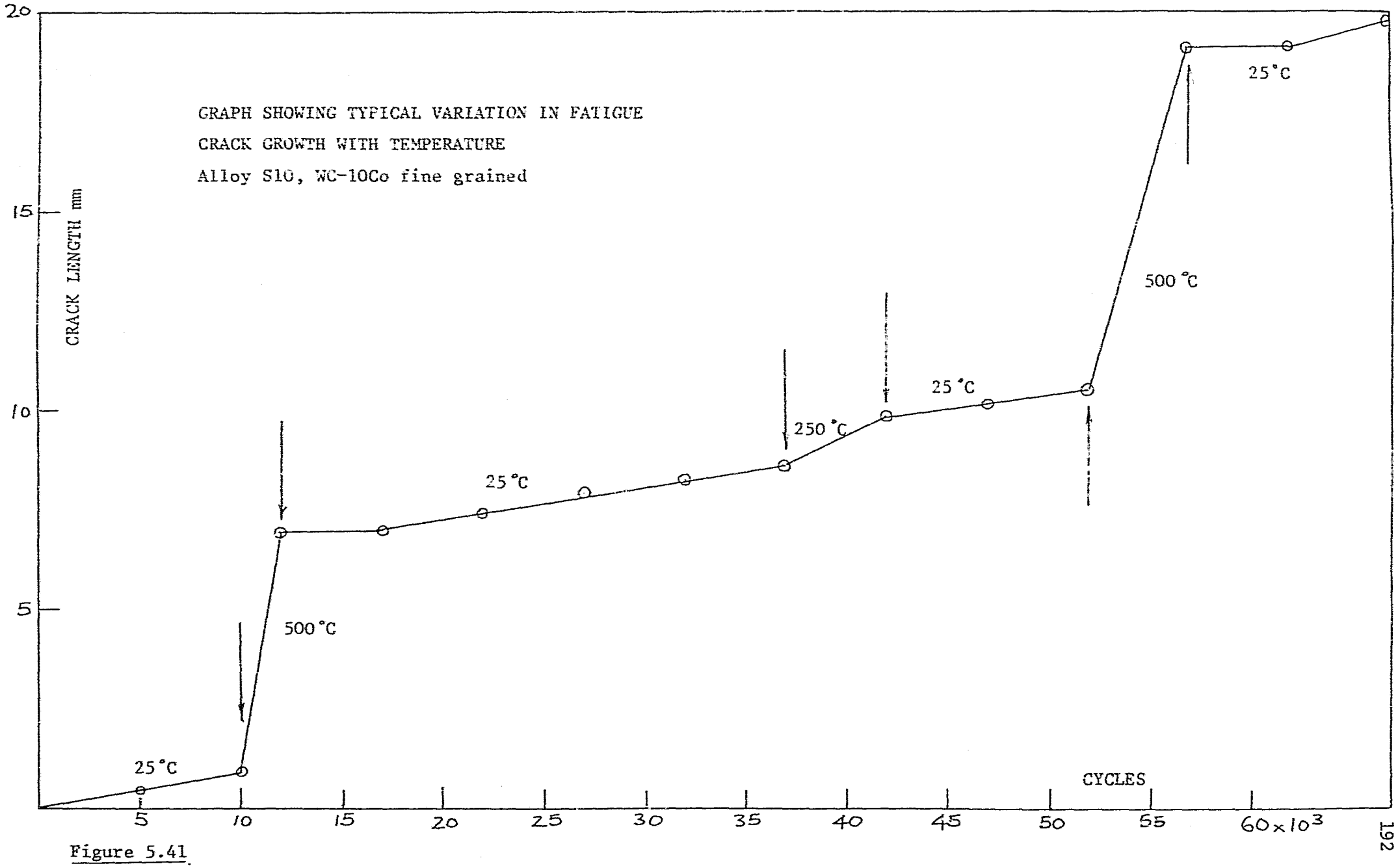

Figure 5.41

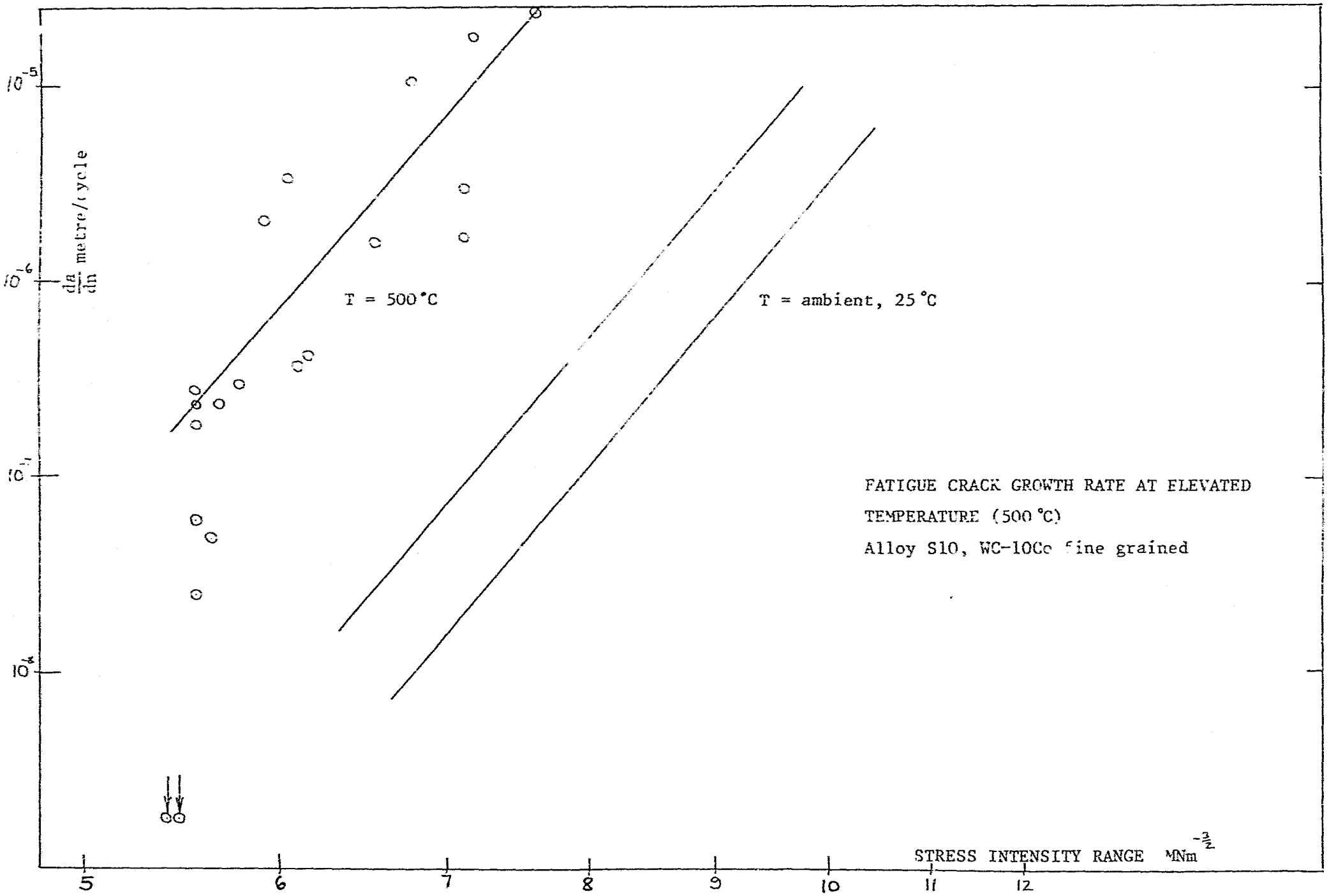
10^{-5}
10^{-6}
$\frac{da}{dn}$ metre/cycle
T = 500°C
T = ambient, 25°C
FATIGUE CRACK GROWTH RATE AT ELEVATED TEMPERATURE (500°C)
Alloy S10, WC-10Co fine grained
STRESS INTENSITY RANGE $MNm^{-\frac{3}{2}}$
5
6
7
8
9
10
11
12

Figure 5.42

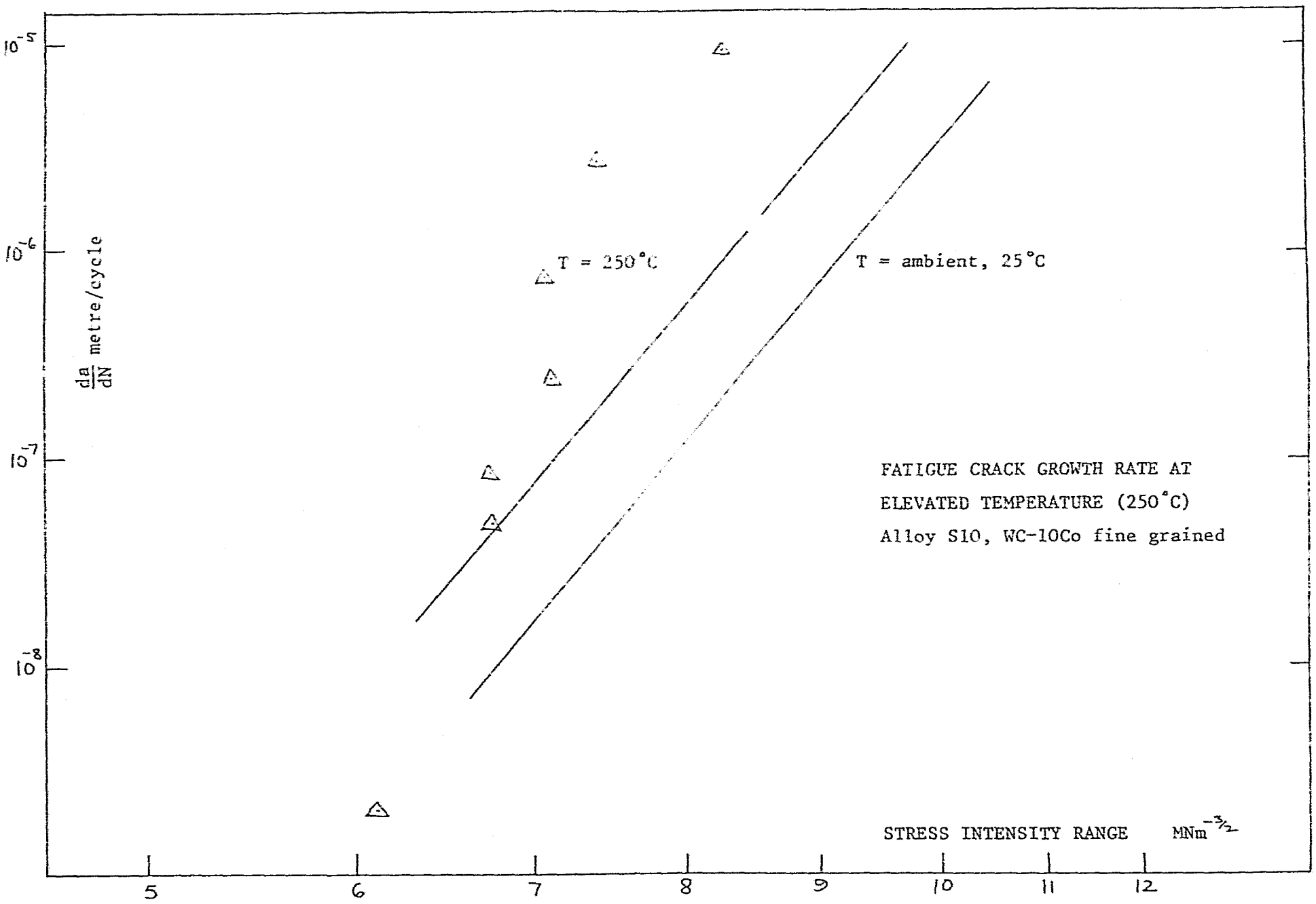
10^{-5}
10^{-6}
10^{-7}
10^{-8}
$\frac{da}{dN}$ metre/cycle
T = 250°C
T = ambient, 25°C
FATIGUE CRACK GROWTH RATE AT
ELEVATED TEMPERATURE (250°C)
Alloy S10, WC-10Co fine grained
STRESS INTENSITY RANGE $MNm^{-3/2}$
5
6
7
8
9
10
11
12

Figure 5.43

GRAPH SHOWING TYPICAL VARIATION IN FATIGUE
CRACK GROWTH WITH TEMPERATURE FOR ΔK_I = 8,471 MNm$^{-3/2}$
(R < 0,1) - VERY SMALL CHANGE IN CRACK GROWTH RATE
AT 500 °C AND THIS STRESS INTENSITY RANGE
Alloy G10, WC-10Co coarse grained

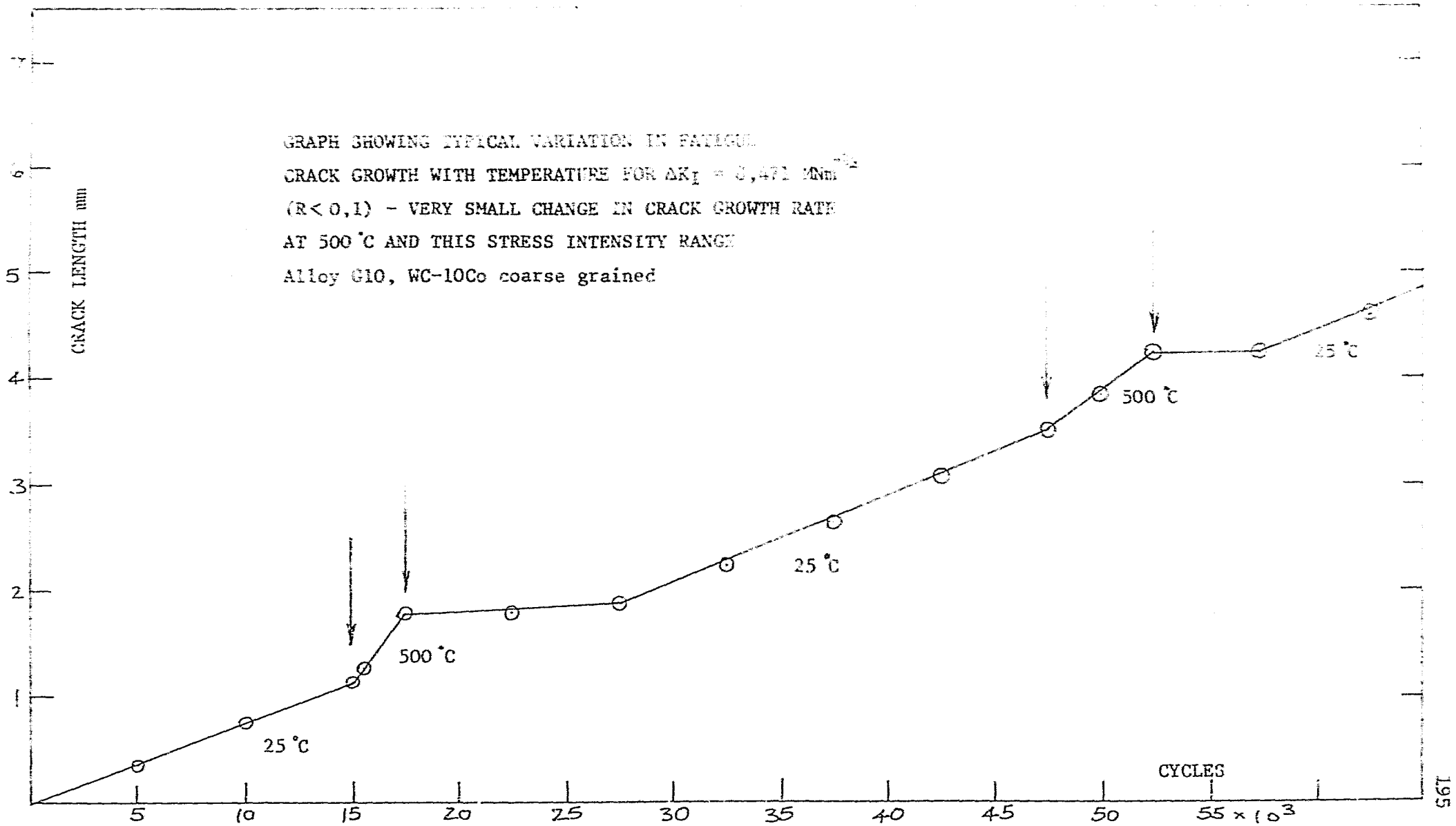

Figure 5.44

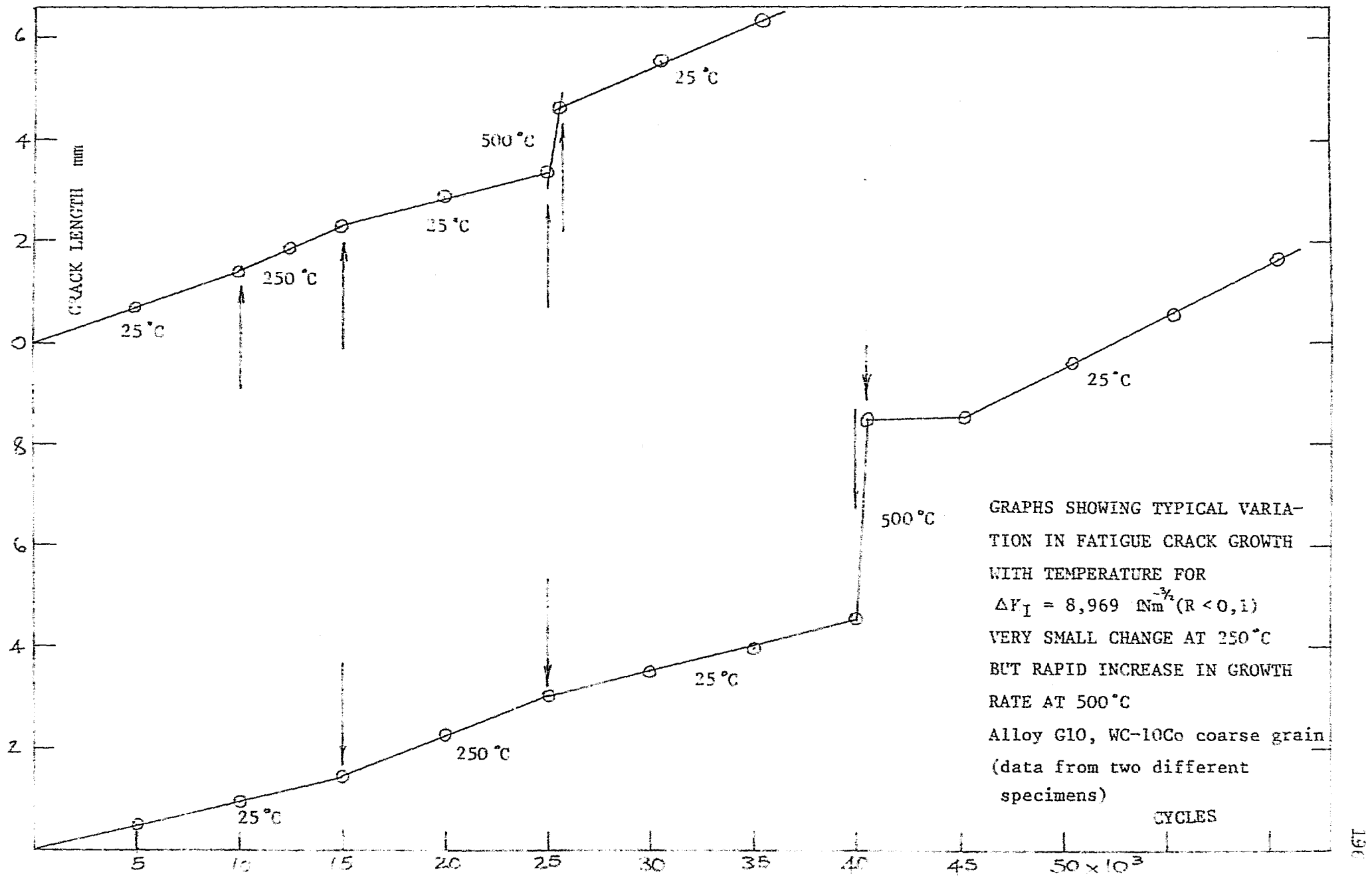

GRAPHS SHOWING TYPICAL VARIATION IN FATIGUE CRACK GROWTH WITH TEMPERATURE FOR $\Delta K_I = 8{,}969$ MNm$^{-3/2}$ ($R < 0{,}1$)
VERY SMALL CHANGE AT 250°C BUT RAPID INCREASE IN GROWTH RATE AT 500°C
Alloy G10, WC-10Co coarse grain (data from two different specimens)

Figure 3.45

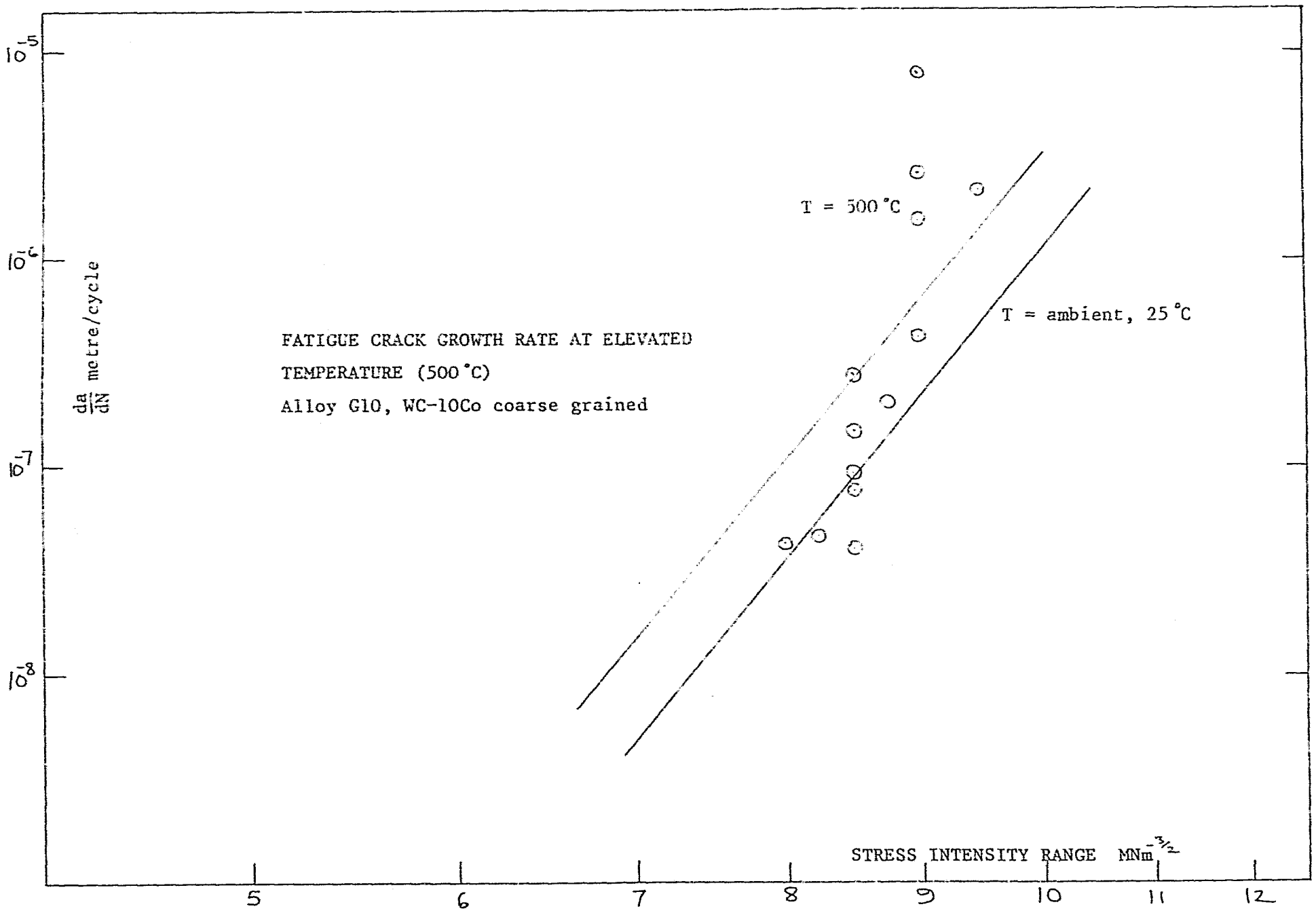
10^{-5}
10^{-6}
10^{-7}
10^{-8}
$\frac{da}{dN}$ metre/cycle
FATIGUE CRACK GROWTH RATE AT ELEVATED
TEMPERATURE (500 °C)
Alloy G10, WC-10Co coarse grained
T = 500 °C
T = ambient, 25 °C
STRESS INTENSITY RANGE MNm$^{-3/2}$
5
6
7
8
9
10
11
12

Figure 5.46

5.3 FRACTURE TOUGHNESS

Fracture toughness measurements were made on the alloys tested by loading the specimens to failure, under stroke control, at a ramp rate of 0,05 mm/sec.

The toughness increases approximately linearly with mean free path and decreases as hardness increases. (Table 5.1, Figures 5.47 - 5.49).

The number of K_{IC} results per alloy is small due to the high cost of the specimens.

Table 5.1

FRACTURE TOUGHNESS AND MICROSTRUCTURAL DETAILS OF ALLOYS TESTED

Alloy	$\bar{d}$ µm	λ_{nom} µm	λ_{true} µm	HV 30 kg mm^{-2}	K_{IC} (mean) MNm$^{-3/2}$	No. of tests
S6	1,0	0,093	0,186	1541	8,22	2
S10	1,1	0,216	0,338	1337	9,17	2
G6	2,9	0,327	0,654	1377	10,03	2
G10	3,1	0,608	0,950	1215	11,32	3
G15	3,5	1,090	1,453	1043	13,26	1
25E	3,2	1,882	2,163	798	15,68	2

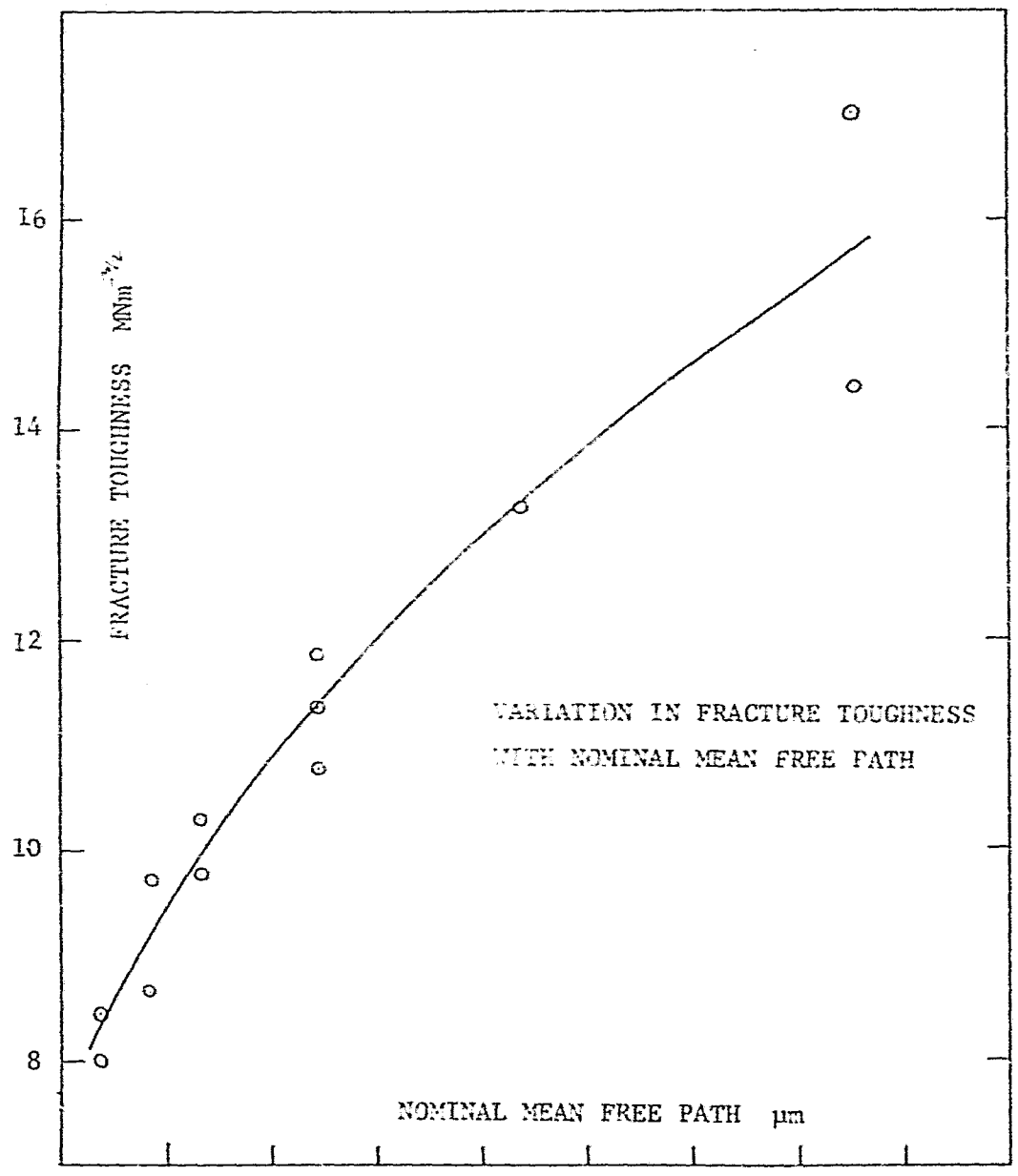

Figure 5.47

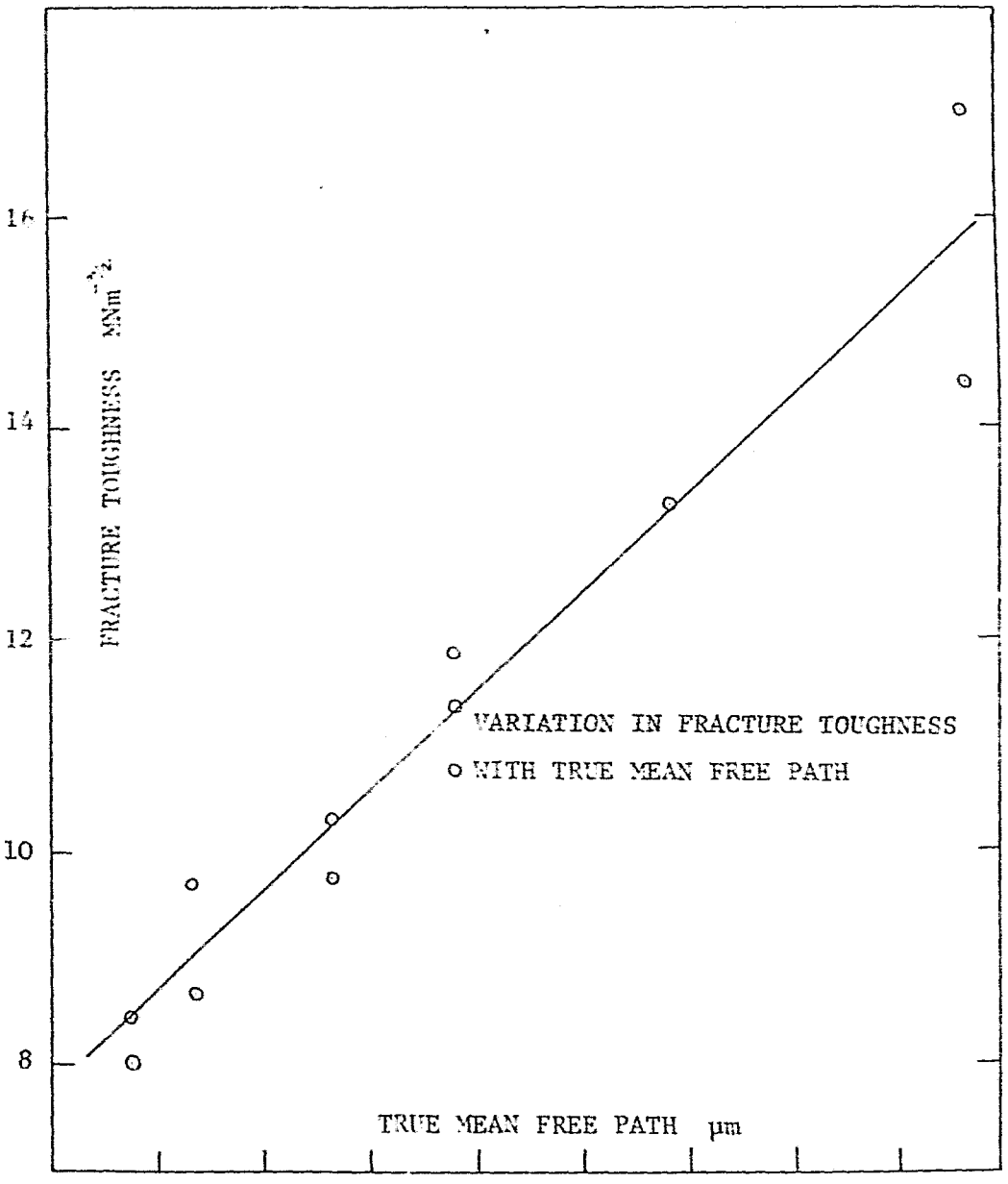

Figure 5.48

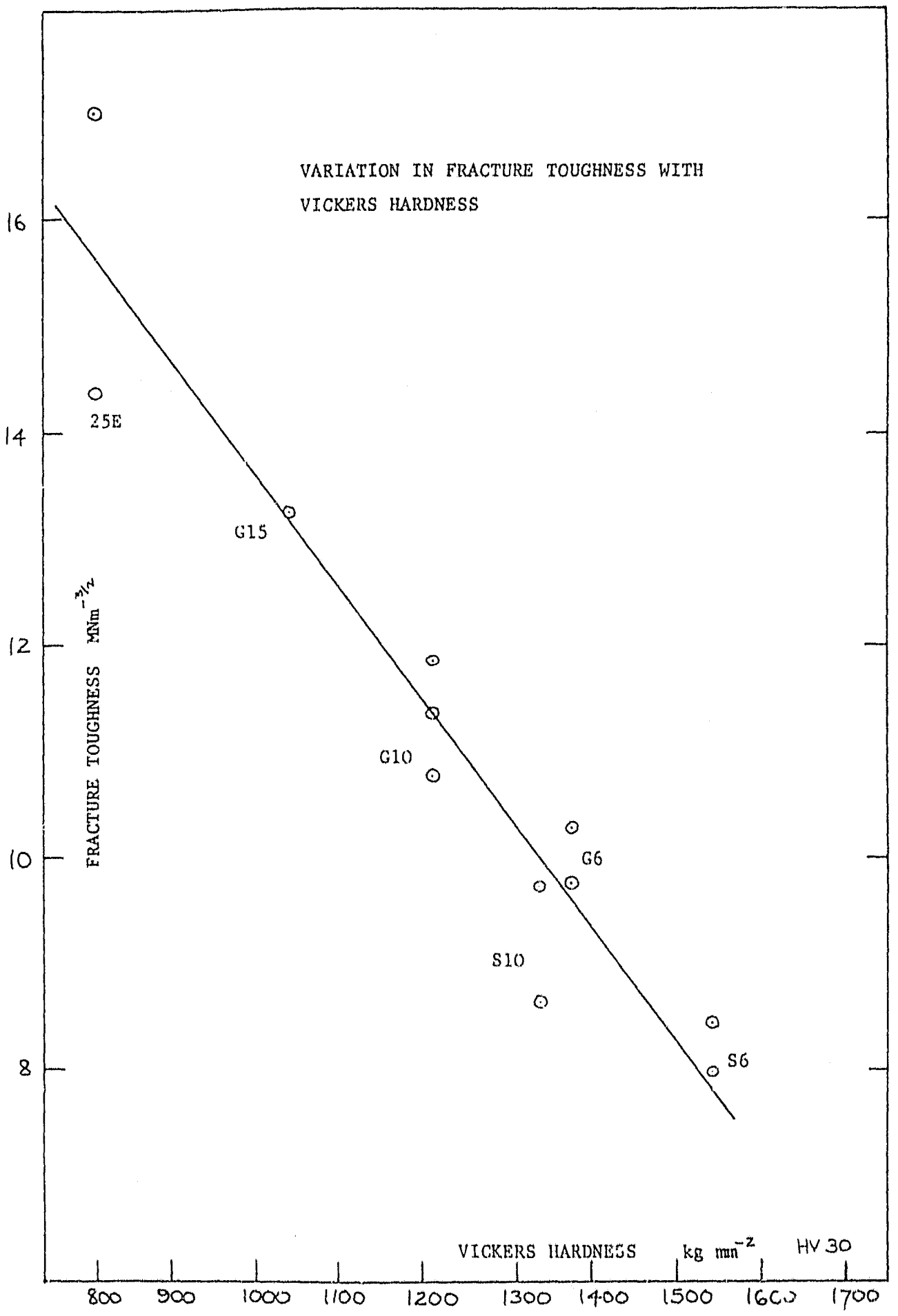
VARIATION IN FRACTURE TOUGHNESS WITH
VICKERS HARDNESS
FRACTURE TOUGHNESS MNm$^{-3/2}$
16
14
12
10
8
25E
G15
G10
G6
S10
S6
VICKERS HARDNESS kg mm^{-2} HV 30
800
900
1000
1100
1200
1300
1400
1500
1600
1700

Figure 5.49

5.4 FRACTOGRAPHY

Scanning electron microscopy was carried out on all the grades tested for three different fracture modes:

(i) Fatigue at R ratio < 0,02
(ii) Fatigue at R ratio ≈ 0,6
(iii) Fast fracture

It was immediately apparent that careful preparation of the sample and suitable protection of the fracture is vital in order to ensure reasonable results. Figures 5.50 and 5.51 illustrate the hopeless situation when the surfaces are degraded during cutting. It is clearly impossible to interpret poor quality fractographs; for example, compare Figures 5.50 and 5.51 with 5.54. The definition in the coarse grained alloy fractographs is considerably better than in the fine grained, as would be expected.

The fractographs show that there are no distinguishable differences between the fracture surface morphologies of fatigue and catastrophic crack propagation, in any of the alloys tested. (Figures 5.52 - 5.57).

Primarily intergranular fracture with the formation of ductile dimples in the binder phase and transgranular cracking of large carbide grains is characteristic of both the fatigue and fast crack propagation.

G6 6 wt% cobalt, coarse grained.

FAST FRACTURE

Surface not protected and cut out of specimen using water coolant. Ultrasonically cleaned in acetone.

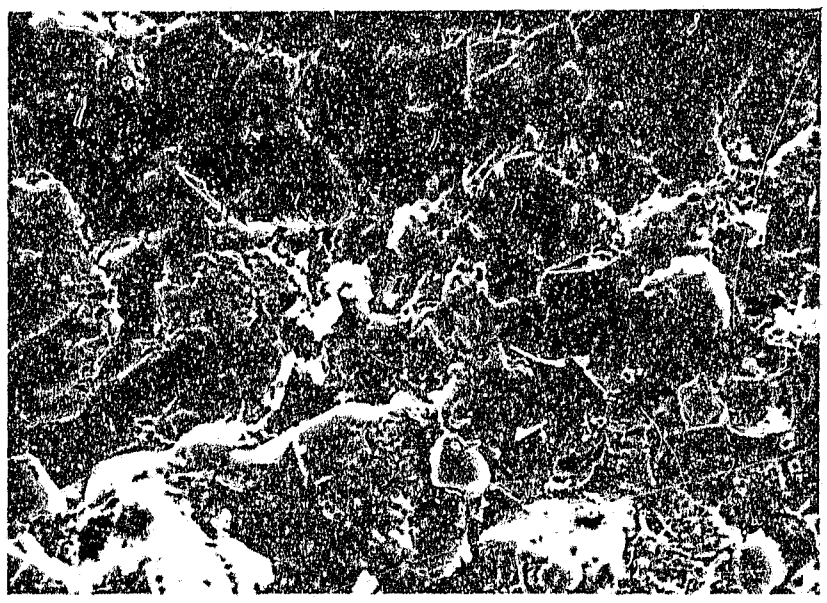

4 μm

Figure 5.50

FAST FRACTURE

Surface protected with 101 Lettraset protective coating. Ultrasonically cleaned in acetone.

4 μm

Figure 5.51

Figure 5.52 S6 6 wt% cobalt fine grained

(i) FAST FRACTURE

K_{IC} = 7,99 $MNm^{-3/2}$

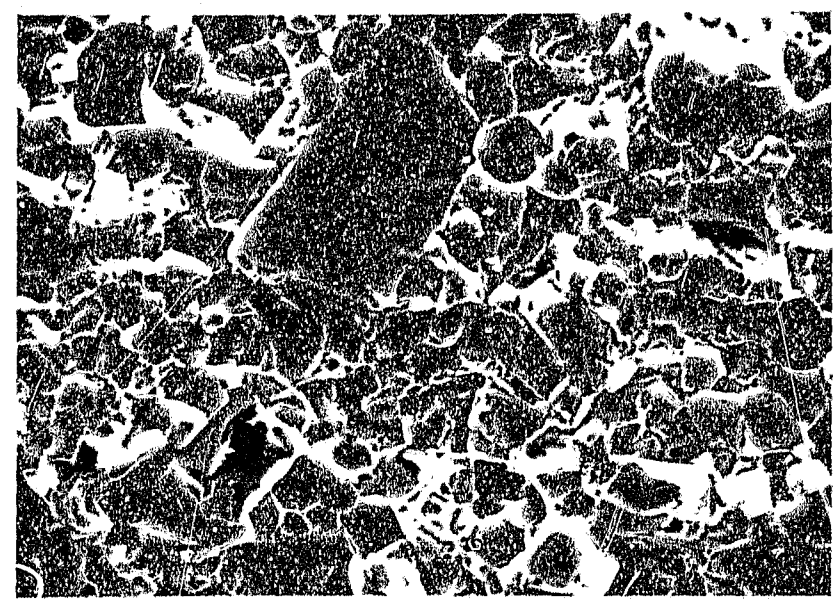

4 µm

(ii) FATIGUE

ΔK_I = 7,22 $MNm^{-3/2}$

K_{Imax} = 7,37 $MNm^{-3/2}$

R = 0,020

da/dN = 1,96 x 10^{-6} m/cycle

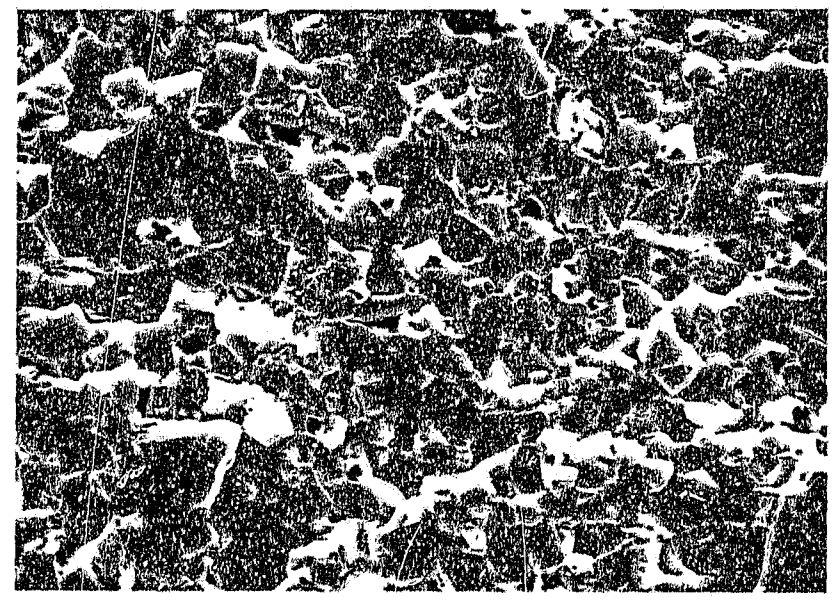

4 µm

(iii) FATIGUE

ΔK_I = 3,00 $MNm^{-3/2}$

K_{Imax} = 7,49 $MNm^{-3/2}$

R = 0,60

da/dN = 1,32 x 10^{-6} m/cycle

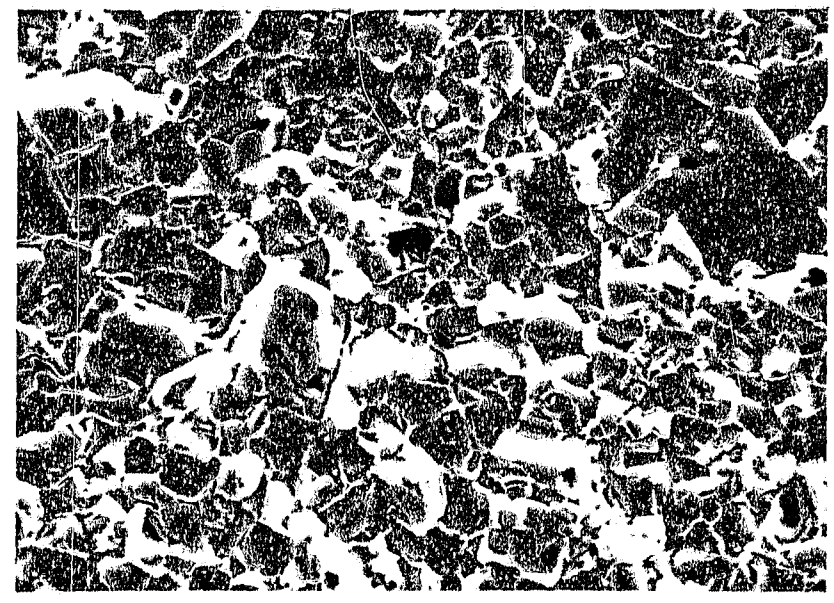

4 µm

Figure 5.53 S10 10 wt% cobalt fine grained

(i) FAST FRACTURE

K_{IC} = 9,71 $MNm^{-3/2}$

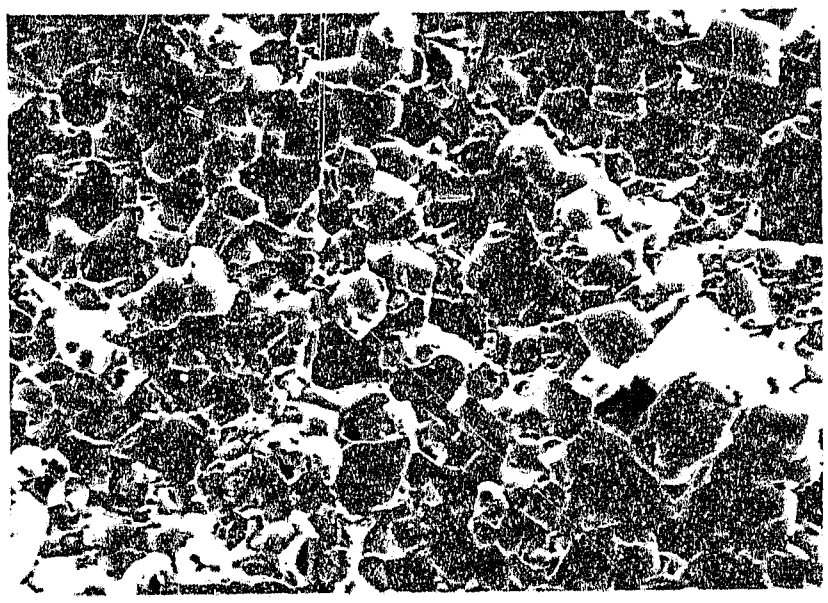

4 µm

(ii) FATIGUE

ΔK_I = 8,59 $MNm^{-3/2}$

K_{Imax} = 8,70 $MNm^{-3/2}$

R = 0,013

da/dN = 1,99 x 10^{-6} m/cycle

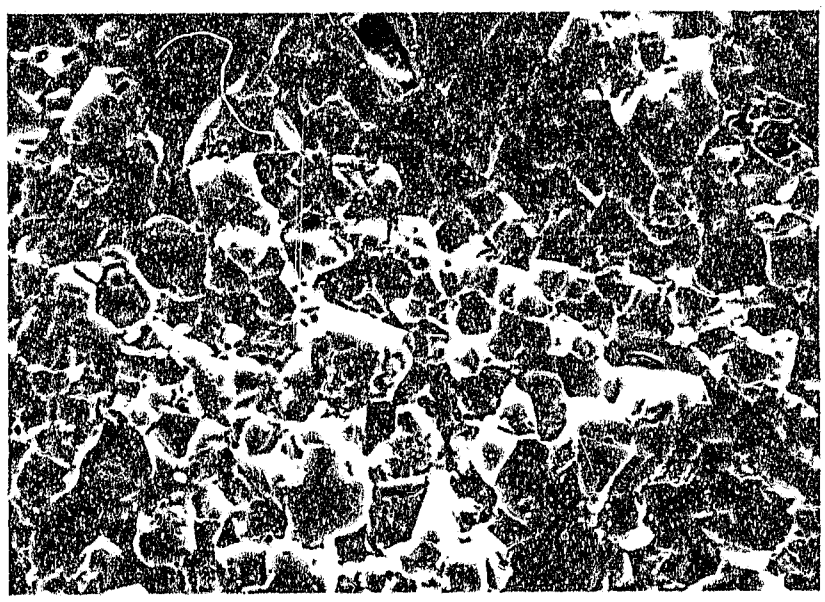

4 µm

(iii) FATIGUE

ΔK_I = 3,66 $MNm^{-3/2}$

K_{Imax} = 9,16 $MNm^{-3/2}$

R = 0,60

da/dN = 1,00 x 10^{-6} m/cycle

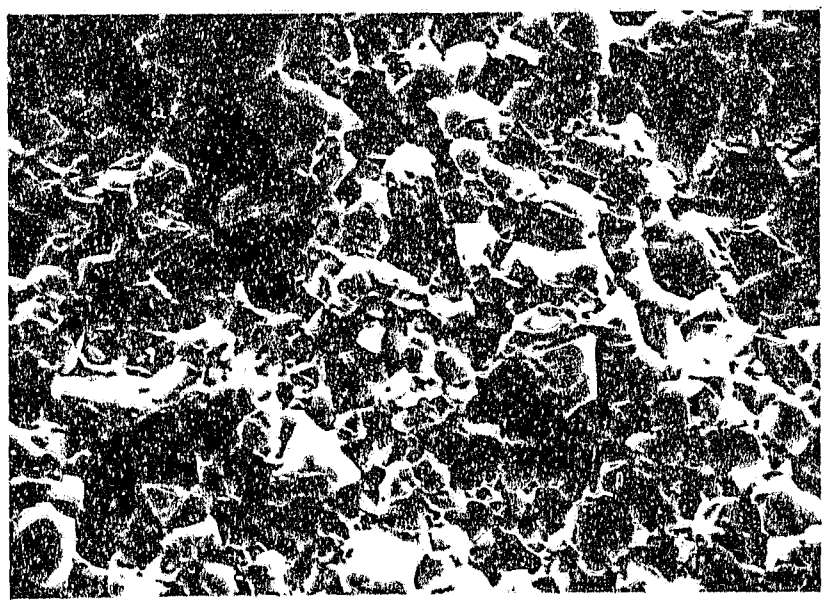

4 µm

Figure 5.54 G6 6 wt% cobalt coarse grained

(i) FAST FRACTURE

K_{IC} = 10,29 $MNm^{-3/2}$

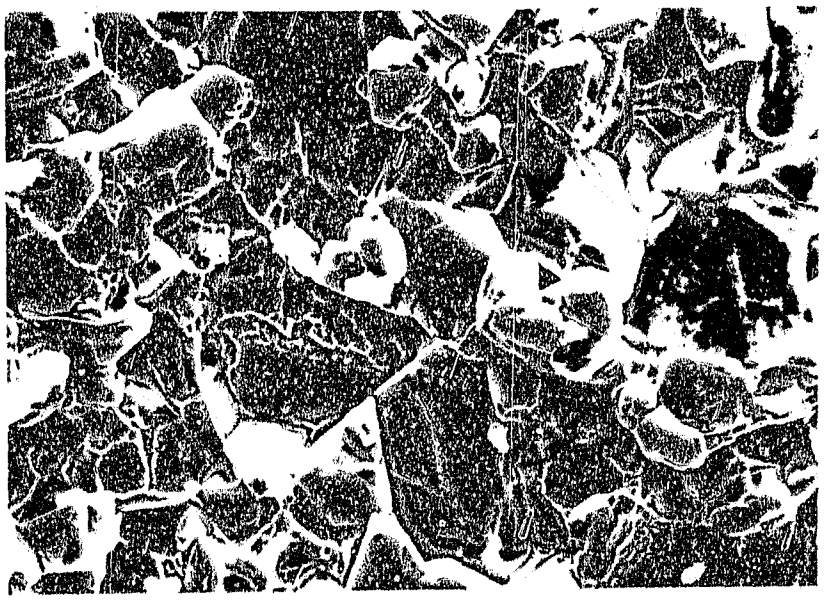

4 µm

(ii) FATIGUE

ΔK_I = 9,22 $MNm^{-3/2}$

K_{Imax} = 9,34 $MNm^{-3/2}$

R = 0,014

da/dN = 1,19 x 10^{-6} m/cycle

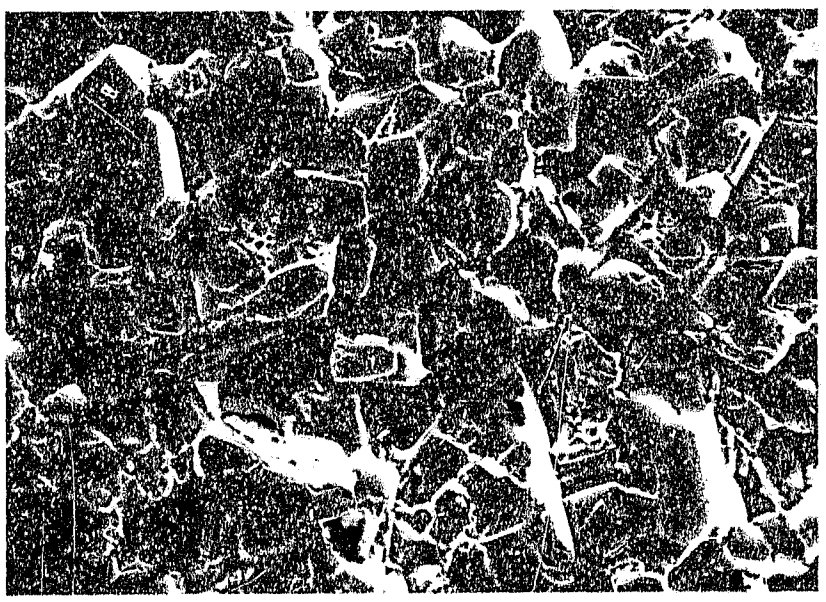

4 µm

(iii) FATIGUE

ΔK_I = 4,04 $MNm^{-3/2}$

K_{Imax} = 9,85 $MNm^{-3/2}$

R = 0,62

da/dN = 9,37 x 10^{-7} m/cycle

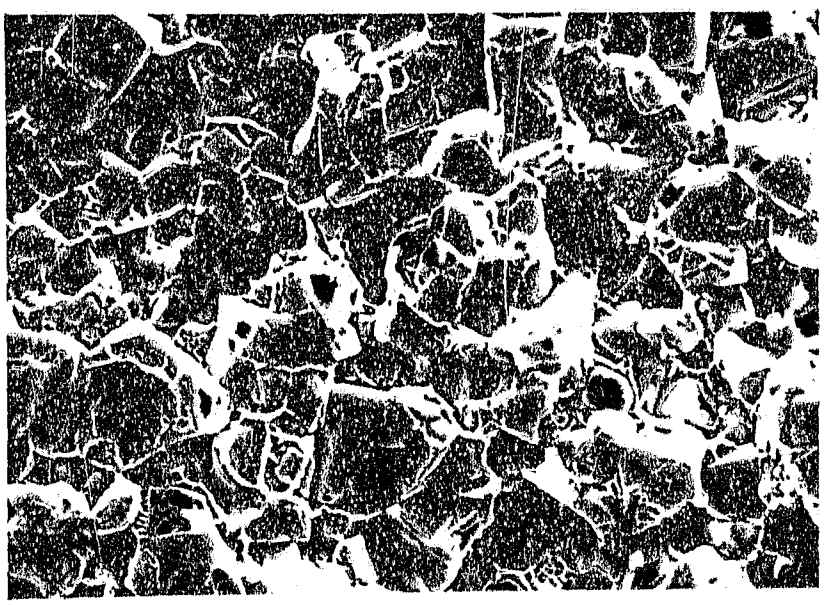

4 µm

Figure 5.55 G10 10 wt% cobalt coarse grained

(i) FAST FRACTURE

K_{IC} = 10,75 $MNm^{-3/2}$

4 µm

(ii) FATIGUE

ΔK_I = 9,33 $MNm^{-3/2}$

K_{Imax} = 9,46 $MNm^{-3/2}$

R = 0,013

da/dN = 1,94 x 10^{-6} m/cycle

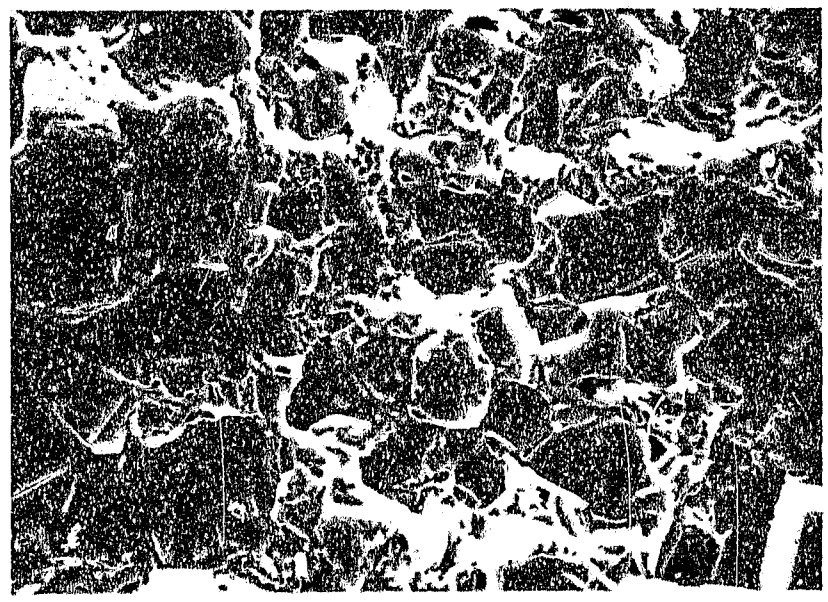

4 µm

(iii) FATIGUE

ΔK_I = 3,98 $MNm^{-3/2}$

K_{Imax} = 10,20 $MNm^{-3/2}$

R = 0,61

da/dN = 8,19 x 10^{-7} m/cycle

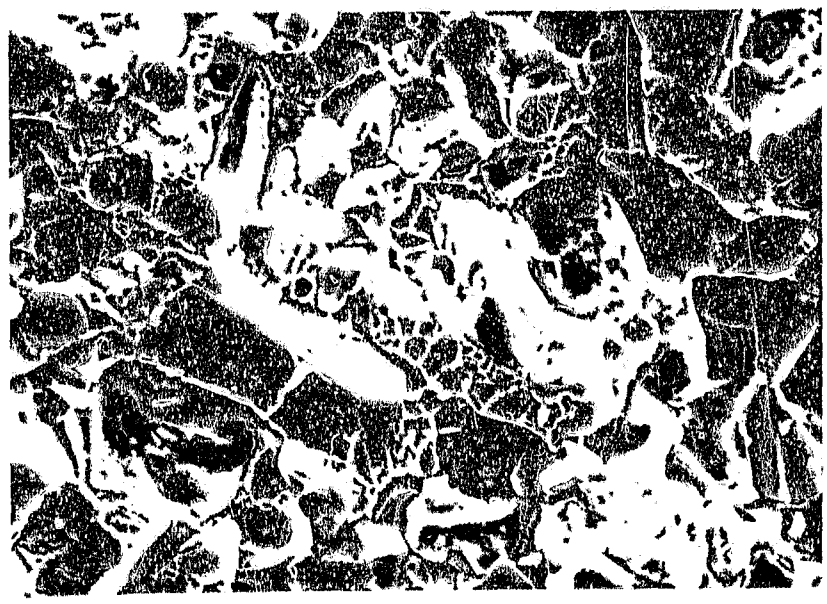

4 µm

FAST FRACTURE

K_{FC} = 13,26 MNm$^{-3/2}$

4 µm

ATTACK

ΔK_I = 10,99 MNm$^{-3/2}$

K_{max} = 11,11 MNm$^{-3/2}$

R = 0,017

da/dN = 1,77 x 10^{-6} m/cycle

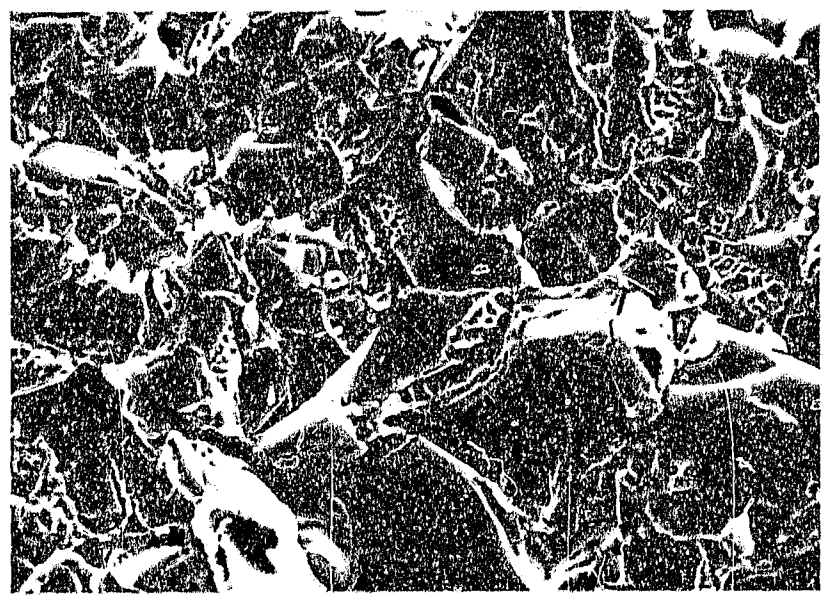

4 µm

ATTACK

ΔK_I = 4,94 MNm$^{-3/2}$

K_{max} = 12,10 MNm$^{-3/2}$

R = 0,59

da/dN = 1,15 x 10^{-6} m/cycle

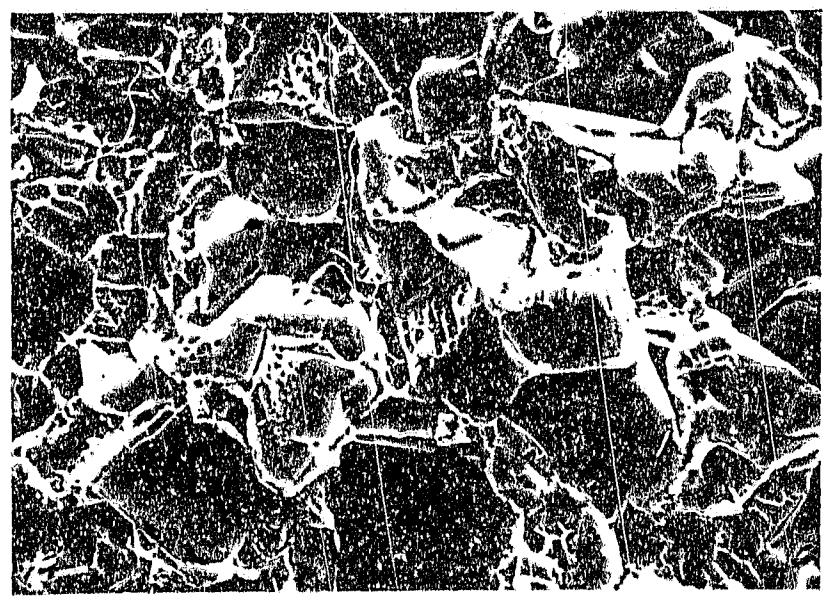

4 µm

Figure 5.57 25E 25 wt% cobalt coarse grained

(i) FAST FRACTURE

K_{IC} = 14,37 $MNm^{-3/2}$

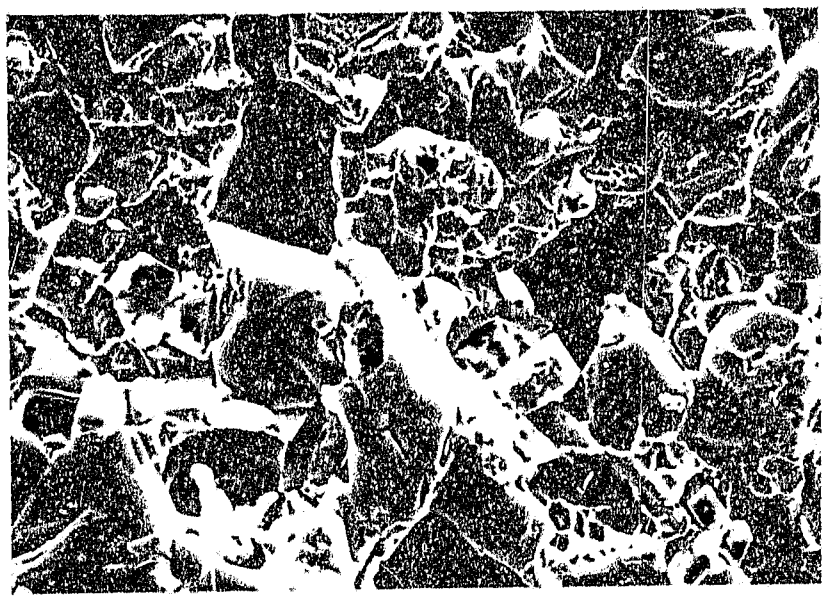

4 µm

(ii) FATIGUE

ΔK_I = 11,29 $MNm^{-3/2}$

K_{Imax} = 11,41 $MNm^{-3/2}$

R = 0,011

da/dN = 9,55 x 10^{-7} m/cycle

4 µm

(iii) FATIGUE

ΔK_I = 4,61 $MNm^{-3/2}$

K_{Imax} = 13,59 $MNm^{-3/2}$

R = 0,66

da/dN = 1,50 x 10^{-6} m/cycle

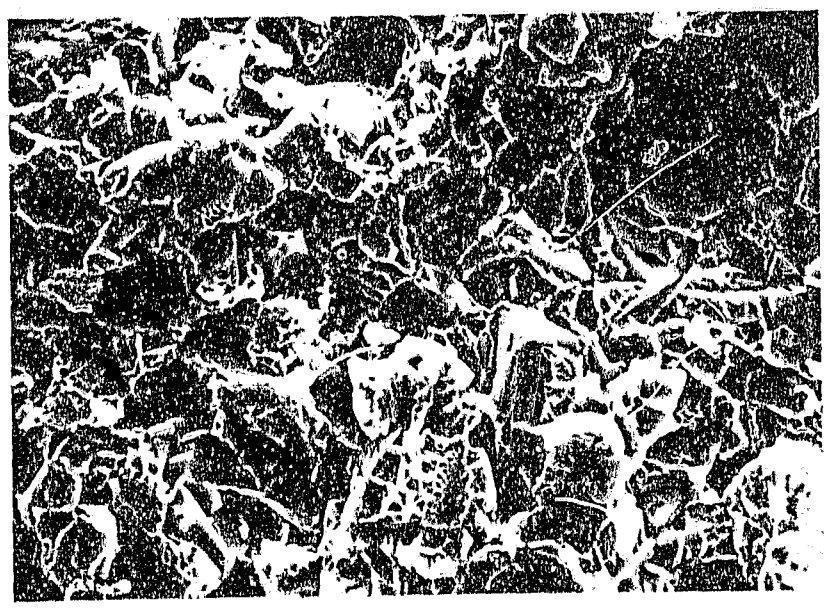

4 µm

6 DISCUSSION

6.1 INTRODUCTION

It has been unequivocally proven that crack propagation by cyclic fatigue occurs in tungsten carbide-cobalt hardmetal alloys. There is however no immediately obvious explanation for this behaviour, particularly as the fracture morphologies of fatigue and fast fracture are indistinguishable.

Both the static and fatigue crack growth rates determined are slightly greater than results reported in the literature for similar alloy compositions,[103,109-111] i.e. crack propagation occurs at lower stress intensity values. (Figures 6.1, 6.2). The absolute differences are, however, not great and the effects of cobalt content and mean stress intensity are in complete agreement. The observations and data summarised in the following sections can therefore be assumed to be valid, and hence form a sound basis for the subsequent discussion.

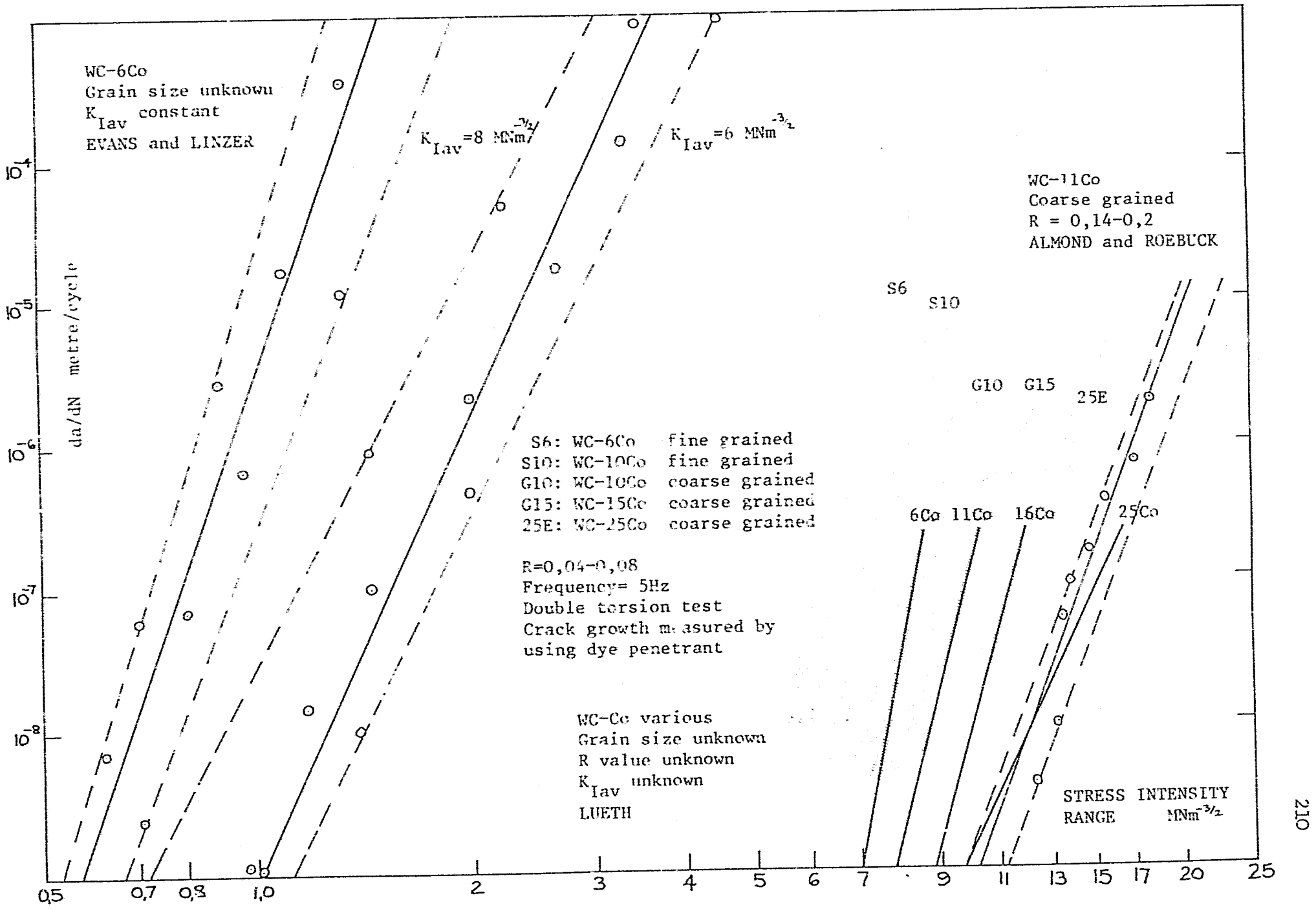
WC-6Co
Grain size unknown
K_{Iav} constant
EVANS and LINZER
K_{Iav}=8 MNm$^{-3/2}$
K_{Iav}=6 MNm$^{-3/2}$
WC-11Co
Coarse grained
R = 0,14-0,2
ALMOND and ROEBUCK
S6
S10
G10
G15
25E
S6: WC-6Co fine grained
S10: WC-10Co fine grained
G10: WC-10Co coarse grained
G15: WC-15Co coarse grained
25E: WC-25Co coarse grained
R=0,04-0,08
Frequency= 5Hz
Double torsion test
Crack growth measured by
using dye penetrant
WC-Co various
Grain size unknown
R value unknown
K_{Iav} unknown
LUETH
6Co
11Co
16Co
25Co
da/dN metre/cycle
10^{-4}
10^{-5}
10^{-6}
10^{-7}
10^{-8}
0,5
0,7
0,8
1,0
2
3
4
5
6
7
9
11
13
15
17
20
25
STRESS INTENSITY
RANGE MNm$^{-3/2}$

Figure 6.1

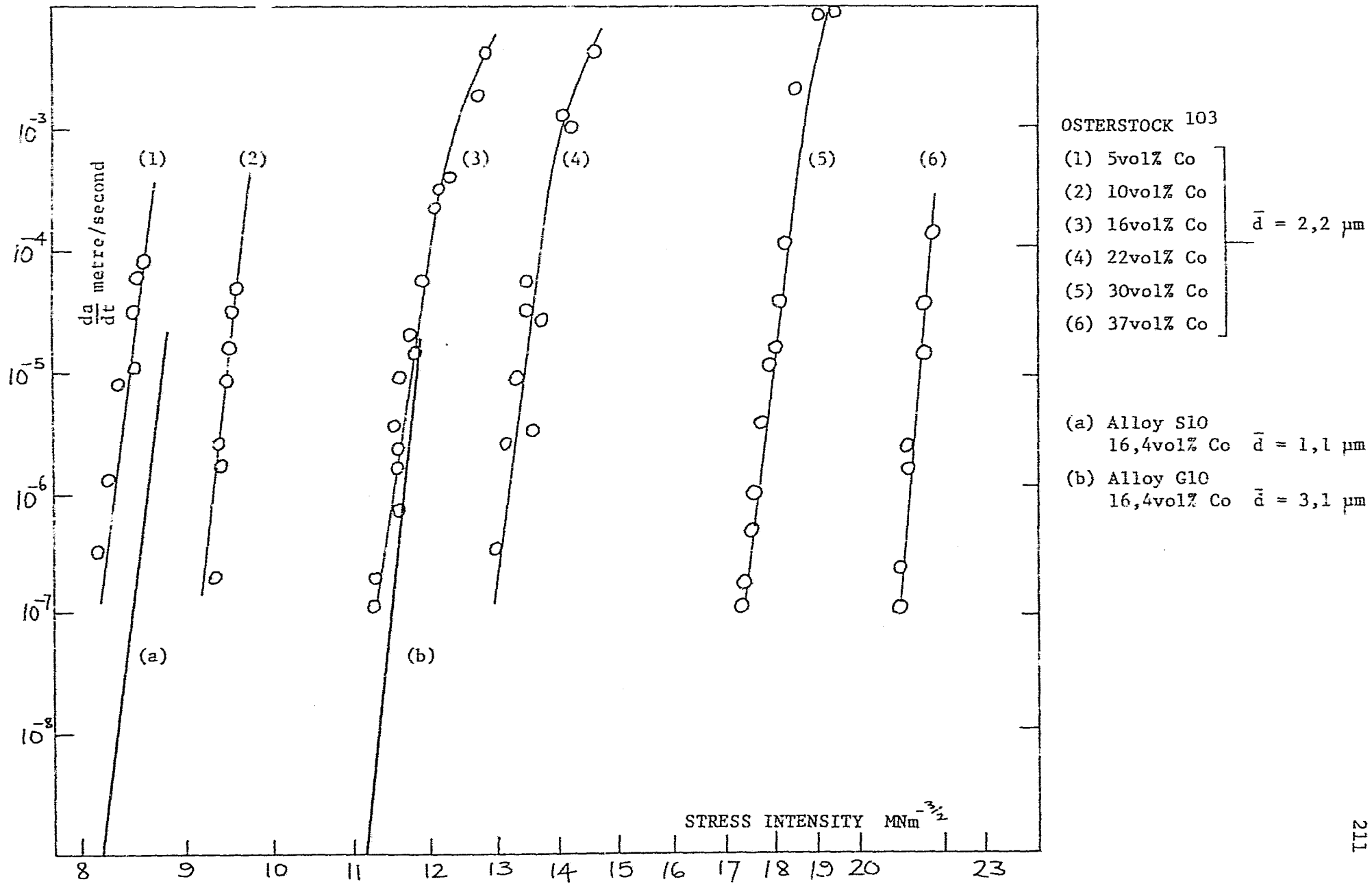
10^{-3}
10^{-4}
10^{-5}
10^{-6}
10^{-7}
10^{-8}
$\frac{da}{dt}$ metre/second
(1)
(2)
(3)
(4)
(5)
(6)
(a)
(b)
8
9
10
11
12
13
14
15
16
17
18
19
20
23
STRESS INTENSITY $MNm^{-3/2}$
OSTERSTOCK 103
(1) 5vol% Co
(2) 10vol% Co
(3) 16vol% Co
(4) 22vol% Co
(5) 30vol% Co
(6) 37vol% Co
$\bar{d}$ = 2,2 μm
(a) Alloy S10
16,4vol% Co $\bar{d}$ = 1,1 μm
(b) Alloy G10
16,4vol% Co $\bar{d}$ = 3,1 μm

Figure 6.2

6.2 CRACK GROWTH UNDER STATIC LOADING

6.2.1 Background

Static crack growth is by definition a time dependent phenomenon, normally associated with environmentally assisted fracture mechanisms. Thus, such subcritical crack growth is normally associated with phenomena such as stress corrosion cracking in metals and hydrogen ion attack in glasses and ceramics.[147, 157]

In conventional metal systems at temperatures low compared to the melting point, static load stable crack growth does not occur unless an environmental mechanism operates. However crack propagation studies in vacuum have shown that slow crack growth is possible in glass even in the absence of a corrosive environment.[157,158] In this rather exceptional case crack growth is a thermally activated process in which atomic bonds are ruptured by additional displacements caused by thermal fluctuations at the crack tip.[157]

6.2.2 Static Crack Growth Rate

Two alloys, S10 and G10, were monotonically loaded in air at room temperature using dye penetrant to monitor crack growth. The results, which confirm those reported by Osterstock,[103] show that static crack growth does not occur below a stress intensity of $\sim 0{,}9K_{IC}$ and that the exponent 'n' in the equation $da/dt = A(K_I)^n$ has a value in the range 125 - 200.

There is no evidence to indicate whether this is an environmental effect or not. The laboratory air and/or the dye penetrant may constitute a sufficiently aggressive environment to cause subcritical cracking at stress intensities close to the fracture toughness.

6.2.3 Observations in SEM

Tests were carried out in the high vacuum chamber of a scanning electron microscope to establish whether static crack growth could occur in an inert (vacuum) environment. Fracture and crack arrest are observed (Section 5.12) but do not show unequivocally that stable subcritical cracking is an environmentally-independent phenomenon in WC-Co alloys. There are two reasons for this:

(i) In the test system used the load application is displacement controlled. Immediately crack propagation starts therefore, the applied stress intensity decreases by 'load relaxation'. Results from the large scale tests (Section 5.1.1) show that even in the air environment once $K_I < 0,9\ K_{IC}$ crack propagation ceases, therefore only a small reduction in load is sufficient to cause crack arrest.

(ii) A specimen geometry with a low angle tapered notch has been used so that the thickness of the web increases continuously along the length. (Figure 4.13). The stress intensity is inversely proportional to (web thickness)$^{\frac{1}{2}}$, so that for a given load, as the crack advances and 'sees' a thicker section the effective applied stress intensity decreases and once below the critical value the crack arrests.

It is quite possible therefore that the crack only initiates when the fracture toughness, K_{IC}, is reached. The reduction in stress intensity as the crack propagates prevents catastrophic fracture of the specimen and causes arrest after a small increase in crack length.

Thus, the SEM test observations do not prove that static crack growth occurs in WC-Co alloys at stress intensities below the fracture toughness in an inert environment.

6.3 FATIGUE CRACK PROPAGATION

6.3.1 Fatigue Mechanisms in Metals

It is not feasible here, nor indeed appropriate, to describe or discuss the many mechanisms that have been proposed to account for crack propagation in materials subject to cyclic loading.

There are however a few fundamental principles which are necessary to outline for an understanding of the mechanisms which may lead to fatigue crack propagation in tungsten carbide-cobalt alloys.

Fatigue crack growth rates can frequently be defined by the well established relationship $da/dN = C(\Delta K_I)^m$, (also called the Paris 'law'). The exponent 'm' is widely considered to be a primary indicator of the mechanisms that contribute to crack growth.

Thus, values in the range 2 - 4 are common for ductile materials where crack extension per cycle is likely to vary proportionally to the crack opening displacement (COD) which in turn is a function of the square of the applied stress intensity, ΔK_I.[2,159] The mechanism of growth is largely dependent on the nature of the slip process which operates in the plastic region at the crack tip, with crack growth primarily dominated by the reversed cyclic stress intensity, ΔK_I.

It is however possible for 'static modes' of fracture such as brittle cleavage and microvoid coalescence to contribute to the overall cyclic crack growth.[160,161] These are effectively superimposed on the 'conventional' fatigue. These monotonic modes of fracture are different, and must not be confused with, static crack growth due to effects such as stress corrosion or hydrogen cracking. Materials in which these modes of fracture operate can often be identified by fatigue crack growth rates which have:

(i) relatively high values of the exponent 'm', and
(ii) a mean stress intensity dependence.

Static or monotonic modes of fracture during a fatigue cycle depend only on the maximum stress level reached at the crack tip. The apparent mean stress intensity, K_{Iav}, dependence in fact only reflects the influence of the maximum stress intensity, K_{Imax}, and is not in itself a controlling parameter.[161]

If static fracture modes operate the additional contribution to crack advance per cycle results in the high 'm' values. For example, in aluminium alloys as strength increases, toughness decreases and 'm' increases,[160] and in high strength steels values of 'm' up to 10 have been reported.[162-164]

The monotonic and cyclic mechanisms of fatigue are dependent only on the maximum stress intensity and stress intensity range of the load cycle. The crack growth rate, da/dN, is therefore independent of frequency. Crack growth rates that show a variation with frequency normally result from time dependent contributions to crack growth (Section 6.2) but in some materials may be due to strain rate effects.

Thus, if fatigue crack growth rates are unaffected by variations in frequency, it is unlikely that environmentally assisted fracture (which can also lead to static crack growth) is occurring.

6.3.2 Fatigue Crack Growth Rate Results in WC-Co Alloys

The results obtained which are relevant to the discussion on fatigue mechanims in WC-Co alloys are briefly summarised below:

(i) Fatigue crack growth rates in all alloys tested incr. se with increasing stress intensity range in accordance with a so-called Paris 'law' of

the form $da/dN = C(\Delta K_I)^m$, but are also a function of the mean stress intensity. (Sections 5.2.1, 5.2.2).

(ii) Fatigue crack growth rates decrease as the mean free path of the cobalt binder increases. (Figures 5.7 - 5.9).

(iii) The values of the exponent 'm' are in the range 10 - 20, increasing as the mean free path decreases or mean stress intensity increases. (Figures 5.10, 5.16 - 5.18).

(iv) Fatigue crack growth rates increase dramatically when the maximum stress intensity during the load cycle reaches the level at which crack growth is obseved to occur under static load. (Figures 5.22, 5.23).

(v) There is no significant effect of frequency on da/dN. (Figure 5.34).

(vi) Fractographs from fatigue and fast fracture surfaces are so similar they are indistinguishable. Microscopy of the fracture indicates that it is predominantly intergranular, remaining primarily in the cobalt binder; however, cleavage within the carbide grains is also frequently observed. (Sections 5.2.6, 5.4).

(vii) Crack growth rates are increased at elevated (500°C) temperatures. (Figures 5.42, 5.43, 5.46).

These results and observations suggest that both cyclic and static modes of fracture contribute to the fatigue crack growth rate. In particular, the high value of the exponent 'm' and the dependence on mean stress intensity are indicative of a dual mechanism of fatigue.

Time dependent crack growth does not appear to operate in fatigue, since da/dN is essentially independent of frequency. There is, however, evidence that when

the peak stress intensity reaches the level at which crack propagation occurs under static load, the static crack growth mechanism acts and there is a rapid increase in growth rate, (Figures 5.22, 5.23). It is predicted that da/dN would be influenced by frequency at these high peak stress intensity levels since the static crack growth is time dependent, but variable frequency tests have not been carried out in this load range.

Thus far, the only results that have been used to indicate whether fatigue crack growth is dependent on the cyclic loading, and is not simply quasi-static crack growth, are the frequency efects discussed above.

Pursuing this point, Evans, in two papers with other authors,[140,146] has described a mathematically sophisticated but extremely useful method of deriving fatigue propagation data from static crack growth results. The analysis is based on the assumption that the mechanisms of crack growth in fatigue and static loading are identical, i.e. the cyclic effects have no additional contribution to the crack advance per cycle. The crack velocity at each point during a load cycle is therefore equal to the velocity as determined by static crack growth measurements, i.e. if the crack velocity at 7,5 $MNm^{-3/2}$ is 10^{-7} m/sec under static load then during fatigue as the stress intensity passes through the value 7,5 $MNm^{-3/2}$ the velocity at that instant is also 10^{-7} m/sec. The net fatigue crack growth rate can therefore be predicted from static measurements by integration of the cyclic stress intensities.

The mathematics shows that the fatigue data, plotted with $\Delta K_I/K_{Iav}$ constant, should then have the same slope as the static growth curve. Data reduction of the results obtained from alloy G10 (Figure 5.15, K_{Iav} constant, ΔK_I varies) immediately shows that the slopes and hence mechanisms for the fatigue and static crack growth rates are different. (Figure 5.3).

This confirms the conclusion implied by the frequency

effects that fatigue crack growth is a truly cyclic mechanism in this material.

It is apparent that as the fracture toughness of the alloys increases the resistance to fatigue crack growth also increases. Thus by normalising ΔK_I, for R ratio < 0,1, with respect to the fracture toughness of the alloys, the fatigue crack propagation rates fall within a reasonably narrow range, (Figure 6.4). The results are in fair agreement with Viswanadham's data.[114] In addition, as the toughness (and mean free path, Figure 5.10) increases the value of the exponent 'm', for R ratio < 0,1, decreases. (Figure 6.5).

It may therefore be possible to approximate fatigue crack growth data in WC-Co hardmetal alloys simply by determining the fracture toughness, an 'm' value can then be obtained from Figure 6.5 and crack growth rate from Figure 6.4.

effects that fatigue crack growth is a truly cyclic mechanism in this material.

It is apparent that as the fracture toughness of the alloys increases the resistance to fatigue crack growth also increases. Thus by normalising ΔK_I, for R ratio = 0,1, with respect to the fracture toughness of the alloys, the fatigue crack propagation rates fall within a reasonably narrow range, (Figure 6.4). The results are in fair agreement with Viswanadham's data.[114] In addition, as the toughness (and mean free path, Figure 6.10) increases the value of the exponent 'm', for R ratio = 0,1, decreases. (Figure 6.5).

It may therefore be possible to approximate fatigue crack growth data in WC-Co hardmetal alloys simply by determining the fracture toughness, an 'm' value can then be obtained from Figure 6.5 and crack growth rate from Figure 6.4.

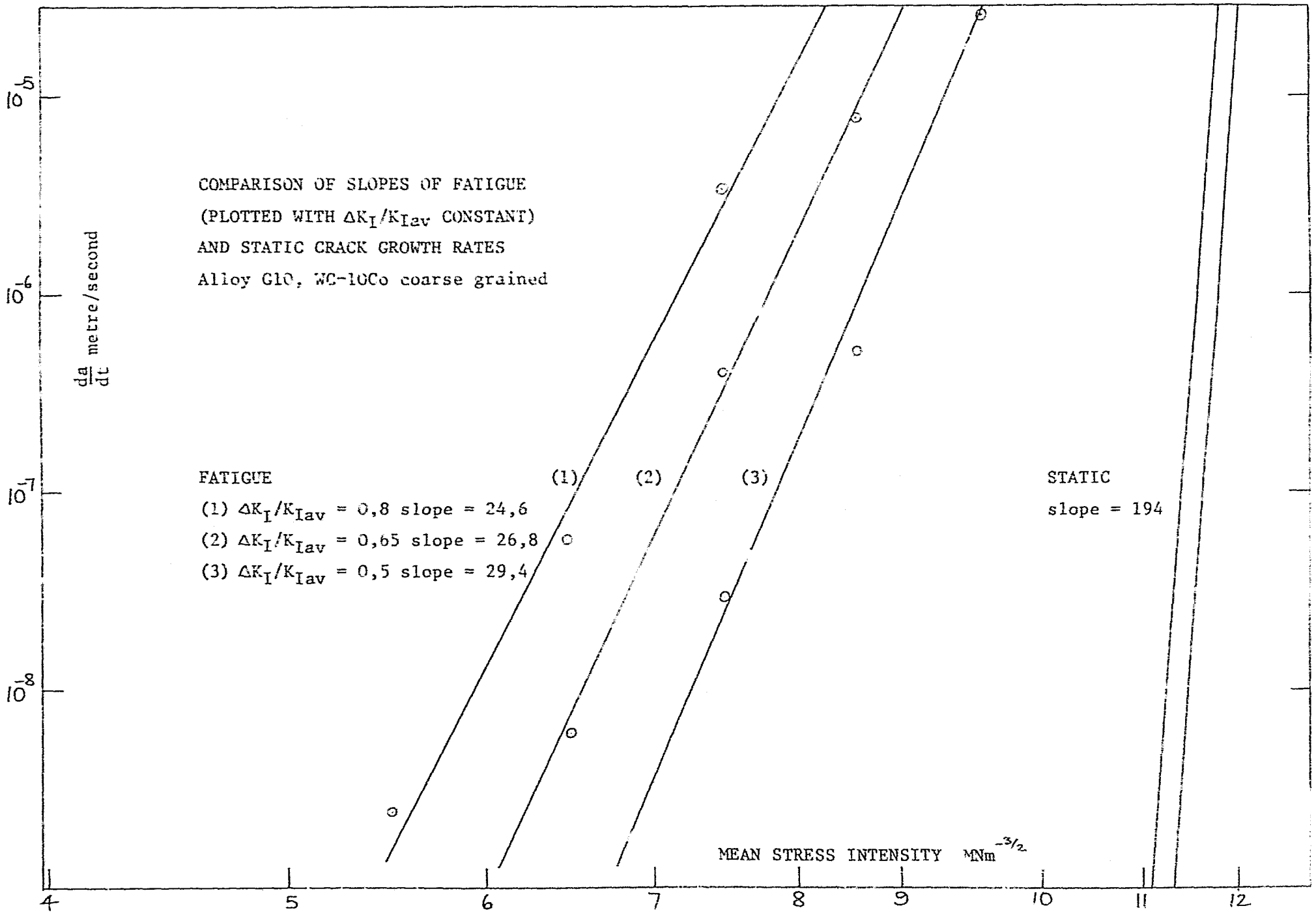
COMPARISON OF SLOPES OF FATIGUE
(PLOTTED WITH $\Delta K_I/K_{Iav}$ CONSTANT)
AND STATIC CRACK GROWTH RATES
Alloy G10, WC-10Co coarse grained
10^{-6}
10^{-7}
10^{-8}
$\frac{da}{dt}$ metre/second
FATIGUE
(1) $\Delta K_I/K_{Iav}$ = 0,8 slope = 24,6
(2) $\Delta K_I/K_{Iav}$ = 0,65 slope = 26,8
(3) $\Delta K_I/K_{Iav}$ = 0,5 slope = 29,4
(1)
(2)
(3)
STATIC
slope = 194
MEAN STRESS INTENSITY $MNm^{-3/2}$
4
5
6
7
8
9
10
11
12

Figure 6.3

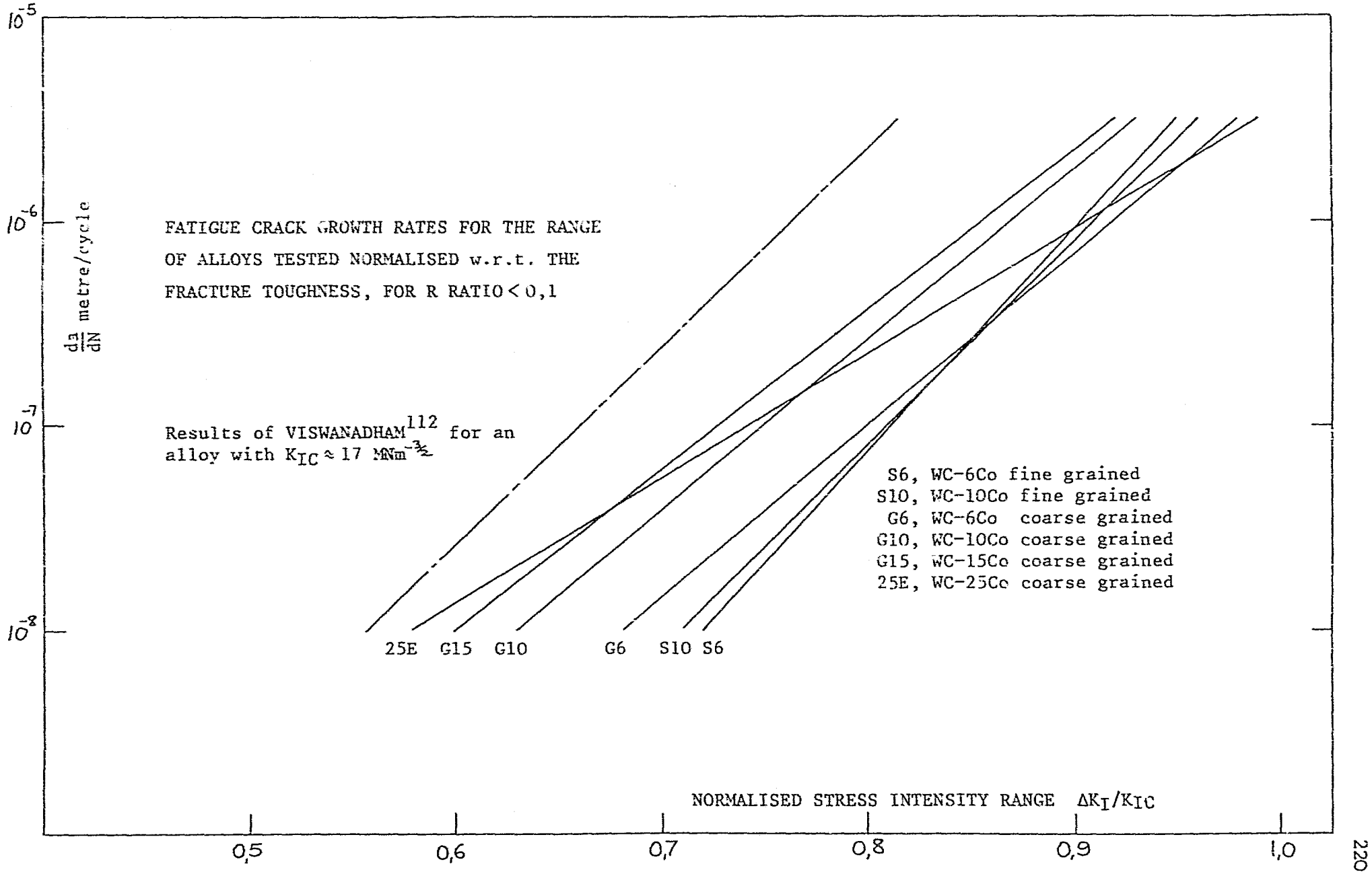
FATIGUE CRACK GROWTH RATES FOR THE RANGE OF ALLOYS TESTED NORMALISED w.r.t. THE FRACTURE TOUGHNESS, FOR R RATIO < 0,1
Results of VISWANADHAM[112] for an alloy with $K_{IC} \approx 17$ MNm$^{-3/2}$
S6, WC-6Co fine grained
S10, WC-10Co fine grained
G6, WC-6Co coarse grained
G10, WC-10Co coarse grained
G15, WC-15Co coarse grained
25E, WC-25Co coarse grained
25E G15 G10 G6 S10 S6
10^{-5}
10^{-6}
10^{-7}
10^{-8}
$\frac{da}{dN}$ metre/cycle
NORMALISED STRESS INTENSITY RANGE $\Delta K_I/K_{IC}$
0,5 0,6 0,7 0,8 0,9 1,0
220

Figure 6.4

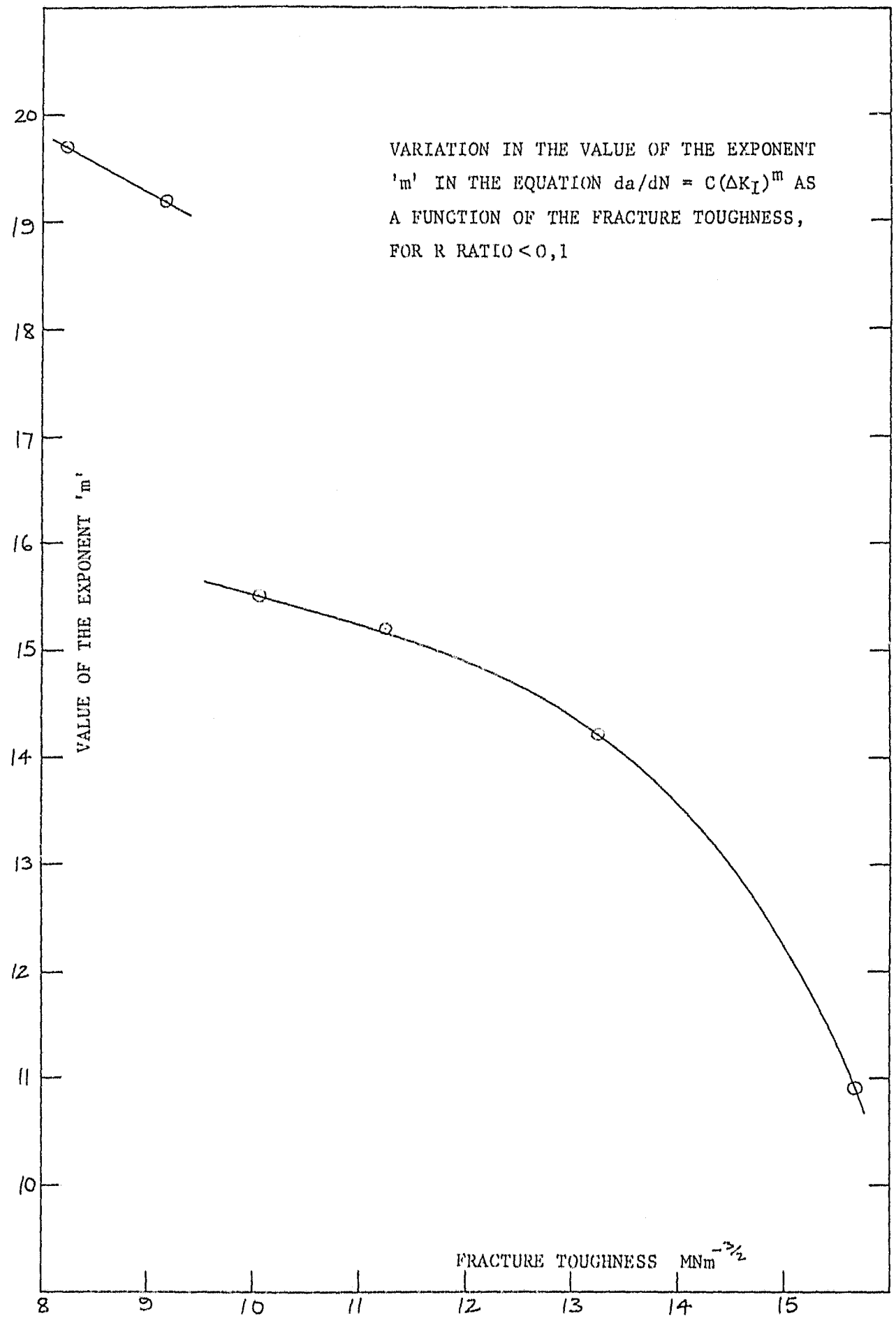
VARIATION IN THE VALUE OF THE EXPONENT 'm' IN THE EQUATION da/dN = C(ΔK_I)^m AS A FUNCTION OF THE FRACTURE TOUGHNESS, FOR R RATIO < 0,1
VALUE OF THE EXPONENT 'm'
20
19
18
17
16
15
14
13
12
11
10
FRACTURE TOUGHNESS MNm^-3/2
8
9
10
11
12
13
14
15

Figure 6.5

6.4 FRACTURE TOUGHNESS

The fracture toughness values are all below those determined by other investigators with respect to both hardness, an easily measured mechanical property, and mean free path, a rather inexact microstructural parameter, (Figures 6.6 - 6.8). There is no obvious explanation for this but the primary reason appears to be associated with the excess carbon, in the material tested, which is reported to be extremely detrimental to mechanical strength.[30,92-94] (Section 2.7.4, Figure 2.8(e)).

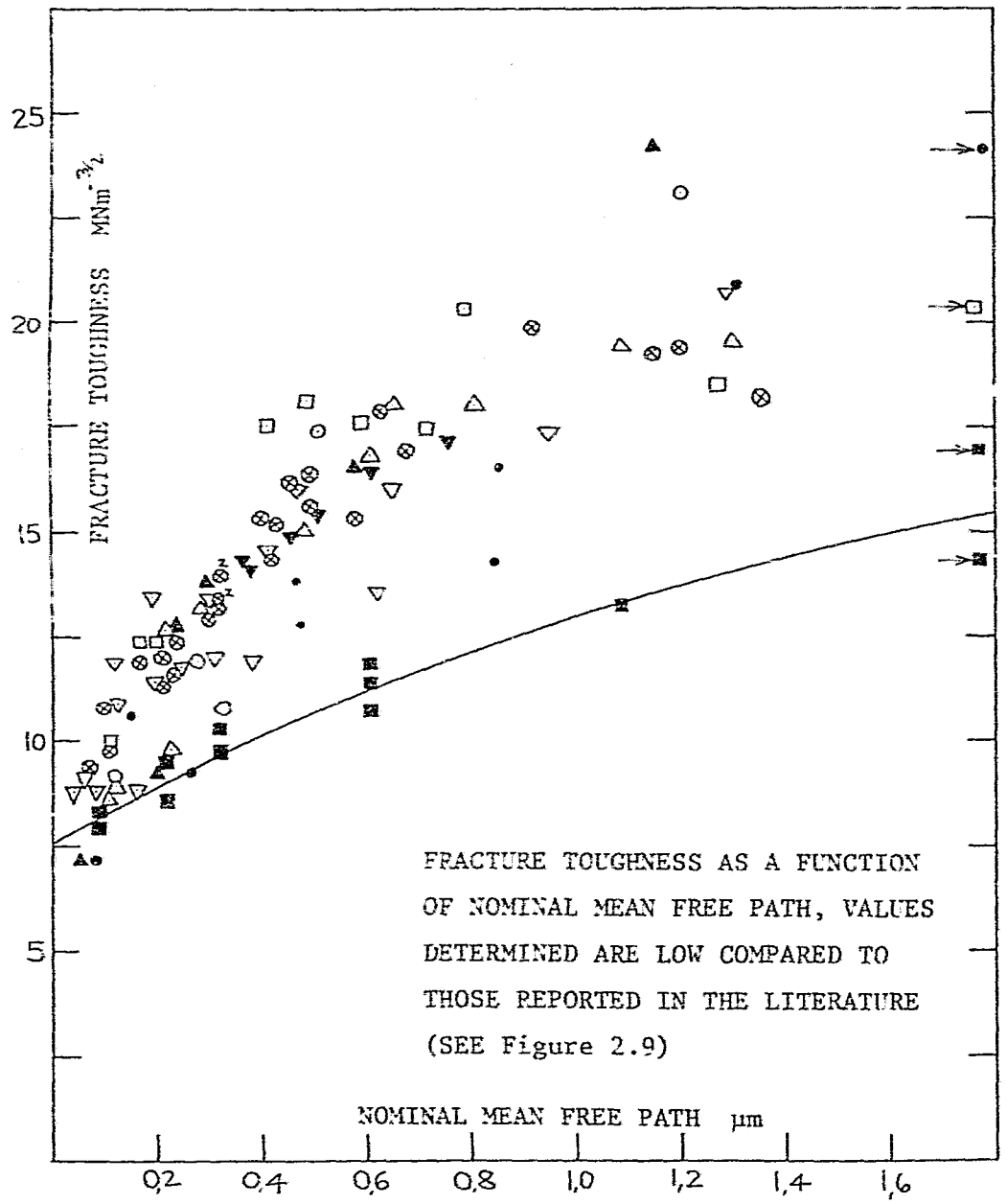

Figure 6.6

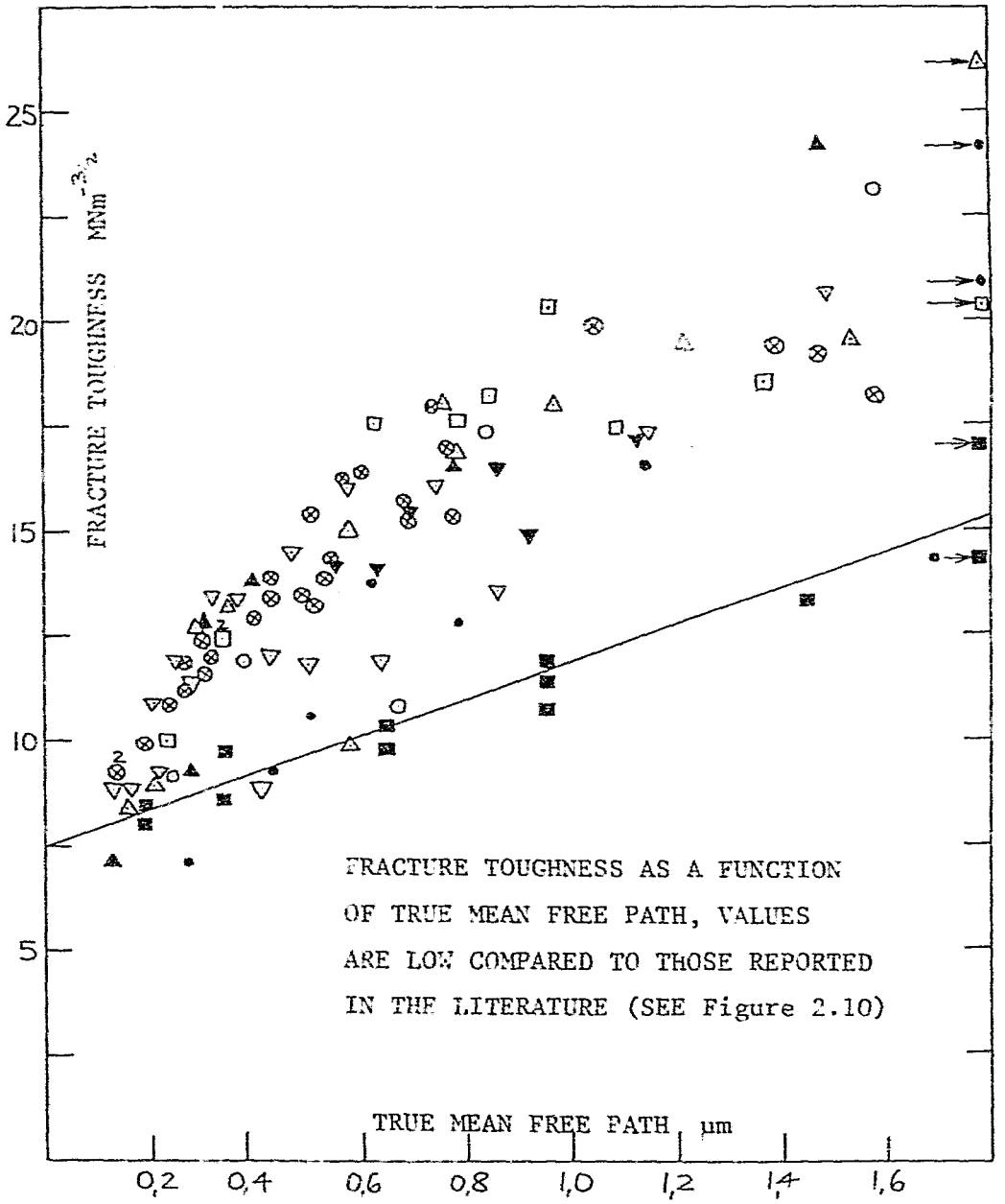

Figure 6.7

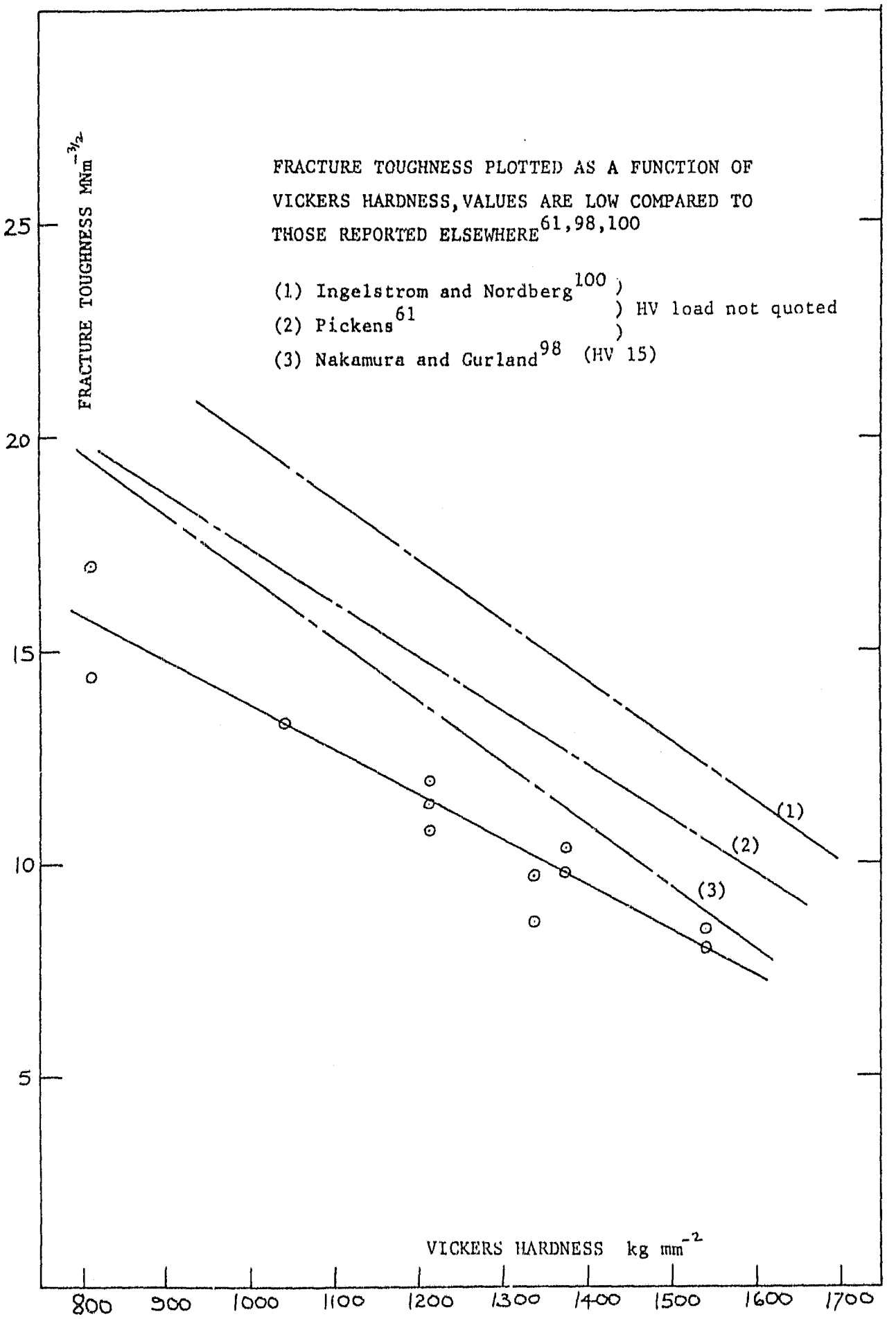
FRACTURE TOUGHNESS PLOTTED AS A FUNCTION OF VICKERS HARDNESS, VALUES ARE LOW COMPARED TO THOSE REPORTED ELSEWHERE[61,98,100]
(1) Ingelstrom and Nordberg[100]) HV load not quoted
(2) Pickens[61])
(3) Nakamura and Gurland[98] (HV 15)
FRACTURE TOUGHNESS MNm$^{-3/2}$
25
20
15
10
5
(1)
(2)
(3)
VICKERS HARDNESS kg mm^{-2}
800
900
1000
1100
1200
1300
1400
1500
1600
1700

Figure 6.8

6.5 MODEL OF THE CRACK TIP

A model system, similar to that proposed by Evans,[115] is envisaged as being the most appropriate, i.e. a brittle low toughness carbide phase in a high ductility high toughness binder.

The carbide grains impose a triaxial constraint on the binder. The degree of constraint and hence the local mechanical behaviour depends on the binder layer thickness. In places where the constraint is high the binder has high strength and low ductility. As the constraint decreases (binder layer thickness increases) the yield strength decreases and strain to failure increases, (Figure 6.9). Hence at the crack tip, as the load is applied and crack displacement increases, the highly constrained binder will fail by ductile rupture and microvoid coalescence (a static fracture mode) while the less constrained will elongate and form ligaments spanning the crack. In addition, the local orientation of the binder film with respect to the crack plane will influence its behaviour. Plastic flow and elongation of a binder layer perpendicular to the crack is easier than for one in the plane of the crack. (Figure 6.10).

The tungsten carbide grains in the region of the crack tip behave as microstructural fracture toughness specimens and if the prevailing stress intensity in the immediate vicinity of a grain exceeds the fracture toughness of tungsten carbide, fracture of the grain occurs.

At any position, therefore, the crack front is likely to be ill-defined, with intact cobalt ligaments spanning the crack behind regions of decohesion by ductile rupture and fractured carbide particles. (Figure 6.10).

Under a monotonic load the binder ligaments spanning the crack provide a restraint to the crack opening, opposing the applied stress intensity at the crack tip. As long as the strain to rupture of these ligaments is

greater than the local crack displacement, they will inhibit crack advance. The failure of these binder ligaments is controlled by the strain a particular ligament can tolerate and this in turn is a function primarily of the degree of constraint imposed, i.e. the binder layer thickness.

As the binder layer thickness increases local constraint is reduced, the ductility increases and the binder spans the crack more easily. The average binder thickness of an alloy, defined by the mean free path, therefore controls the inherent toughness of the composite. (Figures 2.9, 2.10).

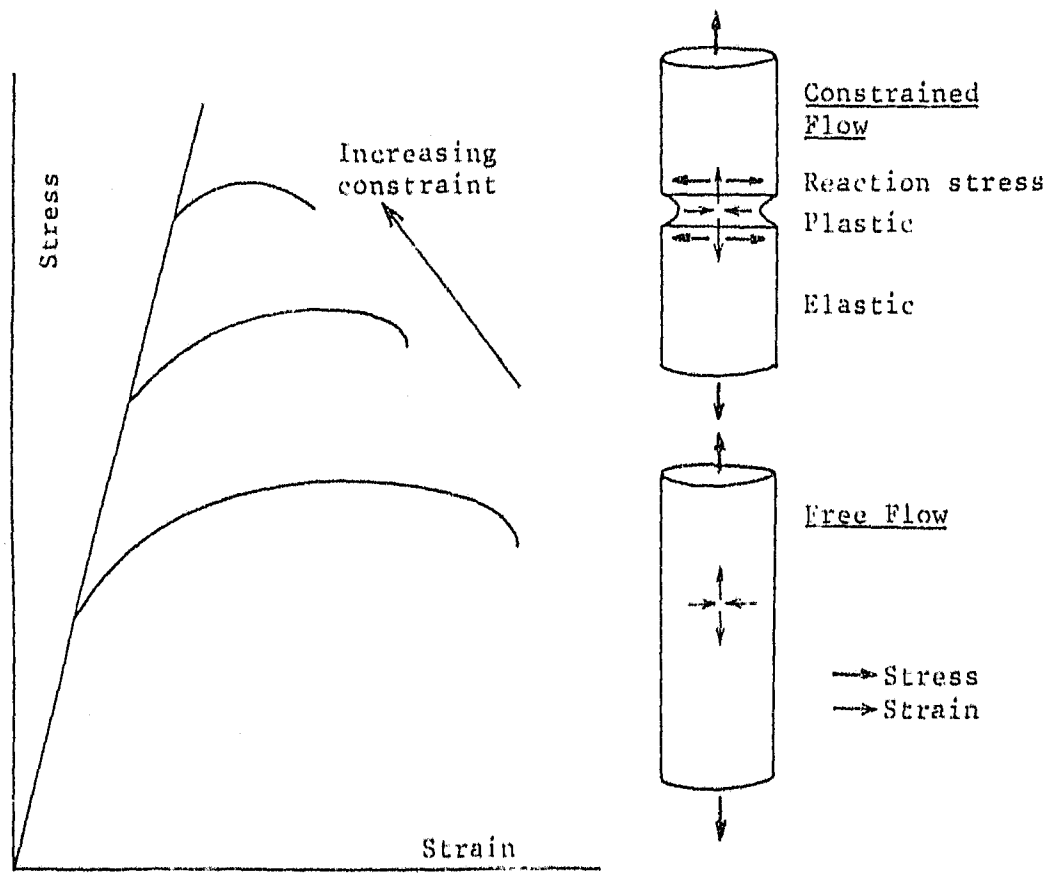

Figure 6.9 Effect of constraint on the mechanical behaviour of a thin film.

Schematic view of crack front perpendicular to the plane of the crack

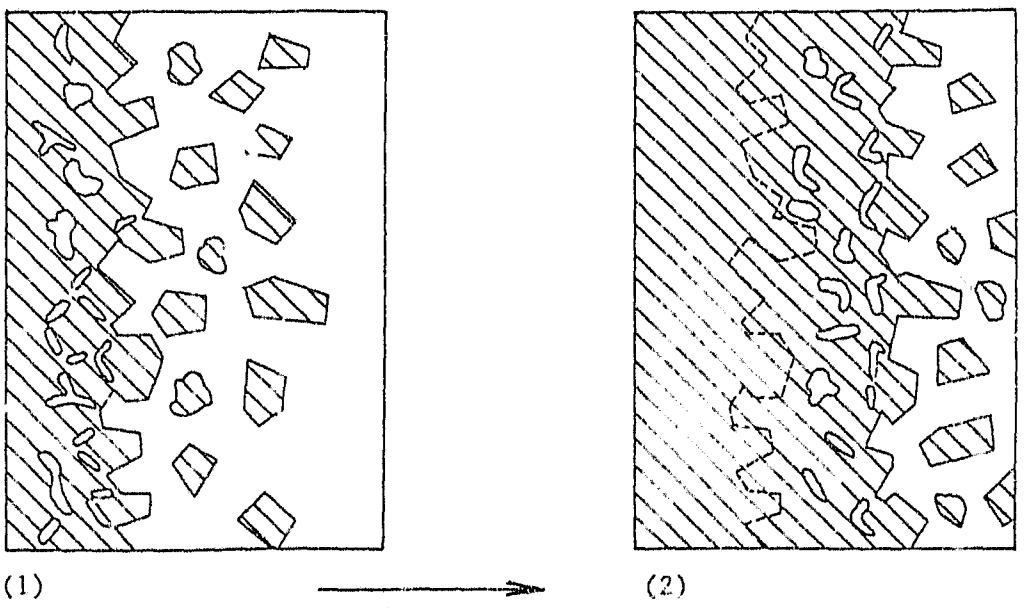

Schematic view of crack front in the plane of the crack

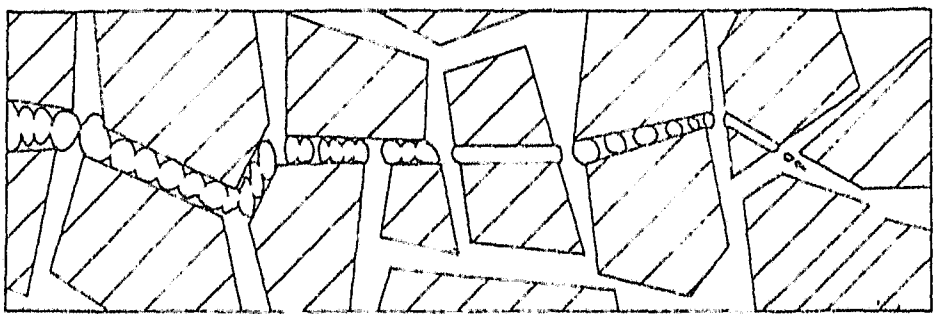

Figure 6.10 Schematic representation of the crack front in WC-Co alloys.

6.6 MODEL FOR STATIC CRACK GROWTH

At stress intensities below the static crack growth regime for the composite, but above the fracture toughness of the tungsten carbide grains, the binder provides sufficient restraint to crack opening to prevent fracture. As the stress intensity increases the displacements at the crack tip increase until the point is reached where ligaments tear apart by strain controlled local necking, and normally fast fracture would occur. The stress intensity is either below the value at which the binder fails or is at the critical value, K_{IC}.

However, since subcritical crack growth is observed to occur it is necessary to invoke some time dependent mechanism for failure of the highly strained ligaments, at stress intensities close to the fracture toughness. There are only two possible mechanisms: creep, which is very unlikely at room temperature, and environmental effects due to the laboratory air and/or dye penetrant.

As discussed in Section 6.2 there is no confirmatory evidence to indicate whether or not the mechanism is environmental. Tests in vacuum or an inert atmosphere, using a crack growth monitoring technique other than dye penetrant, are needed to determine the extent of the environmental influence.

6.7 MODEL FOR FATIGUE CRACK GROWTH

In discussing fatigue the ill-defined crack front previously described is assumed, (Figure 6.10). Consider, for example, a set of 4 idealised intact binder ligaments at the crack tip, subjected to alternating stress.

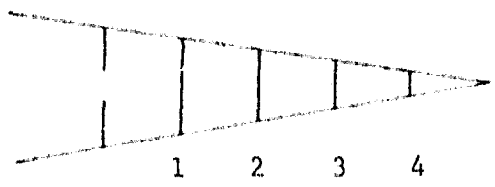

The crack surface separation, at a given distance behind the crack tip, is the same for each, identical load cycle. The ligaments, particularly those furthest from the crack tip are subject to extensive plastic strain. (The residual stresses in the binder due to the different thermal expansion coefficients have been theoretically estimated to be above yield, Section 2.6). Assume a typical stress-strain curve for the cobalt rich binder; each ligament is at a particular point on the curve. (Figure 6.11).

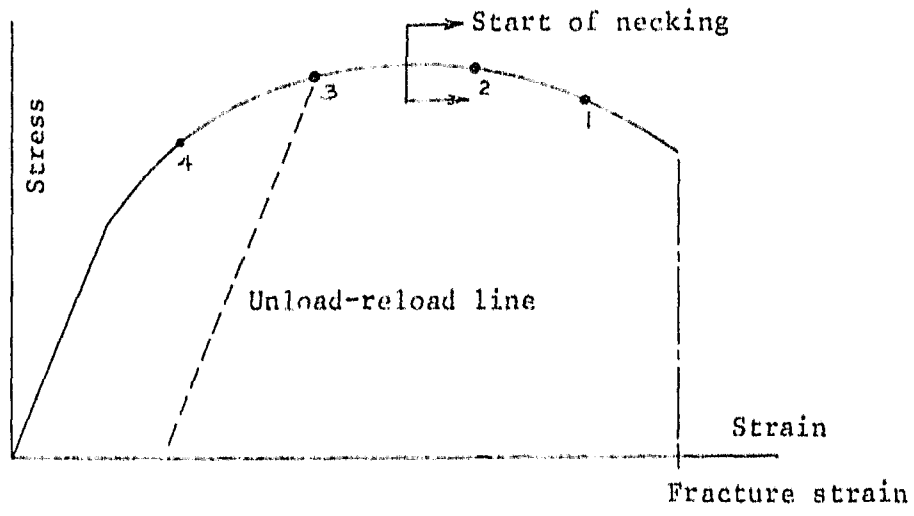

Figure 6.11

If the crack did not advance in successive cycles each ligament would elastically unload and reload to its identical point on the curve, same strain, ad infinitum. However, since the results obtained show that fatigue does occur and the crack advances in successive cycles a mechanism of cyclic damage must operate, altering the state of the crack tip by the load-unload-reload event.

Almond and Roebuck[111] have proposed a work hardening mechanism in which the binder ligaments become increasingly less ductile with each fatigue cycle. However the degree of work hardening is a strain controlled process, and it can only increase if the strain on the ligaments increases, i.e. if the crack advances. The mechanism does not offer an adequate explanation of how the crack could advance. The status quo of individual ligaments elastically unloading and reloading (Figure 6.11) is a closed-loop situation in which work hardening, per se, cannot cause crack growth.

It is possible that stress cycling could cause the metastable f.c.c. structure (12 slip systems) to undergo a stress induced transformation to the room temperature stable h.c.p. structure (3 slip systems). Since very little is known about the parameters that control this transformation no precise mechanism can be proposed. However, if the percentage of binder transformed increases with the number of cycles as reported by Miyake et al.[104] then it is possible that the ligaments become increasingly less able to extend to the imposed strain at the crack tip and after a certain number of cycles fracture. The crack can then advance and the next ligament which has been subjected to the same fatigue cycling now experiences greater strain causing failure in the subsequent cycles.

Alternatively, if each ligament is considered as an individual microstructural tensile specimen, conventional low cycle fatigue mechanisms can conceivably lead to failure.

Evans[118] has proposed an extremely acceptable mechanism for cyclic crack advance in WC-Co alloys due to plastic buckling and consequent failure of the binder ligaments during the unloading half cycle. As the number of effective ligaments providing restraint is reduced, on the loading half cycle the crack advances by static modes such as cleavage of the carbide and microvoid coalescence in the binder. On reloading new ligaments are formed at the crack tip and the ligaments remote from the tip elongate; some remain intact and others, particularly those that have severely buckled during previous unloading cycles, fail by ductile tearing.

The extent of crack advance by static modes is dependent on the maximum stress intensity, K_{Imax}, while the buckling damage to the ligaments depends on the crack closure, i.e. the minimum stress intensity, K_{Imin}.

The effects of K_{Imax} and K_{Imin}, reflected by the influence of both ΔK_I and K_{Iav} on da/dN, are adequately explained by this model.

The constant mean stress intensity tests, show a lower limit of approximately 10 for the exponent 'm' in the Paris relationship, although C values increase as K_{Iav} (and K_{Imax}) increases. Thus the mechanisms, which govern the value of 'm', remain the same as K_{Iav} increases but the actual growth rate at a given ΔK_I increases as K_{Iav} (and K_{Imax}) increases. This means that binder ligament failure is the controlling fatigue mechanism and is totally a function of ΔK_I but the incremental crack advance is dependent also on the static fracture modes which are predominantly a function of K_{Imax}. None of these mechanisms is time dependent.

The increase in 'm' as K_{Imax} approaches stress intensities at which static growth occurs is hardly surprising. The quasi-static growth already discussed obviously contributes significantly to the crack advance per cycle.

The decrease in 'm' as the mean free path increases means that the incremental crack advance per cycle is reduced. The binder ligaments are thicker and therefore less constrained and more ductile; less will fail by buckling on the unloading half cycle. On reloading, therefore, there is a reduced length of crack advance by static modes before the restraint imposed by the ligaments is restored.

The increased crack growth rate at elevated temperature is also explained by this model. The strength of the binder is reduced such that buckling and necking failure occur at lower local stresses, while the basic mechanism remains unchanged.

It is, of course, quite possible that more than one mechanism contributes to the fatigue crack growth. Failure of ligaments could be due to the combined effects of buckling and subsequent necking, work hardening, the f.c.c. to h.c.p. transformation and conventional low cycle fatigue.

6.8 ANVIL FAILURE

There are insufficient data available for an in depth fracture mechanics analysis of anvil failures. However, it is interesting to calculate the approximate fatigue life using the data for alloy S10, which illustrate the effect of different stresses, initial flaw size and temperature.

Blumenthal[1] has determined a maximum tensile stress in anvils, approximately halfway down the nose cone, of 700 MPa (101200 psi) for a synthesis pressure of 6300 MPa (63 kbar).

Fatigue crack propagation normally initiates at some internal or surface defect. Flaws are usually present to some extent in the microstructure of WC-Co alloys in the form of non-metallic inclusions and porosity.[71-74] The diameter of these flaws is typically in the range 20 - 100 μm,[71,72,74] although larger pores do occur.[74]

Fatigue life (or number of cycles to failure, N_f) is determined by integrating the equation $da/dN = C(\Delta K_I)^m$ as outlined in Section 1.1 to obtain:

$$N_f = \frac{1}{C\phi^m \pi^{m/2} (\Delta\sigma_{app})^{m(1-m/2)}} \left[a_c^{(1-m/2)} - a_i^{(1-m/2)} \right]$$

where:

N_f = number of cycles to failure
C = constant
ϕ = geometric constant
m = crack growth rate exponent
$\Delta\sigma_{app}$ = applied stress range
a_c = critical flaw size
a_i = initial flaw size

The critical flaw size is calculated using the equation $K_{IC} = \phi \sigma_{app}(\pi a)^{\frac{1}{2}}$ where the geometric constant o has the following values:

(i) surface flaw, ϕ = 1,12

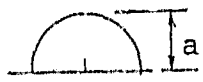

(ii) internal defect, ϕ = 1,0

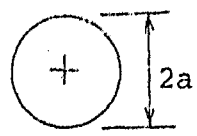

For simplification, a value of 1,0 has been assumed for all the calculations.

The constants 'm' and C and the fracture toughness are obtained from the crack growth rate results, (Figure 5.42). The fracture toughness of 7,62 $MNm^{-3/2}$ for S10 at 500°C has not been experimentally determined but is inferred from the crack growth data.

	Room temperature (RT)	500°C
m	19,2	19,2
C	8,20 x 10^{-25}	5,69 x 10^{-22}
K_{IC}	9,17 $MNm^{-3/2}$	7,62 $MNm^{-3/2}$

The critical crack length, a_c, is calculated using the fracture toughness and the applied stress. A value for the maximum tensile stress of 700 MPa is reported by Blumenthal[1] but calculations using a 20% greater stress i.e. 840 MPa, are included to show how stress level affects the life.

	Critical crack length, a_c	
	RT	500°C
700 MPa	54,6 µm	37,7 µm
840 MPa	37,9 µm	26,2 µm

Hence the fatigue life is calculated as follows:

At room temperature:

$$N_f = \frac{1}{8,20\times10^{-25}(1)^{19,2}\pi^{9,6}(1-9,6)\Delta\sigma_{app}^{19,2}}\left[a_c^{-8,6}-a_i^{-8,6}\right]$$

At 500°C:

$$N_f = \frac{1}{5,69\times10^{-22}(1)^{19,2}\pi^{9,6}(1-9,6)\Delta\sigma_{app}^{19,2}}\left[a_c^{-8,6}-a_i^{-8,6}\right]$$

A range of typical pore sizes (diameter 20 - 100 μm) has been used for the initial crack length, (a_i = 10 - 50 μm).

The influence of stress level, flaw size and temperature on expected life is clearly illustrated in Table 6.1. It is immediately obvious that the initial defect size, a_i, is of primary importance in the life expectancy of a compon nt. An internal pore with a diameter of 40 μm (a_i = 20 μm) gives an expected life of 14600 cycles at room temperature and 700 MPa stress, but doubling the initial defect size (a_i = 40 μm) reduces the life to only 35 cycles. Increasing the operating temperature and stress also causes a considerable reduction in the life.

Although these calculations may partly explain the variable life obtained from anvils, (Table 1.2), the existence of cracks considerably larger than the critical defect size is not well understood, (Figures 1.1, 1.2). The only feasible explanation for this anomaly is that the predominantly compressive stress field, and the steel rings used to constrain the anvil, prevent catastrophic failure. Hence, cracks can grow to sizes substantially greater than those calculated in the fracture mechanics approach. A more detailed analysis of the stress condition in anvils and fracture mechanics data for the

actual grades used may provide a still better theoretical explanation for the observed operational life of these components.

Table 6.1

EFFECT OF STRESS, FLAW SIZE AND TEMPERATURE ON LIFE

a_i (μm)	Number of cycles to failure			
	RT		500°C	
	700 MPa	840 MPa	700 MPa	840 MPa
10	$5{,}66 \times 10^6$	$1{,}71 \times 10^5$	8163	246
15	$1{,}73 \times 10^5$	5228	249	7
20	$1{,}46 \times 10^4$	438	21	
25	2140	63	3	
30	444	12		
35	116	2		
40	35			
45	11			
50	3			

7 CONCLUSIONS AND RECOMMENDATIONS FOR FUTURE WORK

7.1 CONCLUSIONS

7.1.1 Experimental Technique

The double torsion test has proved to be eminently suitable for both static and fatigue crack growth rate measurements in tungsten carbide-cobalt alloys, particularly as a method has been developed whereby the direction of crack propagation can be controlled. The use of a reliable procedure to obtain centre line fracture in specimens without grooves means that the unknown effect of these grooves on the stress intensity calculation is eliminated.

Crack monitoring using dye penetrant and a travelling microscope has permitted extremely sensitive crack length measurement, to a precision of 0,01 mm. The absence of frequency effects on da/dN suggests that the dye penetrant does not influence the crack growth rate. It is therefore an accurate and valid measurement technique.

7.1.2 Static Crack Growth

Static crack growth under monotonic loading in the laboratory air environment occurs only at stress intensities close to the fracture toughness, $K_I > 0,9K_{IC}$. An alloy's resistance to static crack growth is therefore totally predictable from the fracture toughness. As the mean free path of the cobalt binder increases the toughness and stress intensity required for static crack growth increase. These results are consistent with those reported by Osterstock.[103]

Crack propagation and arrest have been observed in high vacuum in a scanning electron microscope. This does not however prove that static stable crack growth can occur in vacuum since the test procedure used causes the stress intensity to decrease as the crack (which may only initiate at K_{IC}) propagates.

7.1.3 Fatigue Crack Growth

Fatigue crack growth rates increase as the stress intensity range increases and can be described by a power law of the form $da/dN = C(\Delta K_I)^m$, as reported in other investigations.[109-112]

In the range of alloys tested, as the mean free path of the binder increases (cobalt content and grain size increase) the crack growth rate and the value of the exponent 'm' decrease, in agreement with Lueth's results.[110]

Fatigue crack growth rates are dependent on the mean stress intensity level, increasing as K_{Iav} increases, as reported by Evans and Linzer.[109] However, provided the maximum stress intensity reached is below th[illegible]vels at which cracking occurs under static load, the[illegible]nt 'm' has a constant value. In the case of al[illegible] (WC-10 wt% Co, coarse grained) this value is approximately 10. Therefore as K_{Iav} increases, the mechanisms (which control the value of 'm') remain the same and the increased growth rate observed is due to additional crack advance by static modes resulting from the increase in K_{Imax}. This shows that the cyclic crack propagation is a function of the absolute values of the maximum and minimum stress intensity in the load cycle.

The fatigue crack growth rate increases dramatically when the maximum stress intensity reached during the load cycle is above the level at which cracking occurs under static load.

7.1.4 Fractography

Fractographs of fatigue and fast fracture are indistinguishable. Ductile dimples and ligament formation in the cobalt-rich binder and occasional transgranular fracture of the tungsten carbide grains are features characteristic of both fatigue and catastrophic crack propagation.

7.1.5 Model for Fatigue Crack Propagation

Fatigue crack propagation occurs by true cyclic mechanisms but static modes of fracture contribute to the crack extension per cycle and this results in the relatively high 'm' values obtained. A model is proposed in which binder ligaments spanning the fracture surfaces behind the crack tip fail by plastic buckling damage during the unloading half cycle. The effects of work hardening, the f.c.c. to h.c.p. transformation and conventional low cycle fatigue, or a combination of these, may also lead to crack growth in the binder. On the loading half cycle the crack advances by static modes, such as cleavage of the carbide grains and microvoid coalescence in the binder, until the restraint to crack opening and advance, imposed by the intact and newly formed binder ligaments, is restored.

7.2 RECOMMENDATIONS FOR FUTURE WORK

There are several aspects of this investigation that require further work for complete clarification and, if the research programme is to continue, particular areas which should be developed.

7.2.1 Double Torsion Test Geometry

The use of double torsion test specimens without grooves, and the ability to ensure centre line fracture, has eliminated most of the uncertainties of this test technique that remain unresolved. (Section 3.5, Table 3.3).

The method has outstanding potential as a standard test for brittle materials. However, a three dimensional finite element analysis is probably required, to provide a sound theoretical basis for many of the aspects which are at present only experimentally justified. In particular the effects of the following need to be determined analytically:

(i) specimen dimensions on the region of constant stress intensity
(ii) alignment on the direction of crack propagation
(iii) grooves on the stress intensity calculation.

7.2.2 Crack Length Measurement

The procedures used to measure crack length and hence crack growth rate are laborious and time consuming but are extremely effective and accurate. The only contentious aspect is the possible environmental effect of the dye penetrant.

Indirect measurement of crack length is a desirable and in an inert environment or at elevated temperatures an almost essential method of monitoring fatigue crack

growth. The electrical potential drop system has been used by Almond and Roebuck[111] on WC-11Co bend specimens and compliance has been used successfully in other ceramic materials.[127,143,144]

Compliance measurements attempted in this investigation were not very successful primarily due to the fact that small changes in crack length could not be detected, (Section 4.5). It is possible that by using LVDT's with higher sensitivity this technique could provide an indirect crack monitoring system.

7.2.3 Inert Atmosphere and Elevated Temperature Tests

There is no evidence so far to prove whether or not static crack growth in WC-Co alloys is an environmentally controlled mechanism. This can only be resolved by testing specimens in an inert or vacuum environment using remote crack length measurement, (Section 7.2.2), under load control. Load relaxation tests, in displacement control are unlikely to be successful due to the fact that the crack arrests after only a small decrease in load. (Section 4.5.3).

The elevated temperature tests need considerable refinement so that the whole specimen is at temperature and in an inert atmosphere. Once again remote or indirect crack growth monitoring is required.

7.2.4 Fracture Toughness

The fracture toughness values obtained were rather lower than expected with respect to both the mean free path and the hardness. Although the probable cause for this is the excess free carbon in the material supplied it would be useful to confirm the values by manufacturing three-point bend, K_{IC}, test specimens from the fractured double torsion specimens.

growth. The electrical potential drop system has been used by Almond and Roebuck[111] on WC-11Co bend specimens and compliance has been used successfully in other ceramic materials.[127,143,144]

Compliance measurements attempted in this investigation were not very successful primarily due to the fact that small changes in crack length could not be detected, (Section 4.5). It is possible that by using LVDT's with higher sensitivity this technique could provide an indirect crack monitoring system.

Inert Atmosphere and Elevated Temperature Tests

There is no evidence so far to prove whether or not static crack growth in WC-Co alloys is an environmentally controlled mechanism. This can only be resolved by testing specimens in an inert or vacuum environment using remote crack length measurement, (Section 7.2.2), under load control. Load relaxation tests, in displacement control are unlikely to be successful due to the fact that the crack arrests after only a small decrease in load. (Section 4.5.3).

The elevated temperature tests need considerable refinement so that the whole specimen is at temperature and in an inert atmosphere. Once again remote or indirect crack growth monitoring is required.

7.2.4 Fracture Toughness

The fracture toughness values obtained were rather lower than expected with respect to both the mean free path and the hardness. Although the probable cause for this is the excess free carbon in the material supplied it would be useful to confirm the values by manufacturing three-point bend, K_{IC}, test specimens from the fractured double torsion specimens.

7.2.5 In Situ SEM Studies of Fracture

The fine grained 6 wt% cobalt alloy used for the small scale double torsion fracture studies in the scanning electron microscope showed that the technique has considerable potential. However, if it is to be used to investigate models for fracture, for example to confirm whether or not binder ligaments exist behind the crack tip, a higher cobalt, larger grain size alloy should be used. The increased size of the microstructural features (mean free path and grain size) should enable fracture processes to be identified more easily at the available magnification and resolution.

7.2.6 Fractography

The 'matching pairs' fractographic technique used by Luyckx[116] is laborious but is extremely effective for assessing the extent of transgranular and intergranular fracture. A 'landmark' must be located on the opposing fractures before matching areas can be photographed. A landmark consists of an exceptionally large grain, area of porosity or similar defect. Since these are not abundant, considerable effort has to be made going from one surface to the other searching for a suitably dominant feature. The method however could be ideal for quantifying and comparing the percentage of intergranular and transgranular fracture in different alloys on both fatigue and catastrophic crack propagation surfaces.

7.2.7 General

There is a considerable matrix of fatigue and material parameters that could be investigated in future work.

(i) Loading wave form: a comparison of the fatigue crack growth rates obtained from triangular and square wave cycling would confirm that, provided K_{Imax} is below the time dependent static crack growth stress intensity level, da/dN is dependent only on cyclic mechanisms and the values of K_{Imax} and K_{Imin}; and show that if K_{Imax} is above this level only then do time dependent mechanisms contribute to growth.

(ii) Elevated temperatures: many components operate at temperatures above ambient. Further tests are required to characterise the influence of temperature on fatigue crack growth rate for a range of alloys.

(iii) Fatigue threshold: fatigue crack growth rates below 10^{-9} m/cycle require long term testing and have not been determined in this investigation. It would be useful however to determine whether a fatigue threshold exists. If it does the stress intensity range or stress level for infinite life could be predicted.

(iv) Alloying of the binder and the use of other hardmetal systems: there are numerous hardmetal alloy combinations in addition to the most common WC-Co system. It would be useful to investigate whether any benefit to fatigue resistance can be derived from alloy additions to the cobalt binder, the use of TaC and TiC grains or even completely different binders, such as nickel.

(v) The synergistic interaction of all these variables.

REFERENCES

1 Blumenthal G.D. The Stress Analysis of Pressure Magnification Anvils for Diamond Synthesis. M.Sc. Thesis. University of the Witwatersrand, 1968.

2 Luyckx S.L. Boart Basic Research Group Report, University of the Witwatersrand, March 1980.

3 Exner H.E. International Metals Reviews: Review 243, No 4, 1979. 149-173

4 Sarin V.K. and Johannesson T. Metal Science 9, 1975. 472-476.

5 Pickens J.R. and Gurland J. Mater. Sci. Eng. 33, 1978. 135-142

6 Doi H., Fujiwara Y. and Oosawa Y. Proceedings of the 1971 International Conference on Mechanical Behaviour of Materials Vol V. 207-219. (The Soc. of Mat. Sci., Japan, 1972.)

7 Luyckx S.L. Ph.D Thesis, University of the Witwatersrand, 1967.

8 Lardner E. and McGregor N. J. Inst. Metals 80: 1951-52. 369.

9 Kieffer R. and Benesovsky F. Hartstoffe 1963, Wien, New York, Springer-Verlag.

10 Arndt R. Z. Metallkd. 63, 1972. 274.

11 Pfau H. and Rix W. Z. Metallkd. 43, 1952. 440.

12 French D.N. and Thomas D.A. Int. J. Powder Metall 3(3), 1967. 7.

13 Kreimer G.S. and Alekseeva N.A. Sov. Phy. Met. Metallogr. 13, 1961. 114.

14 French D.N. and Thomas D.A. Anisotropy in Single Crystal Refractory Compounds. (eds. F.V. Vahldiek and J. Mersol) Vol 1, 55, 1968. New York, Plenum Press.

15 Takahashi T. and Freise E.J. Philos Mag 12(115), 1965. 1.

16 Hagege S., Vicens J., Nouet G. and Delavignette P. Phys. Stat. Sol. (a) 61, 1980. 675.

17 Cobalt Monograph, edited by Centre d'Information du Cobalt, Brussels, 1960.

18 Kreimer G. S. Strength of Hard Alloys, from Russian, Consultants Bureau N.Y., 1968.

19 Rüdiger O. and Exner H.E. Powder Metallurgy-Promises and Problems. 122, 1975. Paris, Matériaux et Techniques.

20 Rüdiger O. and Exner H.E. Powder Metall. Int. 8, 1976. 7.

21 Jonsson H. and Aronsson B. J. Inst. Met. 97, 1969. 281.

22 Wilbrand J. and Wieland U. Int. Powder Metall. 8, 1972. 89.

23 Sandford E.Y. and Trent E.M. Symposium on Powder Metallurgy. Iron and Steel Inst. Special Report Vol 38, 1947. 84.

24 Hess J.B. and Barrett C.S. Trans. AIME 194, 1952. 645.

25 Votava E. J. Inst. Metals 90, 1961-62. 129.

26 Giamei A.F. Thesis North Western University Evanston Ill., USA, 1967.

27 Freytag J. PhD Thesis, Universität Stuttgart, 1977.

28 Invensen V.A., Eiduk O.N. and Pivovarov L.I. Sov. Powd. Met. Metal Ceram, 1964. 300.

29 Suzuki H., Yamamoto T. and Hayashi K. J. Japan. Soc. Powder Met. 14, 1967. 262.

30 Gurland J. Trans. AIME, 200, 1954. 285.

31 Rautala P. and Norton T. Proc. 1st Plansee Seminar 303, 1952. Reutte, Planseewerke.

32 Grüter H. Thesis Universität Münster, 1959.

33 Pollock C.B. and Stadelmaier H. Metall. Trans. 1, 1970. 767.

34 Uhrenius B., Carlson B. and Franzén T. Scand. J. Metall. 5, 1976. 49.

35 Harsta A., Johansson T., Rundqvist S. and Thomas J.O. Acta Chem. Scand. 31A, 1977. 260.

36 Johansson T. and Uhrenius B. Met. Sci. 2, 1978. 83.

37 Sarin V.K. Morphology of Eta Phase in Cemented WC-Co alloys. Proceedings of the 1976 Int. Powder Metall. Conference. eds. Hausner H.H. and Taubenblat P.W. (Amer. Powder Metall. Inst. Princeton, N.J.)

38 Rüdiger O., Hirschfeld D., Hoffmann A., Kolaska J., Ostermann G. and Willbrand J. Tech. Mitt. Krupp, Forsch. Ber 29, 1971. 1-14.

39 Rüdiger O. and Hoffmann A. Metall. 24, 1970. 723-734.

40 Kieffer R. and Benesovsky F. Hartmetalle 1965. Wien, New York, Springer-Verlag.

41 Exner H.E. and Gurland J. Powder Metall. 25 Vol. 13, 1970. 13-31.

42 Exner H.E, and Fischmeister H.F. Z. Metallkd 57, 1966. 187.

43 Exner H.E. and Fischmeister H.F. Arch. Eisenhüttenwesen 37, 1966. 417.

44 Öhman S., Pärnama E. and Palmqvist S. Jernkontorets Ann., 151, 1967. 126.

45 Pfau H. and Rix W. Z. Metallkd 43, 1952. 440.

46 Gurland J. Trans. ASM 50, 1958. 1063.

47 Bernard R. Jernkontorets Ann., 147, 1963. 22.

48 Palmqvist S. Verkstäderna 59, 1963. 187.

49 French D.N. J. Am. Ceram. Soc. 52, 1969. 267.

50 Snell P.O. and Pärnama E. Planseeber. Pulvermetall 21, 1973. 271.

51 Hara A., Megata M. and Yazu S. Proc. 8th X-ray Symp. 1969. Kyoto, Japan, Society of Materials.

52 Hara A., Megata M. and Yazu S. Powder Metall. Int. 2, 1970. 43.

53 Amberg S. Jernkontorets Ann., 147, 1963. 218.

54 Exner H.E. Trans AIME 245, 1969. 677.

55 Kreimer G.S. and Alekseeva N.A. Phys Met. Metallogr 13(4), 1962. 117.

56 Kreimer G.S., Vakhovskaya M.R., Tumanov V.I. and Pavlova Z.I. Phys. Met. Metallogr. 13(6), 1962. 91.

57 Fischmeister H.F. and Exner H.E. Arch. Eisenhüttenwesen 37, 1966. 499.

58 Späth S. Metall. 12, 1958. 925.
59 Gurland J. and Bardzil P. Trans. AIME 203, 1955. 311.
60 Exner H.E. and Fischmeister H.F. Prakt. Metallogr. 3, 1967. 18.
61 Pickens J.R. PhD Thesis, Brown University, Providence USA, June 1977.
62 Exner H.E. Int. Metall. Rev. 17, 1972. 25.
63 Gurland J. Trans. AIME 215, 1959. 601.
64 Exner H.E. Powder Metall. 13, 1970. 429.
65 Gurland J. Jernkontorets Ann., 147, 1963. 4.
66 Lee H.C. and Gurland J. Mat. Sci. and Eng. 33, 1978. 125-133.
67 Lindau L. Scand. J. of Metall. 6, 1977. 90-91.
68 Chermant J.L. and Osterstock F. J. Mat. Sci. 11, 1976. 1939-1951.
69 Nakamura M. and Gurland J. Metall. Trans. A, 11A, 1980. 141-146.
70 Viswanadham R.K., Sun T.S., Drake E.F. and Peck J.A. J. Mat. Sci. 16, 1981. 1029.
71 Amberg S. and Doxner H. Powder Metall. 19, 1977. 1.
72 Bartolucci Luyckx S. Metall. 33. Jahragang. Heft 7. July, 1979.
73 Engel U. and Hübner H. J. Mat. Sci. 13(9), 1978. 2003.
74 Almond E.A. and Roebuck B. Metal Sci., Oct. 1977. 458.
75 Grewe H. and Kolaska J. Metall. 32, 1978. 989.
76 Amberg S., Nylander E.A. and Uhrenius B. Powder Metall. Int. 6, 1974. 178.
77 Suzuki H., Hayashi K., Yamamoto T. and Miyake K. J. Japan. Soc. Powder Metall. 475 21, 1974. 108, 222.
78 Lardner E. Powder Metall. 18, 1975. 47.
79 Grewe H. and Osterman G. Tech. Mitt. Krupp 35, 1977. 51.
80 Kreimer G.S., Baranov A.I. and Alekseeva N.A. Hard Alloys, Sb. Tr. Vses. Nauchn. Issled. Inst. Tverd. Splav., No 2, Metallurgizdat, 1960. 57. Izv. Akad. Nauk SSR, Otd. Tekhn. Nauk, Met. i Toplivo, No 3, 1959. 92.

81 Chermant J.L., Iost A. and Osterstock F. Mech. Characteristics of Carbide-Metal Composites and the Correlation with Microstructural Parameters. Proc. of the British Ceramic Soc. Vol 25, 1975. 197-209.

82 Fischmeister H. Tekn. Tids., 1965. 761.

83 Platov A.B. Poroshkovaya Met. No 3(9), 1962. 63.

84 Dawihl W. and Frisch B. Arch. Eisenhüttenwesen 33, 1962. 61.

85 Engle E.W. Powder Metallurgy (edited by J. Wulff) Cleveland Ohio. Amer. Soc. Metals, 1942.

86 Kreimer G.S., Tumanov V.I., Kamenskaya D.S. and Pavlova Z.I. Physics Metals Metallography 17(4), 1964. 85.

87 Aschan L.J., Johansson I. and Gustafsson L.E. Proceedings of 4th Nordic High Temp. Symp. Nortemps Vol 1 1975. 227-245.

88 Kreimer G.S., Safonova O.S. and Baranov A.I. Zh. Tekhn. Fiz., 25(1), 1955. 117.

89 Gurland J. Trans. Met. Soc. AIME 227, 1963. 1146.

90 Tu K.N. and Gurland J. Proceedings of 2nd Internat. Powder Metall Conf. Prague, 1967 (Prague Academia Publ.).

91 Drucker D.C. High Strength Materials. (ed: Zackay V.F.) 1965. 795. New York, London (John Wiley).

92 Suzuki H. Trans. Japan. Inst. Metals 7, 1966. 112.

93 Suzuki H. and Kubota H. Planseeber Pulvermet 14, 1966. 96.

94 Kubota H., Ishida R. and Hara A. Sumitomo Elect. Tech. Rev. 6, 1965. 87; Trans. Indian Inst. Metals 17(5), 1964. 132.

95 Lindau L. Fracture 1977. ICF4 ed. Taplin D.M.R. University of Waterloo Press, 2, 1977. 215-221.

96 Lueth R.C. Fracture Mechanics of Ceramics Vol 2, eds. Bradt R.C., Hasselman D.P.H. and Lange F.F. Plenum Press N.Y. 1974. 791-806.

97 Chermant J.L. and Osterstock F. J. of Mat. Sci. 11, 1976. 1939-1951.

98 Nakamura M. and Gurland J. Metall. Trans A Vol 11A Jan. 1980. 141-146.

99 Viswanadham R.K., Sun T.S., Drake E.F. and Peck J.A. J. of Mat. Sci. 16, 1981. 1029-1038.

100 Ingelstrom N. and Norberg H. Eng. Fract. Mech. Vol 6, 1974. 597-607.

101 Chermant J.L., Deschanvres A. and Osterstock F. Fracture Mechanics of Ceramics Vol 4, eds. Bradt R.C., Hasselman D.P.H. and Lange F.F. Plenum Press N.Y. 1974. 891-901.

102 Braiden P.M., Davidge R.W. and Airey R. J. Mech. Phys. Solids Vol 25, 1977. 257-268.

103 Osterstock F. Thesis Université de Caen, Caen, France. 1980.

104 Miyake K., Fujiwara Y. and Nishigaki K. Nippon Kinzoku Gakkai-Shi 32, 1968. 1128-1131.

105 Davies T.J. and Barhana S. Planseeberichte Pulvermetallurgie Vol 20, No 1, 1972.

106 Kreimer G.S., Sidorin I.I. and Tishchenkova E.F. Collection: Manufacture of Parts by Powder Metall. Techniques, Vses. Inst. Nauchn. i Tekhn. Inform.

107 Kreimer G.S., Sidorin I.I. and Tishchenkova E.F. Izv. Akad. Nauk SSSR Otd. Tekhn. Nauk, No 3, 1958. 113.

108 Johansson I., Persson G. and Hiltscher R. Powder Metall. Vol 13, No 26. 1970.

109 Evans A.G. and Linzer M. Int. J. of Fracture 12, 1976. 217-222.

110 Lueth R.C. J. of General Electric Eng. Materials; Materials Technology, Spring 1981. 27-30.

111 Almond E.A. and Roebuck B. Metals Technology Feb. 1980. 83-85.

112 Viswanadham R.K. Private communication, Nov., 1981.

113 Almond E.A. Private communication, July, 1981.

114 Viswanadham R.K. Private communication, April, 1982.

115 Evans A.G. Int. J. of Fracture 16, 1980. 485-498.

116 Luyckx S.L. Fracture 1977, ICF4, ed. Taplin D.M.R. University of Waterloo Press, 2, 1977. 223.

117 Chermant J.L., Deschanvres A. and Iost A. Fracture Mechanics of Ceramics Vol 1, eds. Bradt R.C., Hasselman D.P.H. and Lange F.F. Plenum N.Y. 1974. 347-366.

118 Evans A.G., Heuer A.H. and Porter D.L. Fracture 1977 ICF4, ed. Taplin D.M.R. University of Waterloo Press, 1, 1977. 529-556.

119 Evans A.G. Fracture Mechanics of Ceramics Vol 1, eds. Bradt R.C., Hasselman D.P.H. and Lange F.F. Plenum Press N.Y., 1974. 17-48.

120 Outwater J.O. and Jerry D.J. On the Fracture Energy of Glass. Interim Rept., Contract Nonr. 3219 (01)(X) University of Vermont, Burlington, VT, Aug. 1966.

121 Trantina G.G. Journal of the Amer. Ceramic Soc. Vol 60 (7-8) July-Aug. 1977. 338-341.

122 Li-Shing Li and Pabst R.F. Journal of Materials Science 15, 1980. 2861-2866.

123 Pletka B.J., Fuller E.R. and Koepke B.G. Fracture Mechanics Applied to Brittle Materials ASTM STP 678 ed. Freiman S.W., 1979. 19-37.

124 Williams D.P. and Evans A.G. Journal of Testing and Evaluation JTEVA Vol 1 No 4, July 1973. 264-270.

125 Outwater J.O., Murphy M.C., Kumble R.G. and Berry J.T. Fracture Toughness and Slow Stable Cracking ASTM STP 559, 1974. 127-138.

126 McKinney K.R. and Smith R.L. Journal of the Amer. Ceramic Soc. Vol 56, No 1, 1973. 30-52.

127 Evans A.G. Int. Journal of Fracture, Vol 9 No 3, Sept. 1973. 267-275.

128 Murray M.F. and Perrot C.M. 1976 Proc. Int. Cont. Hard Materials Tool Technology p.314. Carnegie Mellon University, Pittsburgh, Penn.

129 Evans A.G. Private communication, 1980.

130 Fuller E.R. Fracture Mechanics Applied to Brittle Materials ASTM STP 678. ed. Freiman S.W. 1979. 3-18.

131 Evans A.G. Journal of Mat. Science 7, 1972. 1137-1146.

132 Champomier F.P. Fracture Mechanics Applied to Brittle Materials, ASTM STP 678. Freiman S.W. 1979. 60-72.

133 Murphy M.C., Kumble R.G. and Berry J.T. Amer. Foundrymen's Soc. Transactions Vol 81, 1973. 158-162.

134 Annis C.G. and Cargill J.S. Fracture Mechanics of Ceramics, Vol 4. eds. Bradt R.C., Hasselman D.P.H. and Lange F.F. Plenum Press, N.Y. 1978. 737-744.

135 Bruce J.G., Gerberich W.M. and Koepke B.G. Fracture Mechanics of Ceramics, Vol 4, eds. Bradt R.C., Hasselman D.P.H. and Lange F.F. Plenum Press, N.Y. 1978. 687-709.

136 Pletka B.J. and Wiederhorn S.M. Fracture Mechanics of Ceramics, Vol 4, eds. Bradt R.C., Hasselman D.P.H. and Lange F.F. Plenum Press, N.Y., 1978. 745-759.

137 Pabst R.F. and Weick J. J. of Mat. Sci. 16, 1981. 836-838.

138 Shetty D.L. and Virkar A.V. Journal of the Amer. Ceramic Society Vol 61, No 1-2, Jan.-Feb. 1978. 93-94.

139 Virkar A.V. and Gordon R.S. Journal of the Amer. Ceramic Soc., Vol 58 No 11-12, Nov.-Dec. 1975. 536-537.

140 Evans A.G., Russell L.R. and Richerson D.W. Metallurgical Transactions, Vol 6A, April, 1975. 707-716.

141 Wiederhorn S.M. Journal of the Amer. Ceramic Soc. Vol 50, 1967. 407.

142 Wiederhorn S.M. Int. J. Fracture Mech. 4, 1968. 171.

143 Nadeau J.S. Journal of the Amer. Ceramic Soc. Vol 57, No 7, 1974. 303-306.

144 Nadeau J.S., Mindess S. and Hay J.M. Journal of the Amer. Ceramic Soc., Vol 57, No 2, 1974. 51-54.

145 Evans A.G. and Linzer M. NBS Washington, Internal Report, 1974.

146 Evans A.G. and Fuller E.R. Metallurgical Transactions, Vol 5, Jan. 1974. 27-33.

147 Wiederhorn S.M. Fracture Mechanics of Ceramics, Vol 2, eds. Bradt R.C., Hasselman, D.P.H. and Lange F.F. Plenum Press, N.Y. 1974.

148 Kies J.A. and Clark B.J. Fracture 1969. ed. Pratt P.L. Chapman and Hall Ltd., London, 1969. 483-491.

149 Beacham C.D., Kies J.A. and Brown B.F. Materials Research and Standards, 11, 1970. 30.

150 Evans A.G., Clifton J.R. and Anderson E. Cement and Concrete Research . Vol 6, 1976. 535-548.

151 Hakeem M.I. and Philips M.G. Journal of Mat. Science, Vol 14, 1979. 2901-2905.

152 Davidge R.W., McLaren J.R. and Tappin G. Journal of Mat. Science, Vol 8, 1973. 1699-1705.

153 Dalgleish B.J., Pratt P.L. and Rawlings R.D. Materials Science and Engineering 45, 1980. 9-20.

154 Wright B.D. Private communication Nov., 1981.

155 Tait R.B. and Böhm H. In situ Scanning Electron Microscope Observations of Double Torsion Fracture of Concrete. Electron Microscopy Soc. of South Africa. Poceedings Vol 10, 1980. 17-18.

156 Tait R.B. Private comunication May, 1981.

157 Wiederhorn S.M., Johnson H., Diness A.M. and Heuer A.H. J. Am. Ceramic Soc. Vol 57, n 8. Aug. 1974. 336-341.

158 Wiederhorn S.M., Evans A.G. and Roberts D.L. Fracture Mechanics of Ceramics Vol 2, eds. Bradt R.C., Hasselman D.P.H. and Lange F.F. 1974.

159 Garrett G.G. and Knott J.F. Met. Trans. A Vol 7A, 1976. 804.

160 Garrett G.G. and Knott J.F. Met. Trans. A Vol 6A, August, 1975. 1663-1665.

161 Ritchie R.O. and Knott J.F. Acta Metall. Vol 21 May, 1973. 639-648.

162 Miller G.A. Trans. ASM 61, 1968. 442.

163 Clark W.G. and Wessel E.T. ASTM Special Technical Publ. No 463, 1970. 106.

164 Evans P.R.V., Owen N.B. and Hopkins B.E. Eng. Fract. Mech. 3, 1971. 463.

APPENDIX 1

Tabulation of selected fracture toughness data for WC-Co alloys, where there is sufficient microstructural information reported to calculate the nominal and true mean free path.

The following equations have been used:

$$\lambda_{nom} = \frac{f_{Co}\,\bar{d}}{(1-f_{Co})}$$

$$\lambda_{true} = \frac{f_{Co}\,\bar{d}}{(1-f_{Co})(1-C)}$$

Values of λ_{nom} and λ_{true} quoted in microns (μm).

In cases where the contiguity C has not been reported or differs greatly from other published values, Lee and Gurland's graph[66] has been used to obtain C. (Section 2.7.3).

CHERMANT ANI OSTERSTOCK [97]

ALLOY	wt%	vol%	$\bar{d}$ µm	$\frac{\lambda_{nom}}{\bar{d}} \frac{f_{fc}}{1-f_{fc}}$	C CHERMANT +OSTERSTOCK	λ_{true} CHERMANT +OSTERSTOCK	C FROM FIG 2.5	$\frac{\lambda_{true}}{\bar{d}} \frac{f_{fc}}{(1-f_c X_i - c)}$	K_{IC} MNm$^{-3/2}$
	3,0	5	2,2	0,116	0,744	0,46	0,72	0,414	8,8
	5,9	10	2,2	0,244	0,623	0,65	0,51	0,498	[illegible]
	9,1	15	2,2	0,388	0,523	0,81	0,39	0,636	[illegible]
	13,8	22	2,2	0,621	0,456	1,0	0,28	0,863	[illegible]
	19,5	30	2,2	0,943	0,410	1,35	0,18	1,150	[illegible]
	25	37	2,2	1,292	0,368	1,80	0,13	1,485	[illegible]
	3,0	5	1,1	0,058	0,76	0,29	0,72	0,207	[illegible]
	5,9	10	1,1	0,122			0,51	0,249	[illegible]
	9,1	15	1,1	0,194			0,39	0,318	[illegible]
	13,8	22	1,1	0,311	0,484	0,68	0,28	0,432	[illegible]
	19,5	30	1,1	0,472	0,450	0,86	0,19	0,576	[illegible]
	25	37	1,1	0,646	0,432	1,04	0,13	0,749	[illegible]
	3,0	5	0,7	0,037	0,800	0,16	0,72	0,132	8,5
	5,9	10	0,7	0,078	0,700	0,22	0,51	0,159	8,9
	9,1	15	0,7	0,123	0,600	0,31	0,39	0,202	[illegible]
	13,8	22	0,7	0,198	0,554	0,46	0,28	0,275	[illegible]
	19,5	30	0,7	0,300	0,516	0,66	0,18	0,366	[illegible]
	25	37	0,7	0,411	0,500	0,82	0,13	0,472	[illegible]

INGELSTROM AND NORDBERG [100]

ALLOY	wt %	vol %	$\bar{d}$ μm	$\frac{\lambda_{nom}\,\bar{d}\,f_{c\omega}}{1-f_{c\omega}}$			C FROM FIG 2.5	$\frac{\lambda_{true}\,\bar{d}\,f_{c\omega}}{(1-f_{c\omega})(1-C)}$	K_{IC} $MNm^{-3/2}$
6F	6	10,1	1,0	0,113			0,50	0,226	10,0
6M	6	10,1	1,5	0,169			0,50	0,338	12,4
8F	8	13,3	1,3	0,199			0,42	0,343	12,3
8C	8	13,3	3,2	0,491			0,42	0,847	18,2
11M	11	17,7	1,9	0,414			0,34	0,627	17,5
11C	11	17,7	3,3	0,719			0,34	1,089	17,4
15M	15	23,7	1,9	0,591			0,25	0,788	17,6
15C	15	23,7	3,3	1,027			0,25	1,369	18,5
20M	20	30,6	1,8	0,794			0,17	0,957	20,3
25M	25	37,0	3,0	1,764			0,13	2,028	20,3

LINDAU [95]

ALLOY	wt %	vol %	$\bar{d}$ μm	λ_{nom} LINDAU	$\frac{\lambda_{nom}\,\bar{d}\,f_{c\omega}}{1-f_{c\omega}}$		C FROM FIG 2.5	$\frac{\lambda_{true}\,\bar{d}\,f_{c\omega}}{(1-f_{c\omega})(1-C)}$	K_{IC} $MNm^{-3/2}$
1	6,0	10	3,0	0,7	0,33		0,51	0,67	10,8
2	6,0	10	1,1	0,25	0,12		0,51	0,24	9,2
3	9,2	15	2,9	0,95	0,51		0,39	0,84	17,3
4	15,8	25	3,6	1,90	1,20		0,24	1,58	23,1
5	14,5	23	0,95	0,35	0,28		0,26	0,38	11,9

LUETH 96

ALLOY	wt%	vol%	$\bar{d}$ NOMINAL μm	λ_{nom} LUETH	$\frac{\lambda_{nom}\bar{d}f_{co}}{1-f_{co}}$		C FROM FIG 2.5	$\frac{\lambda_{true}\bar{d}f_{co}}{(1-f_{co})(1-C)}$	K_{IC} $MNm^{-3/2}$
	3	5,2	1,5	0,09	0,082		0,70	0,273	7,14
	3	5,2	2,5-3	0,14	0,150		0,70	0,500	10,55
	6	10,1	7-8		0,844		0,50	1,688	14,29
	9	14,8	1,5	0,16	0,262		0,39	0,430	9,23
	9	14,8	2,5-3	0,38	0,479		0,39	0,785	12,75
	9	14,8	7-8	1,05	1,31		0,39	2,148	20,88
	15	23,7	1,5	0,29	0,467		0,25	0,623	13,74
	15	23,7	2,5-3	0,65	0,856		0,25	1,141	16,49
	15	23,7	7-8	1,4	2,335		0,25	3,113	24,18

PICKEN'S WORK ON LUETH'S ALLOYS 61

	wt %	vol%	$\bar{d}$ MEASURED μm	λ_{nom} PICKENS		C PICKENS	λ_{true} PICKENS	K_{IC} LUETH $MNm^{-3/2}$	K_{IC} PICKENS $MNm^{-3/2}$
3F	3	5,1	1,06	0,058		0,55	0,128	7,14	9,43
9F	9	14,8	1,16	0,202		0,27	0,276	9,23	11,34
9M	9	14,8	1,37	0,238		0,27	0,298	12,75	12,40
9C	9	14,8	1,24	0,216		0,27	0,296	20,88	11,59
15F	15	23,6	0,96	0,297		0,25	0,395	13,74	12,98
15M	15	23,6	1,88	0,581		0,25	0,776	16,49	15,34
15C	15	23,6	3,73	1,15		0,22	1,47	24,18	19,22

PICKENS [61]

ALLOY	wt%	vol%	$\bar{d}$ μm	λ_{nom} PICKENS			C PICKENS	λ_{true} PICKENS	K_{IC} $MNm^{-3/2}$
ε	4,5	7,6	0,9	0,074			0,458	0,137	9,28
883	6	10,1	0,9	0,101			0,573	0,237	10,92
φ	6	10,1	0,98	0,110			0,422	0,190	9,90
γ	6	10,1	2,84	0,319			0,373	0,509	13,14
k	6,3	10,4	1,5	0,174			0,483	0,255	11,90
κ	9	14,8	1,25	0,217			0,311	0,315	12,00
6	9	14,8	1,79	0,311			0,274	0,429	13,32
4	9,3	15,2	1,74	0,311			0,363	0,489	13,40
β	10,5	17,1	1,45	0,326			0,383	0,528	13,87
θ	12	19,3	1,41	0,337			0,223	0,434	13,81
τ	12,5	20,0	1,66	0,417			0,231	0,543	14,32
55A	13	20,8	1,50	0,404			0,209	0,511	15,34
ω	15	23,6	1,58	0,488			0,190	0,602	16,31
I	16	25,0	1,30	0,433			0,376	0,694	15,19
II	16	25,0	1,50	0,500			0,273	0,688	15,60
ι	20	30,6	1,04	0,459			0,199	0,573	16,10
N	20	30,6	1,54	0,679			0,120	0,771	16,91
S	20	30,6	3,08	1,35			0,148	1,580	18,16
J	25	36,9	1,09	0,637			0,140	0,741	17,91
O	25	36,9	1,57	0,918			0,128	1,050	19,83
T	25	36,9	2,05	1,200			0,137	1,370	19,31

NAKAMURA AND GURLAND [98]

ALLOY	wt%	vol%	$\bar{d}$ μm	λ_{nom} NAKAMURA +GURLAND		C NAKAMURA +GURLAND	λ_{true} NAKAMURA +GURLAND	$\lambda_{true}\frac{1-f_{Co}}{f_{Co}}(1-C)$	K_{IC} $MNm^{-3/2}$
1	6,0	10,0	0,97	0,108		0,33	0,16	0,16	8,6
2	6,0	10,0	1,09	0,121		0,41	0,20	0,21	9,0
3	6,0	10,0	2,09	0,232		0,60	0,58	0,58	9,8
4	12,5	20,0	0,89	0,223		0,22	0,28	0,29	12,7
5	12,5	20,0	1,17	0,293		0,16	0,35	0,35	13,2
6	12,5	20,0	2,44	0,610		0,22	0,78	0,78	16,8
7	19,8	30,5	1,10	0,483		0,16	0,57	0,58	15,0
8	19,8	30,5	1,50	0,658		0,13	0,76	0,76	18,0
9	19,8	30,5	2,96	1,299		0,15	1,53	1,53	19,5
10	27,4	40,0	1,22	0,813		0,16	0,64	0,968	18,0
11	27,4	40,0	1,63	1,087		0,11	0,81	1,22	19,4
12	27,4	40,0	3,60	2,40		0,14	1,84	2,79	26,2

VISWANADHAM SUN DRAKE AND PECK [99]

ALLOY	wt%	vol%	$\bar{d}$ μm	λ_{nom} VISWANADHAM ET AL.			C VISWANADHAM ET AL.	λ_{true} VISWANADHAM ET AL.	K_{IC} $MNm^{-3/2}$
19B	10,5	17,2	1,8	0,37			0,33	0,55	14,26
19C	7,9	13,3	2,5	0,38			0,40	0,63	14,09
19D	5,7	9,3	4,5	0,46			0,50	0,92	14,92
21B	13,8	22,0	1,8	0,51			0,26	0,69	15,36
21C	12,2	19,7	2,5	0,61			0,29	0,86	16,41
21D	10,2	16,7	3,8	0,76			0,33	1,13	17,11

APPENDIX 2

Information used to determine microstructural parameters for the alloys tested.

The Appendix contains:

(i) Typical microstructures

(ii) Weight percentage to volume percentage conversion

(iii) A graph of Vicker's hardness vs mean free path to show how the values compare with those reported in the literature.

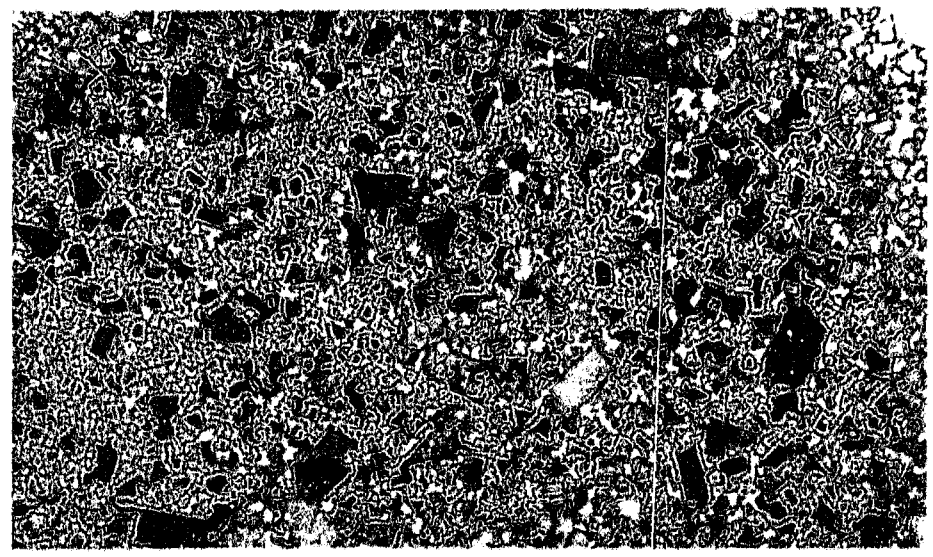

Figure A2.1 Alloy S6, WC-6Co fine grained x 1200

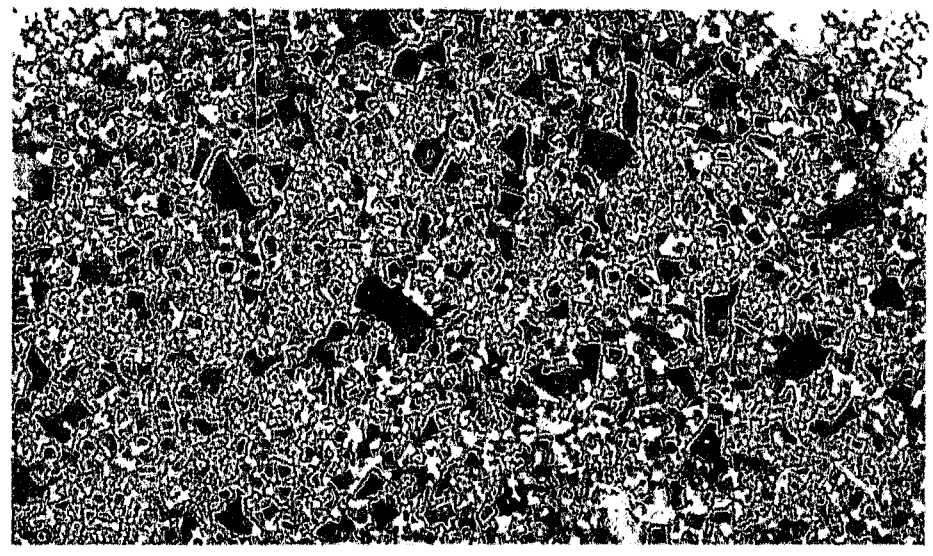

Figure A2.2 Alloy S10, WC-10Co fine grained x 1200

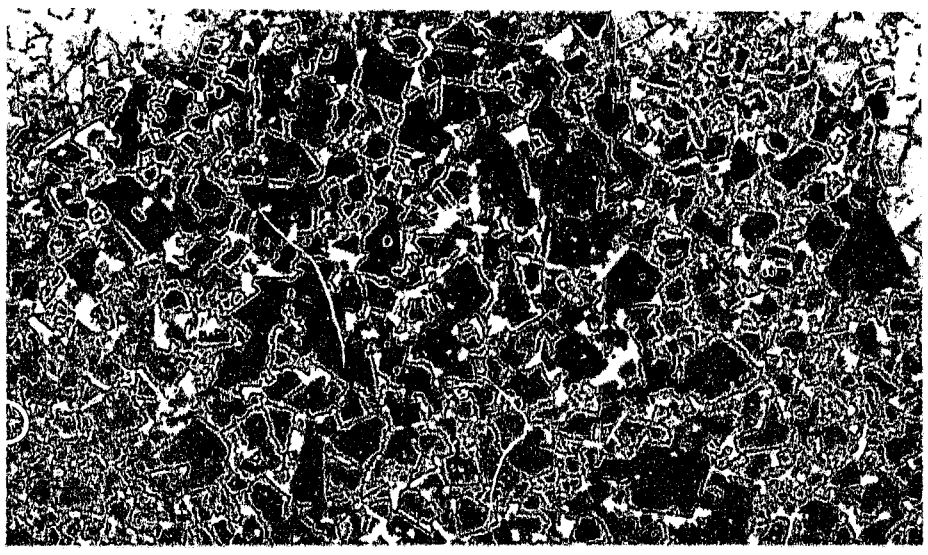

Figure A2.3 Alloy G6, WC-6Co coarse grained x 1200

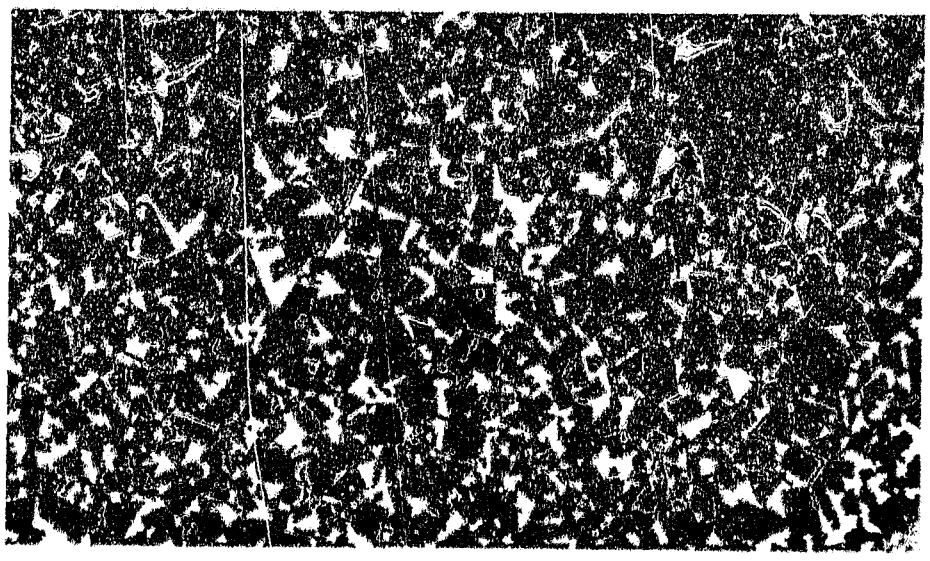

Figure A2.4 Alloy G10, WC-10Co coarse grained x 1200

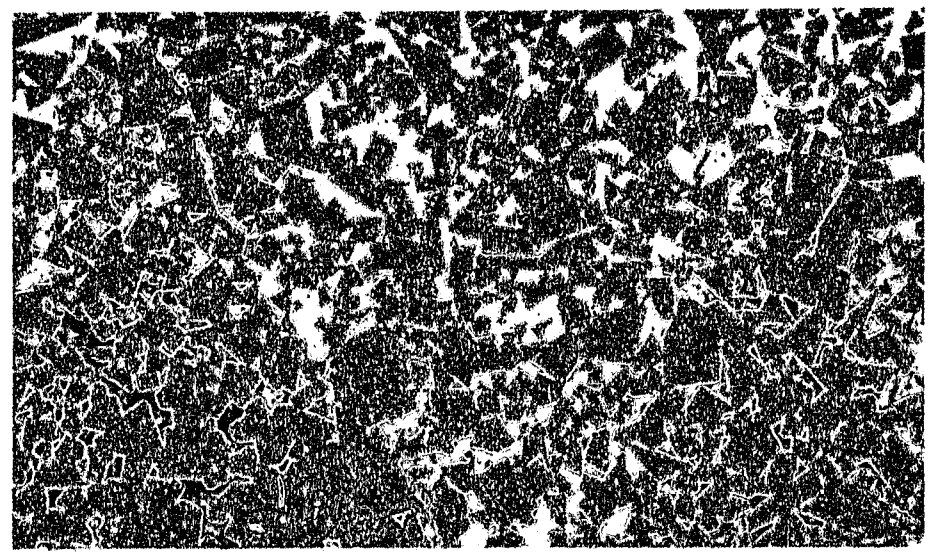

Figure A2.5 Alloy G15, WC-15Co coarse grained x 1200

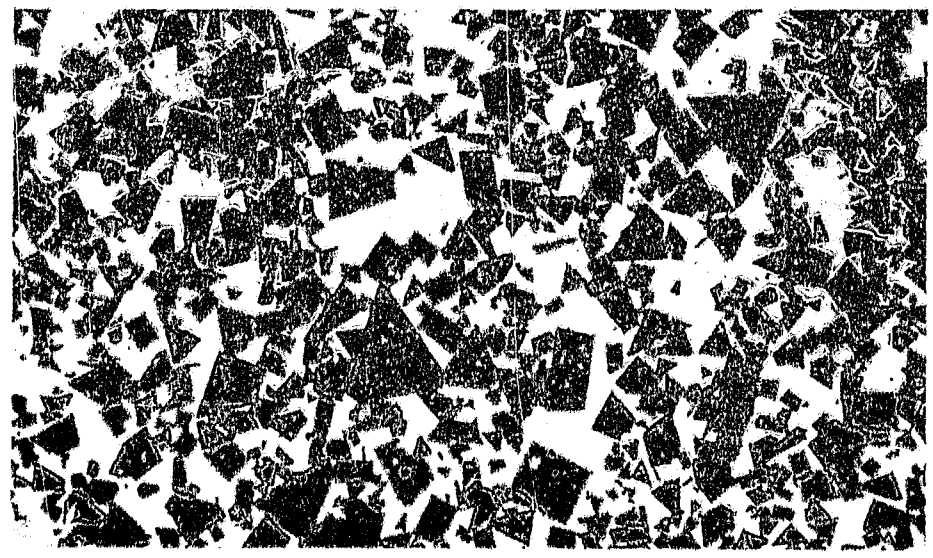

Figure A2.6 Alloy 25E, WC-25Co coarse grained x 1200

WEIGHT PERCENTAGE TO VOLUME PERCENTAGE CONVERSION

Density of WC = 15,7

Density of Co = 8,9

$$\text{Weight fraction Co} = \frac{8,9(\text{Volume fraction Co})}{15,7(\text{Volume fraction WC}) + 8,9(\text{Volume fraction Co})}$$

$$= \frac{8,9f_{Co}}{15,7(1 - f_{Co}) + 8,9f_{Co}}$$

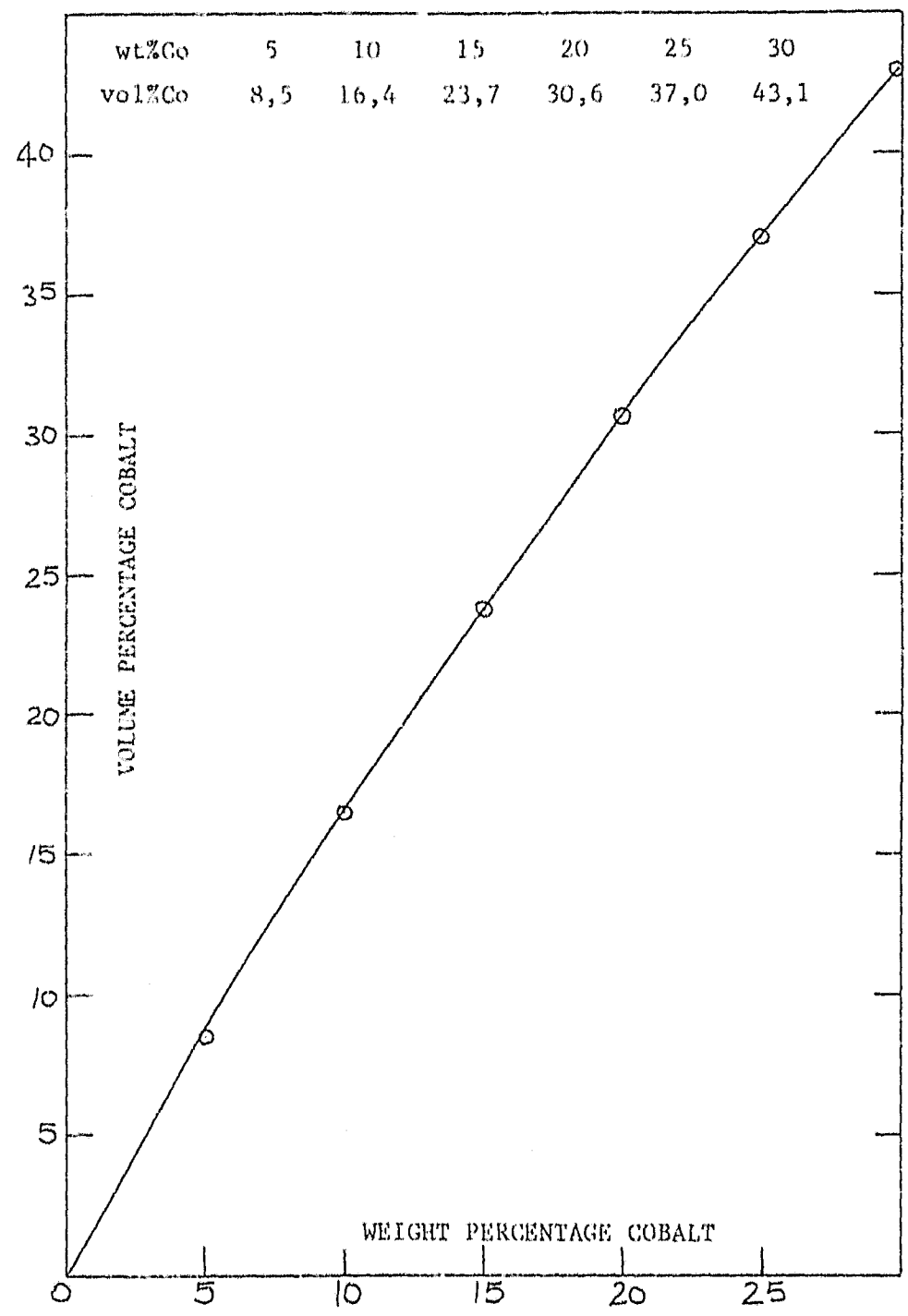

Figure A2.7

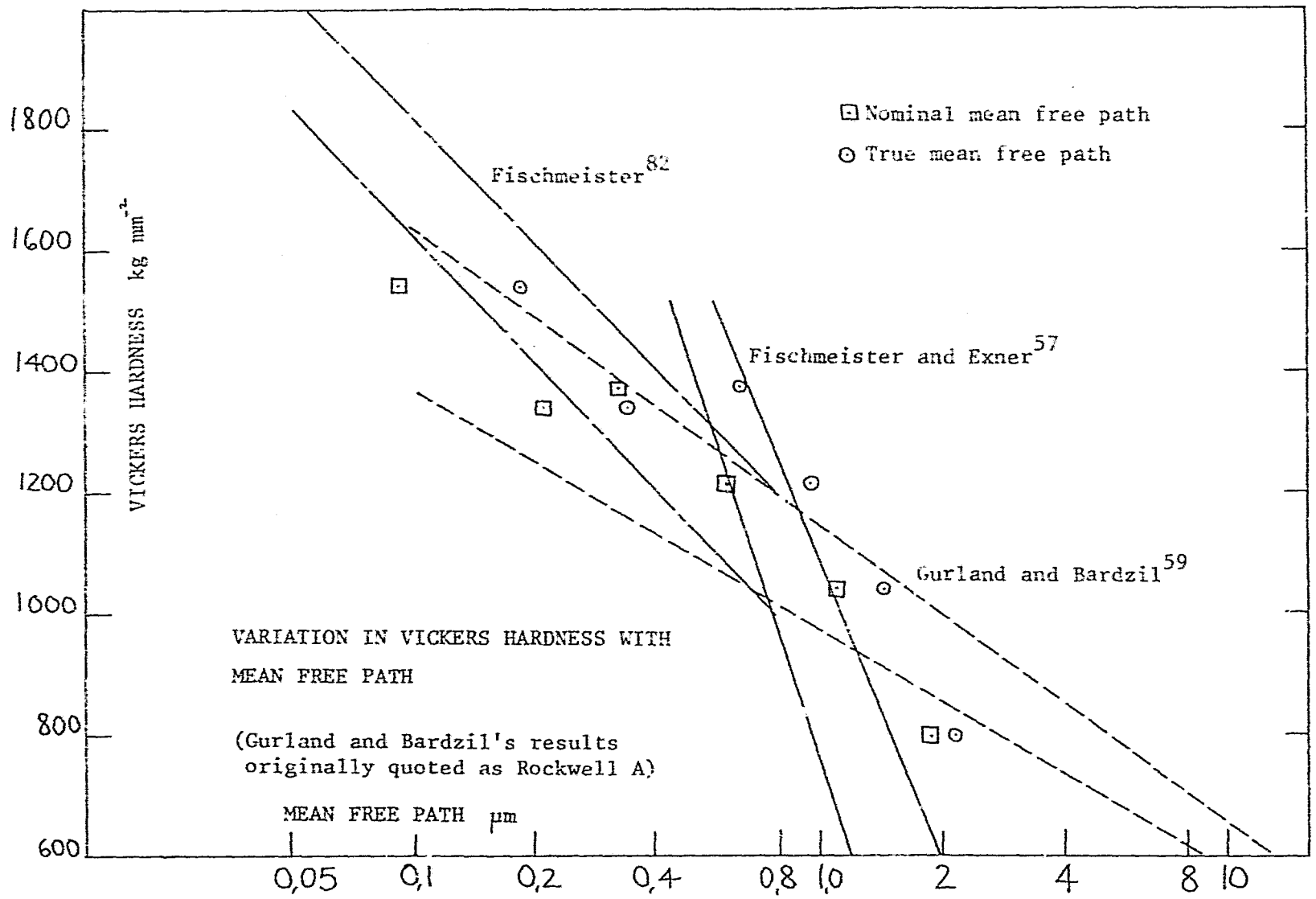
1800
1600
1400
1200
1000
800
600
VICKERS HARDNESS kg mm⁻²
Nominal mean free path
True mean free path
Fischmeister[82]
Fischmeister and Exner[57]
Gurland and Bardzil[59]
VARIATION IN VICKERS HARDNESS WITH
MEAN FREE PATH
(Gurland and Bardzil's results
originally quoted as Rockwell A)
MEAN FREE PATH μm
0,05
0,1
0,2
0,4
0,8
1,0
2
4
8
10

Figure A2.8

APPENDIX 3

Examples of specimens with large defects apparent on the surface.

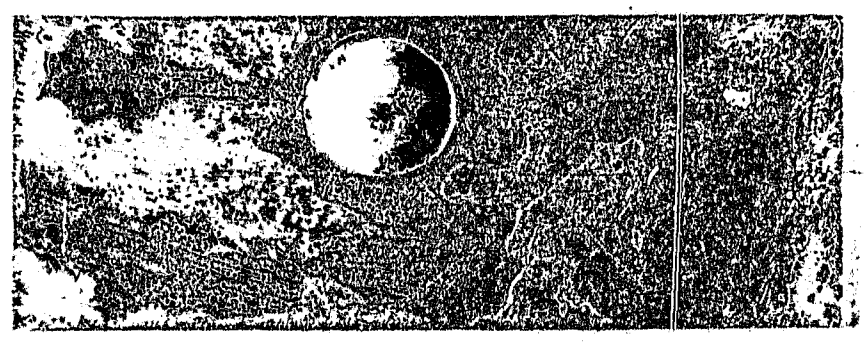

Figure A3.1 Alloy 25E

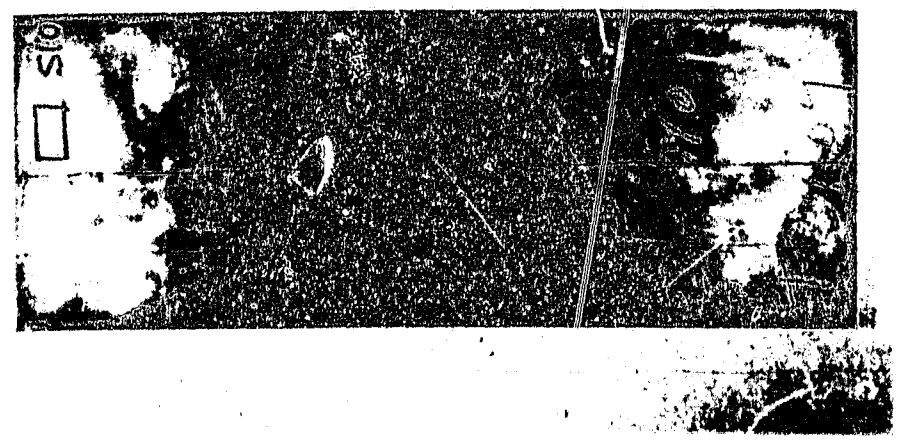

Figure A3.2 Alloy S10

APPENDIX 4

Drawings for test rig load system

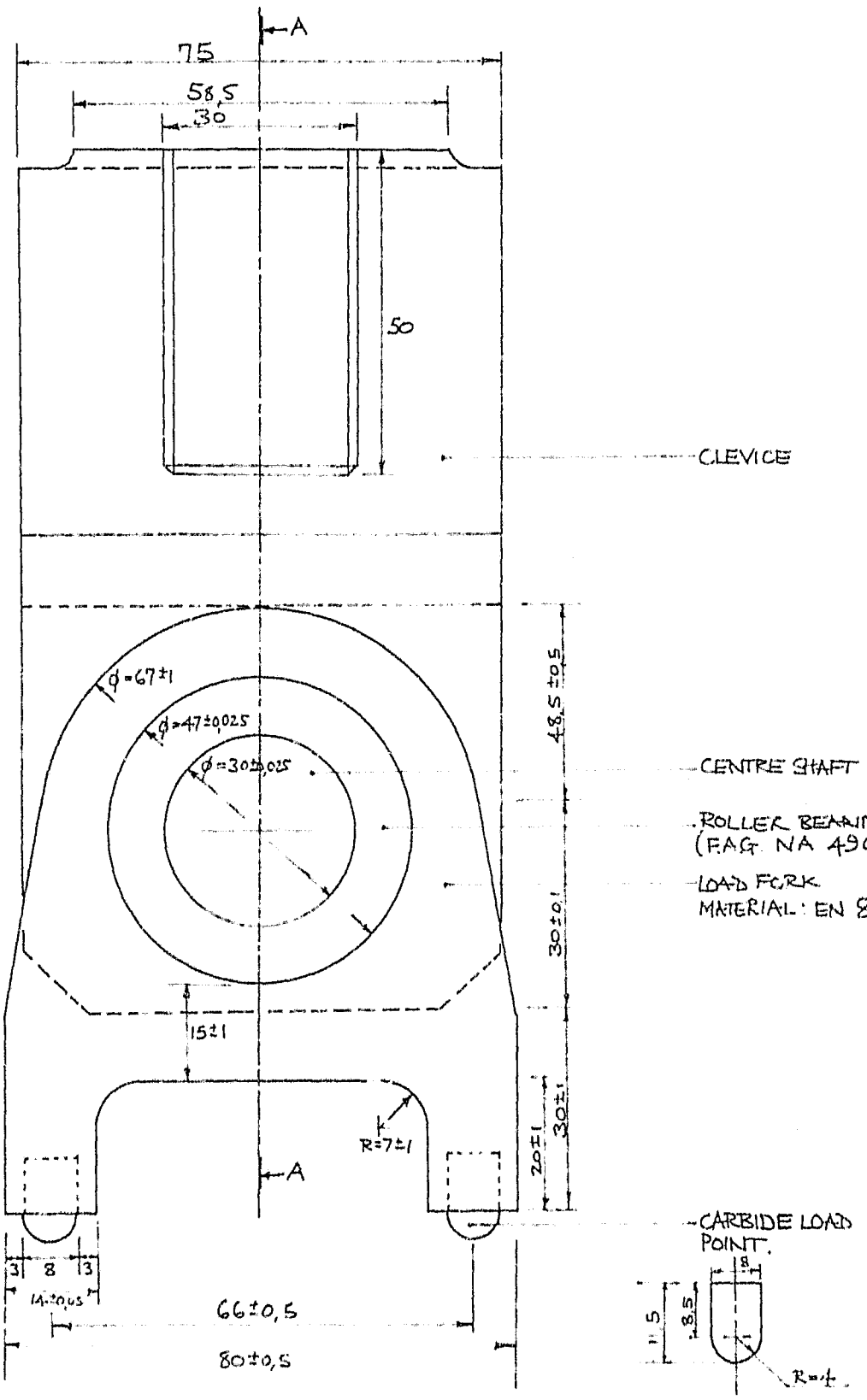

DESIGN OF LOAD FORK FOR D.T. SPECIMEN

SCALE 1:1

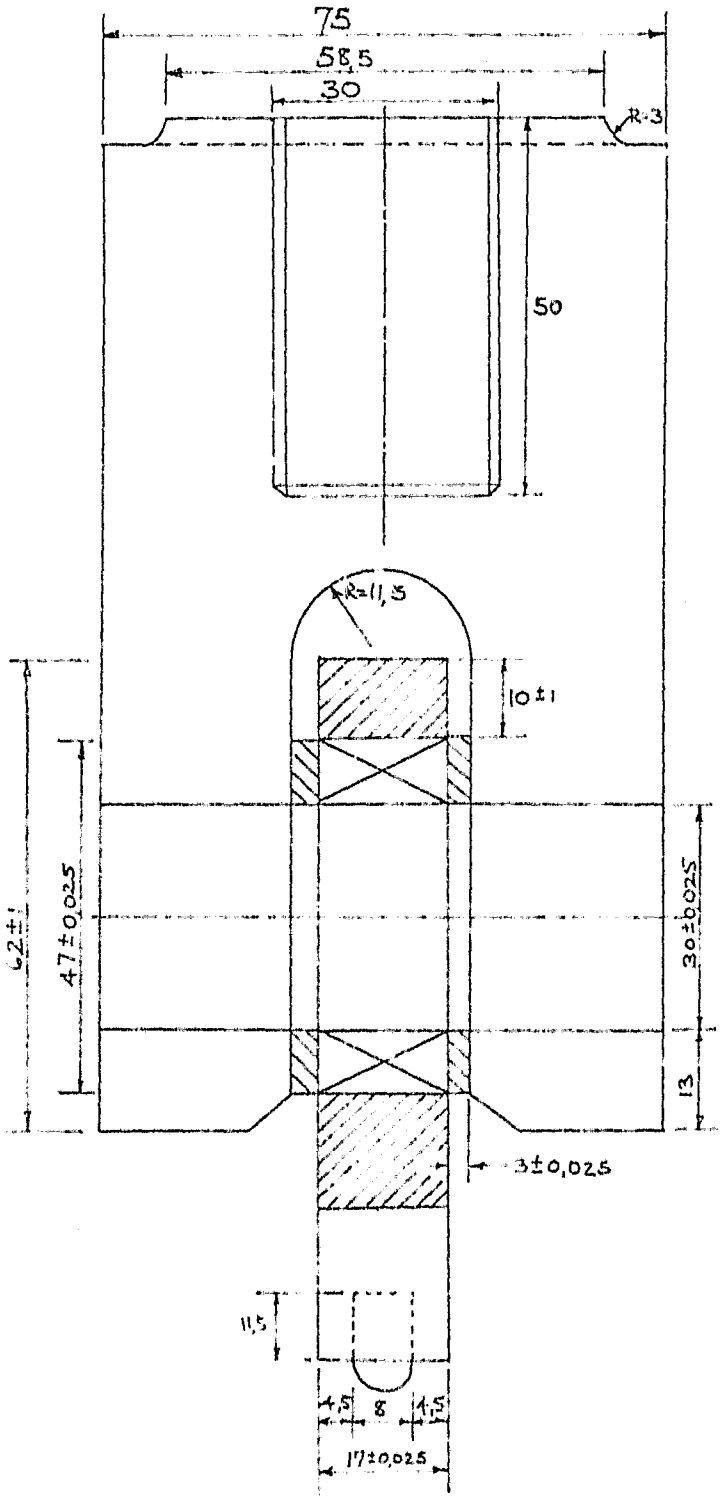

SECTION A-A

DESIGN OF LOAD FORK FOR D.T. SPECIMEN.

SCALE 1:1

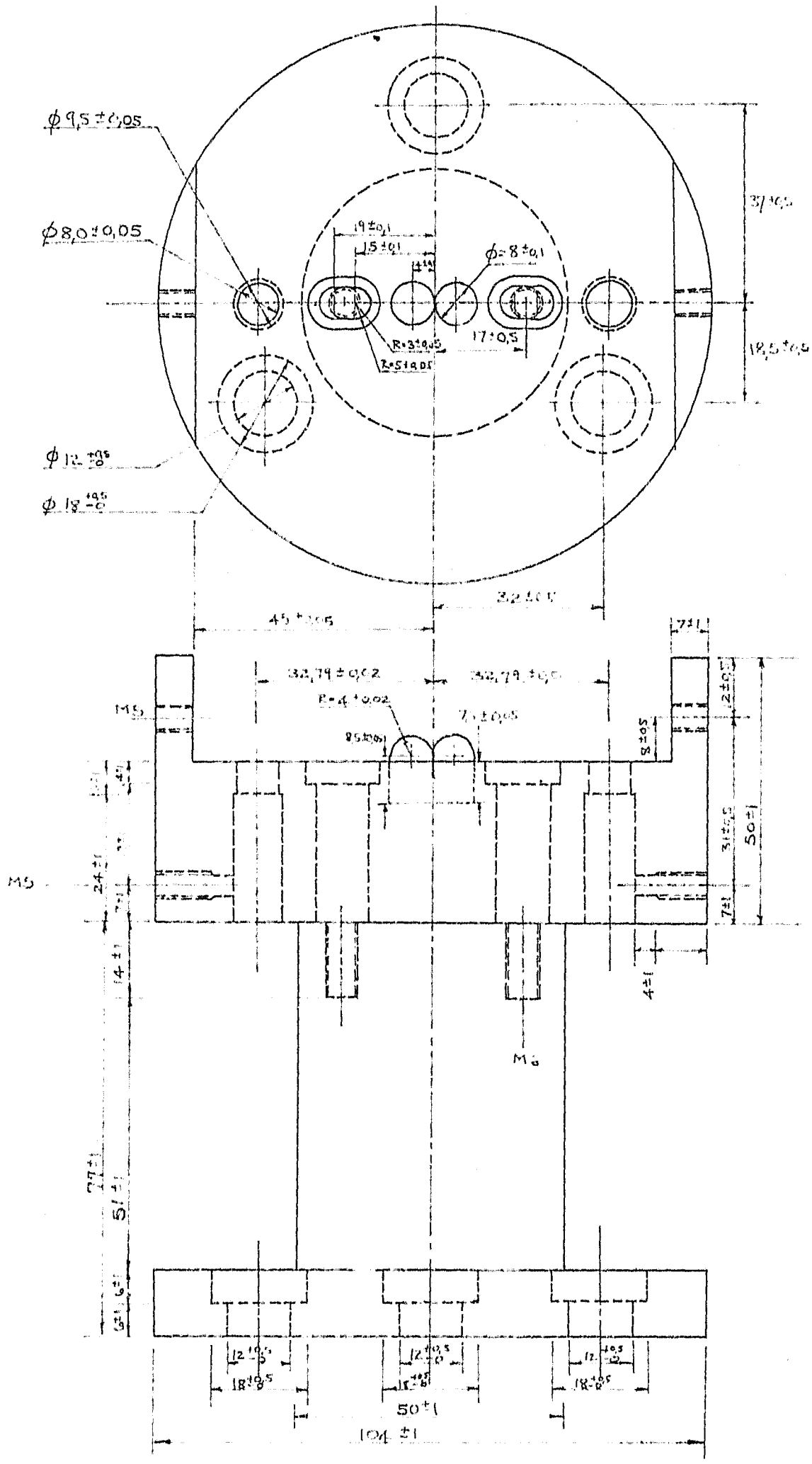

DESIGN FOR SUPPORT AND ALIGNMENT AT LOADED END OF D.T. SPECIMEN.

SCALE 1:1 MATERIAL : EN 8.

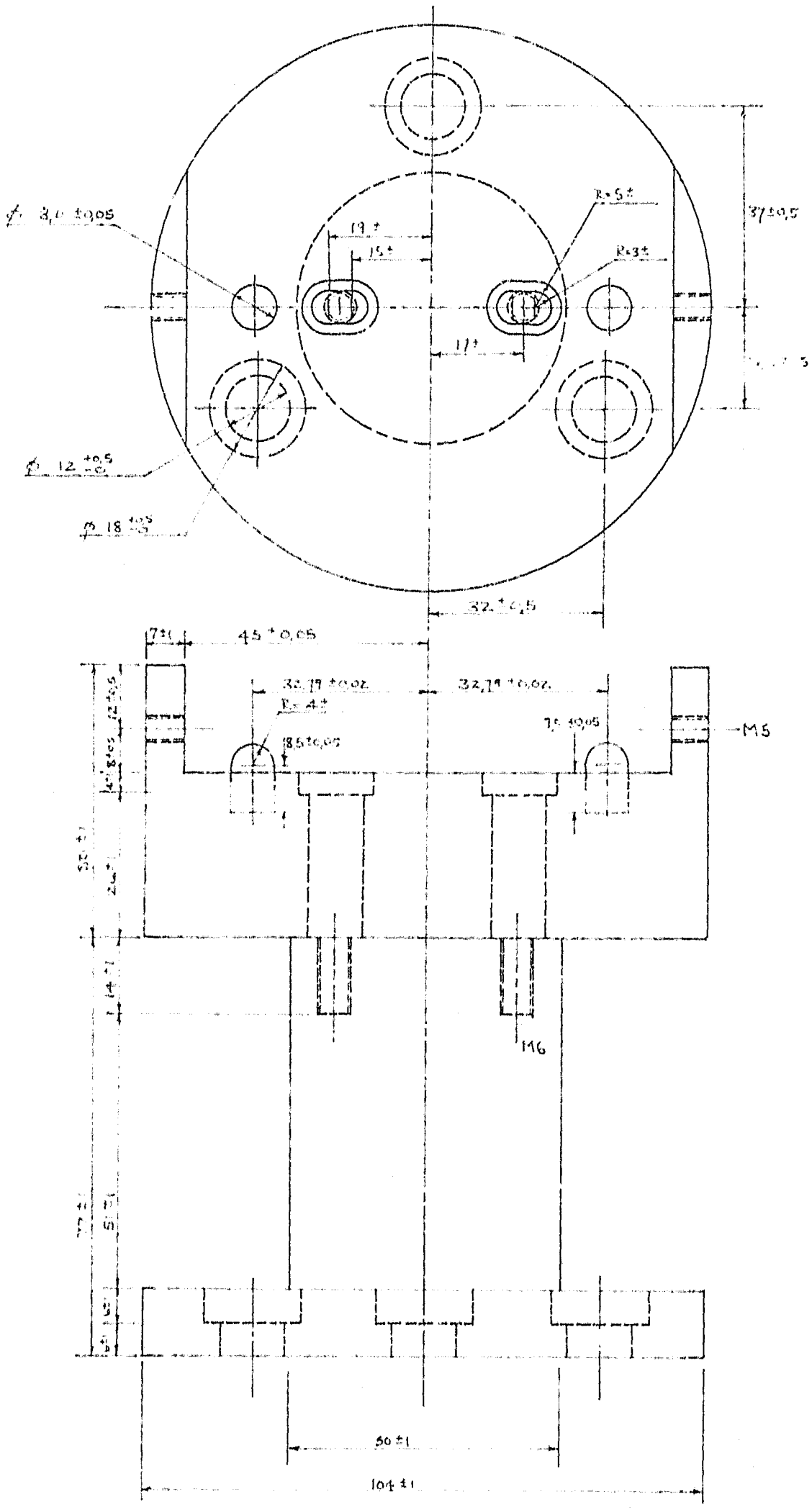

DESIGN FOR SUPPORT AND ALIGNMENT AT REMOTE END OF D.T. SPECIMEN.
SCALE 1:1

APPENDIX 5

Details of unsuccessful attempts to obtain crack growth rate data by indirect monitoring.

(i) Static crack growth measurement by load relaxation

(ii) Fatigue crack growth measurement by monitoring deflections of the load points as the crack propagates

(i) Static crack gr wth

Crack growth rate measurement by load relaxation monitoring under displacement control is given by the following equation a defined in Section 3.4.4.1.

$$\frac{da}{dt} = \frac{-a_i P_i}{P^2}\left(\frac{dP}{dt}\right)$$

The load relaxation is monitored using both a chart recorder (Figure A5.1), and a Commodore Pet computer linked to the load output, see programme below.

Programme:

```
 10     0 = 107*256: BY = 3276.8
 20     ADC = 0+53
 30     T = TI
 35     OPEN 4,4
 36     CMD 4
 40     IF TI < T GO TO 40
 50     SYS(ADC): V = USR(3)/BY
 60     SYS(ADC): U = USR(2)/BY
 61     MEAN = (INT(1E3*LDL+V)*.5/2))/1E3
 65     RT = (INT(1E6*(LDL-V)*.5/300))/1E6
 70     PRINT"LOAD = "V;"DISP = "U;"RATE = "RT; "kN/SEC"
        "MEAN = "MEAN; "kN"
 80     T = T+18000
 82     LDL = V
 90     GO TO 40
100     PRINT #4
110     CLOSE 4
READY
```

Readings at 1 minute intervals extracted from print out.

TIME (mins)	LOAD (volts)	ΔP (volts)	ΔP (kN)
0	4,02832		
1	4,01855	$9,77 \times 10^{-3}$	$4,885 \times 10^{-3}$
2	4,01367		
3	4,00879		
4	4,00391		
5	3,99902		
6	3,99902		
7	3,99902		
8	3,99414	$2,44 \times 10^{-2}$	$1,221 \times 10^{-2}$
9	3,99414		
10	3,98926		
11	3,98926		
12	3,98926		
13	3,98438		
14	3,98438		
15	3,98438	$9,76 \times 10^{-3}$	$4,880 \times 10^{-3}$
16	3,97461		
17	3,97461		
26	3,97461		
27	3,97461		
28	3,96973	$1,47 \times 10^{-2}$	$7,325 \times 10^{-3}$
32	3,96973		

Total ΔP = 4,02832-3,96973 = 0,05859 volts = 0,0293 kN in 30 minutes.

Calculation of da/dt;

$$\frac{da}{dt} = \frac{-a_i P_i}{P^2}\left(\frac{dP}{dt}\right)$$

$a_i = 120$ mm
$P_i = 2,014$ kN

(1) 0 - 1 min

$$\frac{da}{dt} = \frac{120\times10^{-3}\ 2,014}{(2,0117)^2}\left(\frac{4,855\times10^{-3}}{60}\right)$$

$$= 4,83\times10^{-6} \text{ m/sec}$$

$K_I = 4,495(2,0117)$
$= 9,043$ MNm$^{-3/2}$

(2) 16 - 28 min

$$\frac{da}{dt} = \frac{120\times10^{-3}\ 2,014}{(1,9885)^2}\left(\frac{7,33\times10^{-3}}{13\times60}\right)$$

$$= 5,74\times10^{-7} \text{ m/sec}$$

$K_I = 4,495(1,9885)$
$= 8,938$ MNm$^{-3/2}$

No account has been taken of the background elastic relaxation of the load system, but since the data that is obtained is very limited and, due to the very small load relaxation, unreliable, the method was abandoned early on in the investigation.

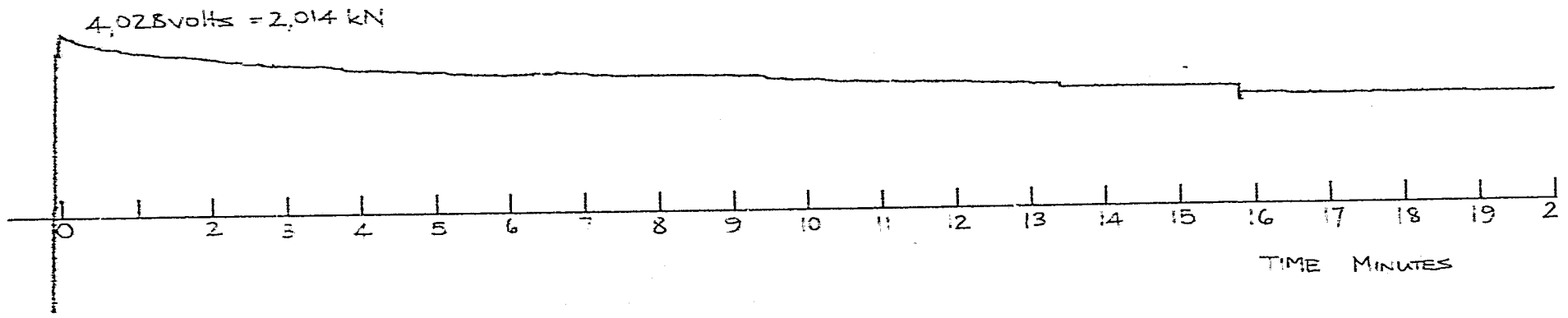

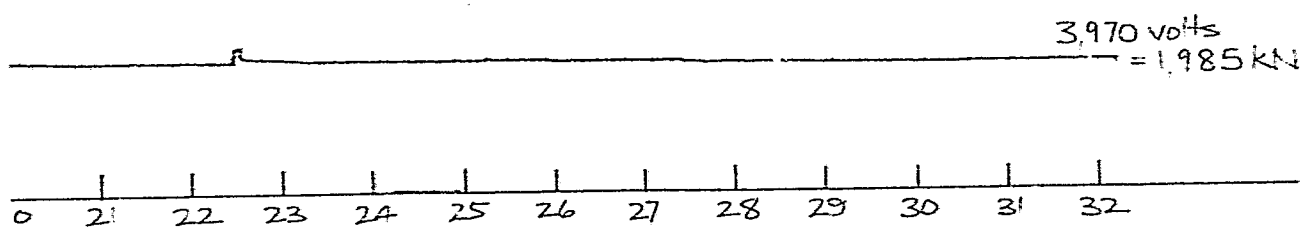

Figure A5.1 Load relaxation plot for Alloy S10, WC-10Co fine grained.
Total load decrease = 0,029 kN.

(ii) Fatigue crack growth

Crack growth rate measurement by testing under load control (fatigue load range constant) and monitoring specimen deflection (which in theory increases as the crack advances).

$$\frac{da}{dN} = \frac{1}{BP}\left(\frac{dy}{dN}\right)$$

a = crack length
y = specimen deflection
N = number of cycles
P = mean load
B = slope of compliance curve (dC/da) = $3W_m^2/Wd^3G$

W_m = loading moment
W = specimen width
l = specimen thickness
G = shear modulus = E/2(1 + ν)

E = elastic (Young's) modulus
ν = Poisson's ratio

Calculations

Alloy S10, WC-10Co fine grained
E = 550 GPa (Figure 2.14, Section 2.8.6)
ν = 0,22 (Figure 2.13, Section 2.8.6)

$$G = \frac{550\times10^9}{2(1+0,22)} = 225\times10^9 \text{ Nm}^{-2}$$

$$B = \frac{3(28,5\times10^{-3})2}{75,5\times10^{-3}(6,72\times10^{-3})^{3}(225\times10^{9})}$$

$$= 4,73\times10^{-7}\ N^{-1}$$

A compliance - crack length calibration has been obtained (Figure A5.2) and gives a B (dC/da) value of $6,5\times10^{-7}\ N^{-1}$ which is in reasonable agreement with the calculated value. These values should be compared to those reported by Williams and Evans[124] for 4130 steel ($dC/da = 1,59\times10^{-5}\ N^{-1}$) and Nadeau[143] for vitreous carbon ($dC/da = 2,34\times10^{-5}\ N^{-1}$). (Figure 3.15).

$$\frac{da}{dN} = \frac{1}{BP}\left(\frac{dy}{dN}\right)$$

$B = 4,73\times10^{-7}\ N^{-1}$

$P = 1,1\times10^{3}\ N$ (load range used = 0,1 to 2,1 kN)

$dy/dN = 1\times10^{-5}$ mm in 1170 cycles (Figure A5.3)

$= 8,55\times10^{-12}$ m/cycle

$$\frac{da}{dN} = \frac{8,55\times10^{-12}}{(4,73\times10^{-7})(1,1\times10^{3})}$$

$$= 1,64\times10^{-8}\ \text{m/cycle}$$

The actual value measured using dye penetrant is $7,30\times10^{-6}$ m/cycle. This gives an error of over 10^{2} in the crack growth rate determined by monitoring the displacement, using LVDT's.

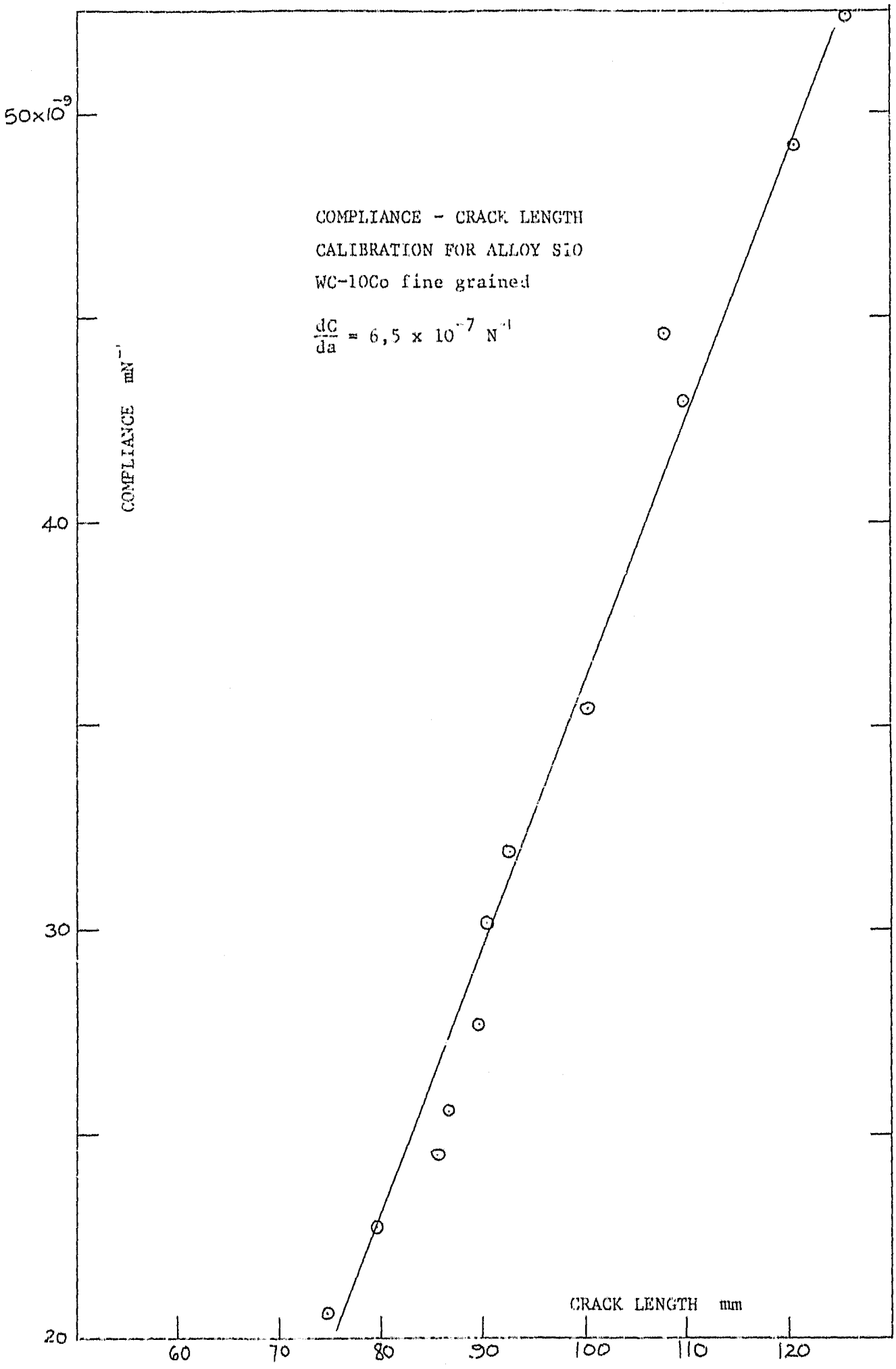
COMPLIANCE - CRACK LENGTH
CALIBRATION FOR ALLOY S10
WC-10Co fine grained
dC/da = 6,5 x 10⁻⁷ N⁻¹
COMPLIANCE mN⁻¹
50x10⁻⁹
40
30
20
CRACK LENGTH mm
60
70
80
90
100
110
120

Figure A5.2

Chart recorder scale = 0,5 mV/cms

LVDT scale = 0,5 mm/10 V

$\therefore$ 1 cms on chart = $2,5 \times 10^{-5}$ mm deflection of the specimen at the load points

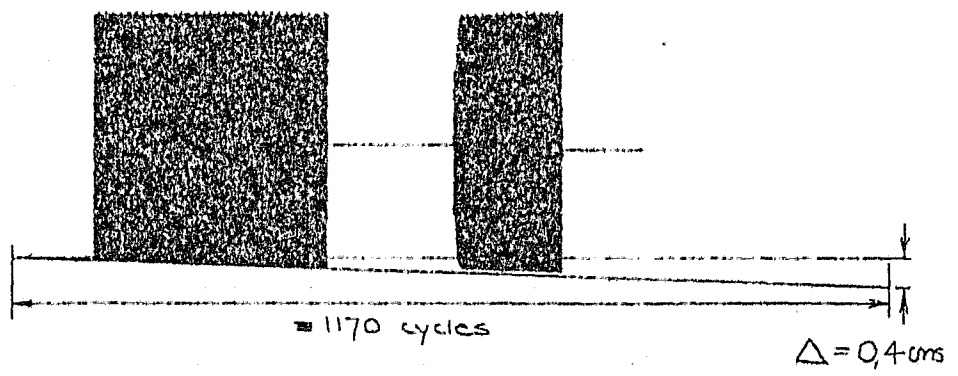

Chart recorder scale = 2 sec/mm

Frequency = 5 Hz

1 cms on chart = 100 cycles

Δ = 0,4 cms of vertical scale on the chart

$\Delta y = 2,5 \times 10^{-5}(0,4)$

$= 1,0 \times 10^{-5}$ mm

Figure A5.3

Chart recorder scale = 0,5 mV/cms

LVDT scale = 0,5 mm/10 V

$\therefore$ 1 cms on chart = $2,5 \times 10^{-5}$ mm deflection of the specimen at the load points

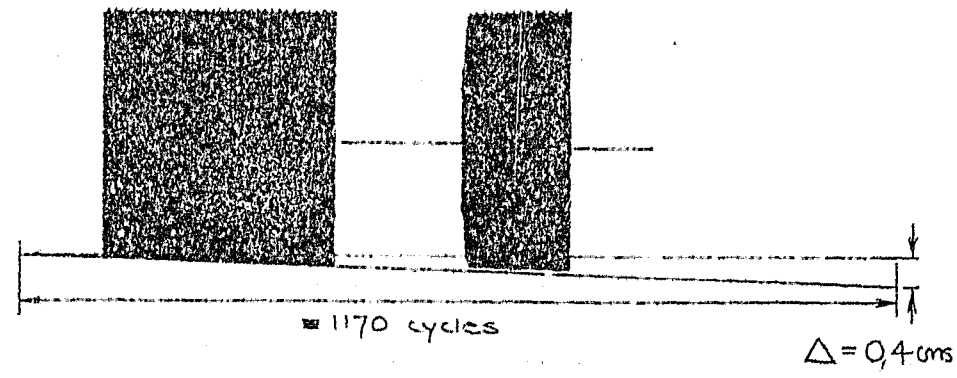

Chart recorder scale = 2 sec/mm

Frequency = 5 Hz

1 cms on chart = 100 cycles

Δ = 0,4 cms of vertical scale on the chart

$\Delta y = 2,5 \times 10^{-5}(0,4)$

$= 1,0 \times 10^{-5}$ mm

Figure A5.3

APPENDIX 6

Details of da/dN vs ΔK_I graphs for the six alloys tested at R ratio $\leq$ 0,1.

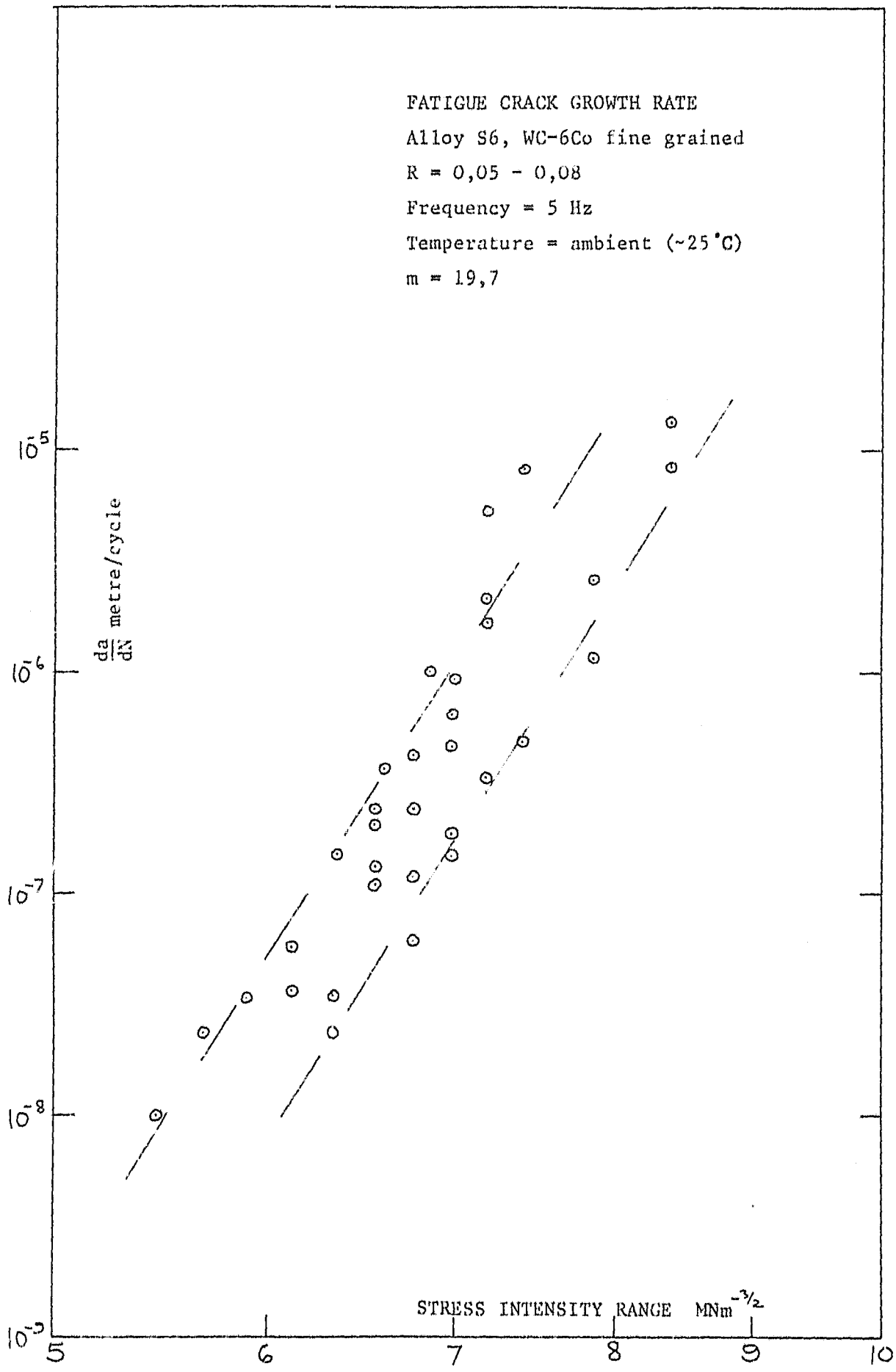
FATIGUE CRACK GROWTH RATE
Alloy S6, WC-6Co fine grained
R = 0,05 - 0,08
Frequency = 5 Hz
Temperature = ambient (~25°C)
m = 19,7
10^{-5}
10^{-6}
10^{-7}
10^{-8}
10^{-9}
$\frac{da}{dN}$ metre/cycle
5
6
7
8
9
10
STRESS INTENSITY RANGE MNm$^{-3/2}$

Figure A6.1

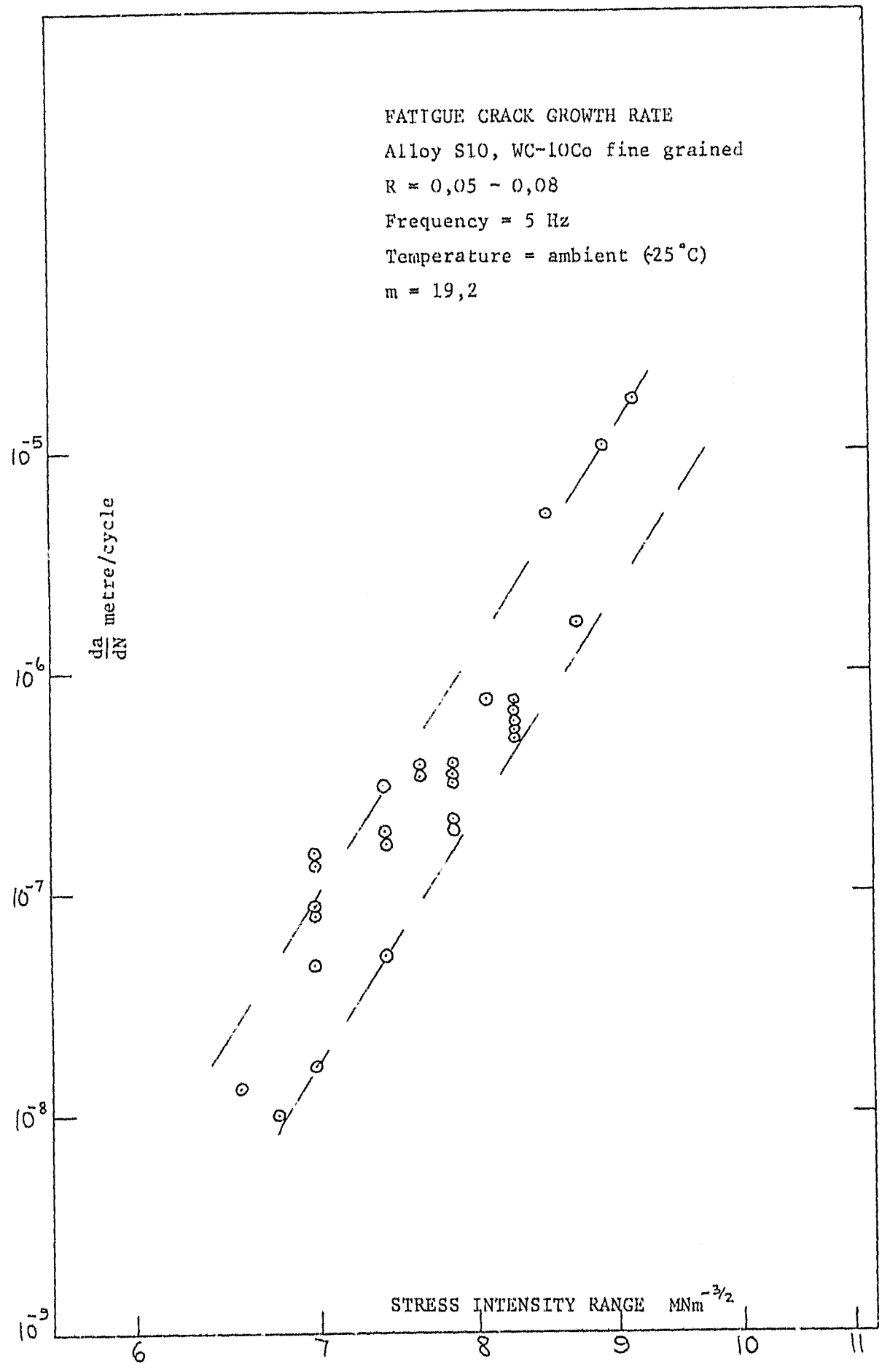
FATIGUE CRACK GROWTH RATE
Alloy S10, WC-10Co fine grained
R = 0,05 - 0,08
Frequency = 5 Hz
Temperature = ambient (25°C)
m = 19,2
da/dN metre/cycle
10^-5
10^-6
10^-7
10^-8
10^-9
STRESS INTENSITY RANGE MNm^-3/2
6
7
8
9
10
11

Figure A6.2

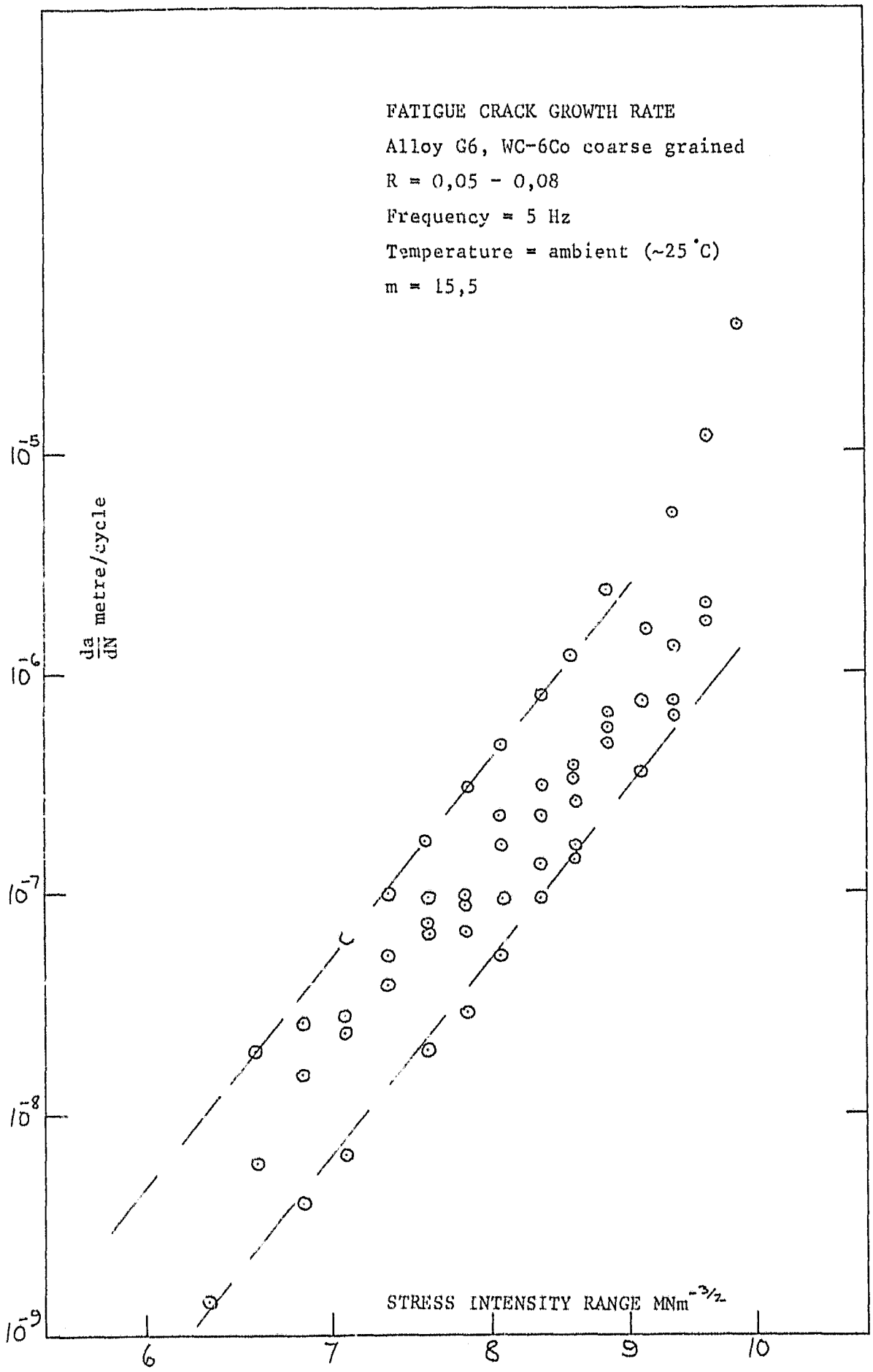
FATIGUE CRACK GROWTH RATE
Alloy G6, WC-6Co coarse grained
R = 0,05 - 0,08
Frequency = 5 Hz
Temperature = ambient (~25 °C)
m = 15,5
da/dN metre/cycle
10^-5
10^-6
10^-7
10^-8
10^-9
STRESS INTENSITY RANGE MNm^-3/2
6
7
8
9
10

Figure A6.3

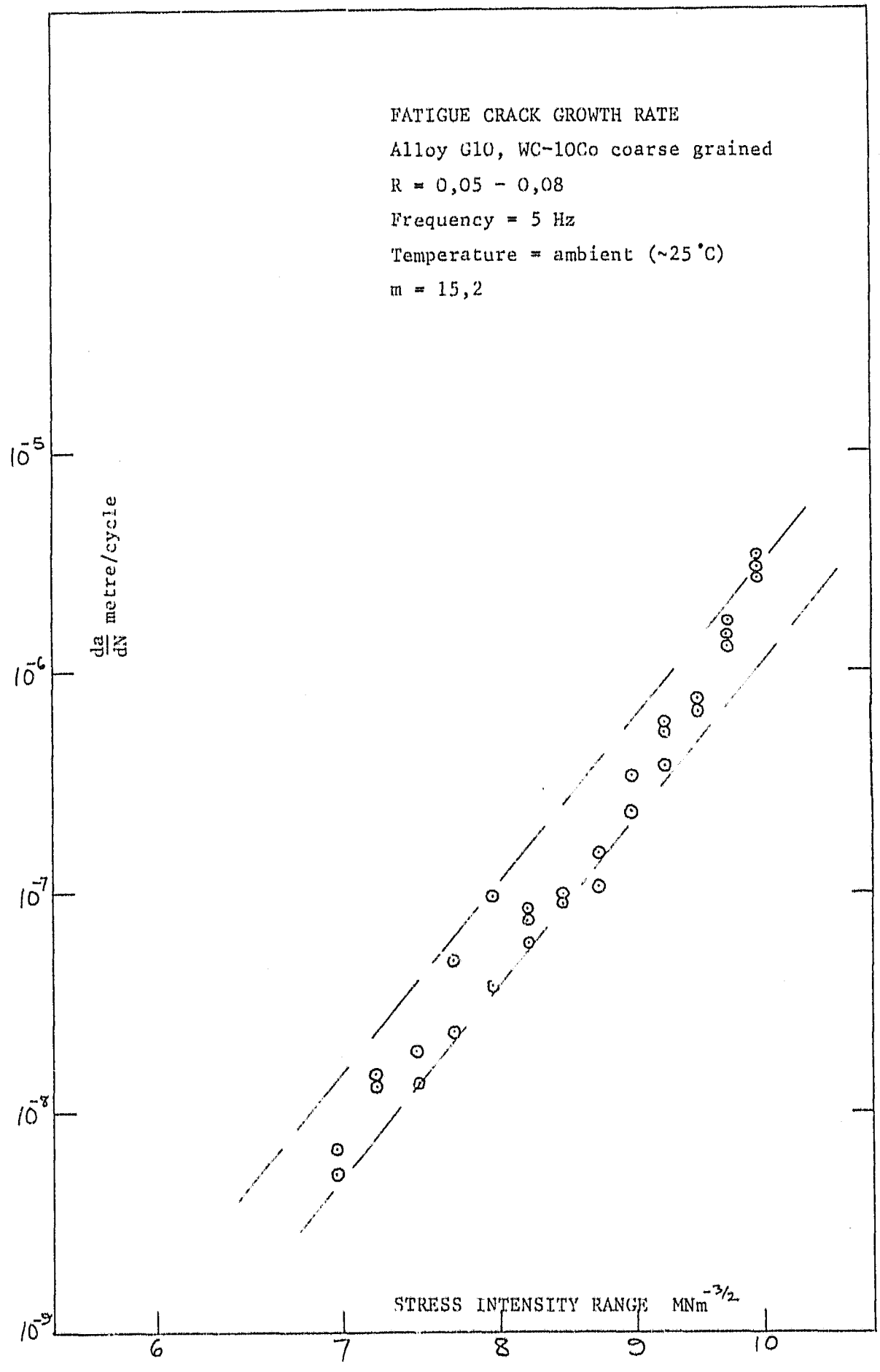
FATIGUE CRACK GROWTH RATE
Alloy G10, WC-10Co coarse grained
R = 0,05 - 0,08
Frequency = 5 Hz
Temperature = ambient (~25 °C)
m = 15,2
da/dN metre/cycle
10^-5
10^-6
10^-7
10^-8
10^-9
STRESS INTENSITY RANGE MNm^-3/2
6
7
8
9
10

Figure A6.4

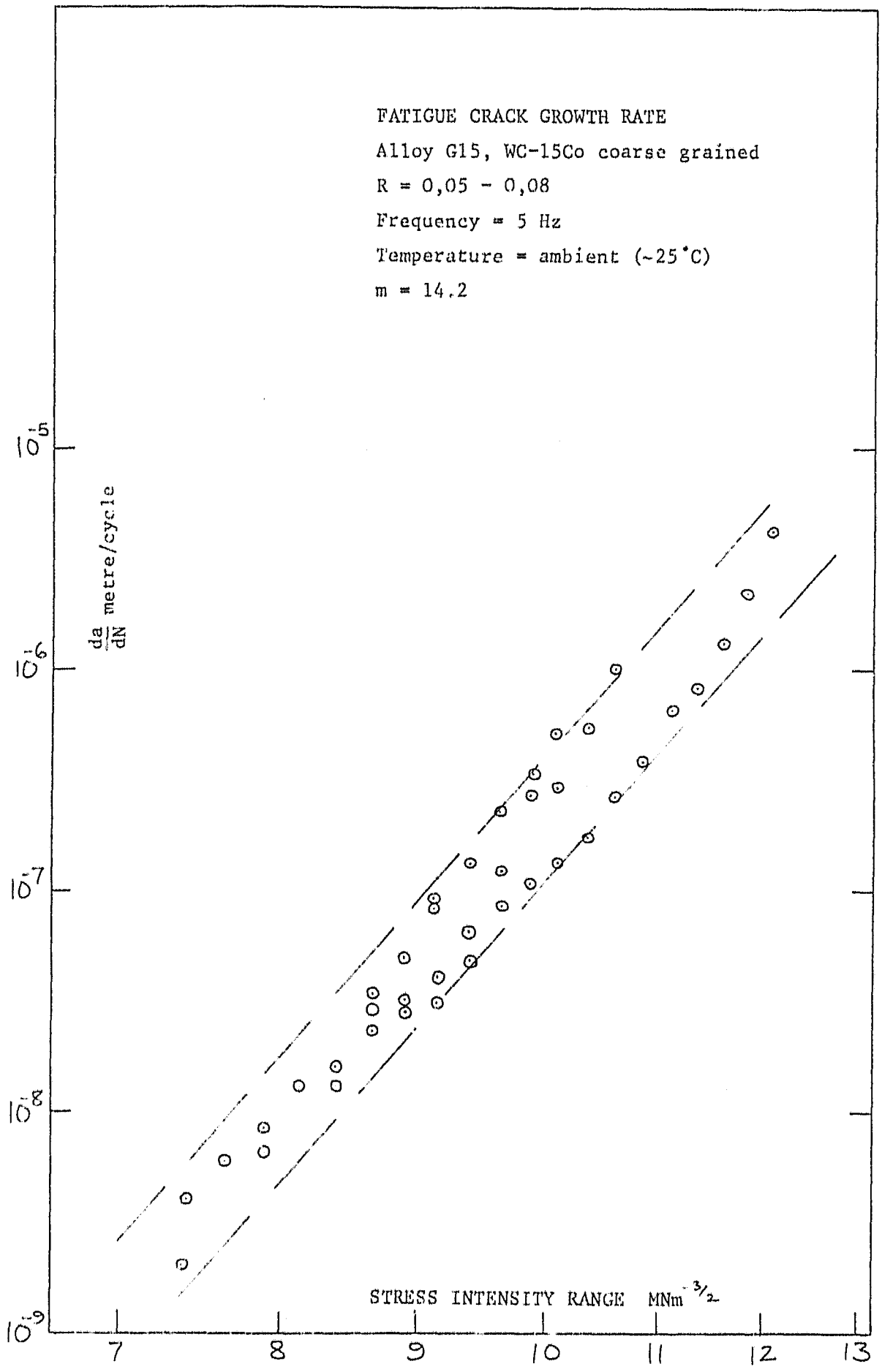
FATIGUE CRACK GROWTH RATE
Alloy G15, WC-15Co coarse grained
R = 0,05 - 0,08
Frequency = 5 Hz
Temperature = ambient (~25°C)
m = 14.2
10^{-5}
10^{-6}
10^{-7}
10^{-8}
10^{-9}
$\frac{da}{dN}$ metre/cycle
7
8
9
10
11
12
13
STRESS INTENSITY RANGE MNm$^{-3/2}$

Figure A6.5

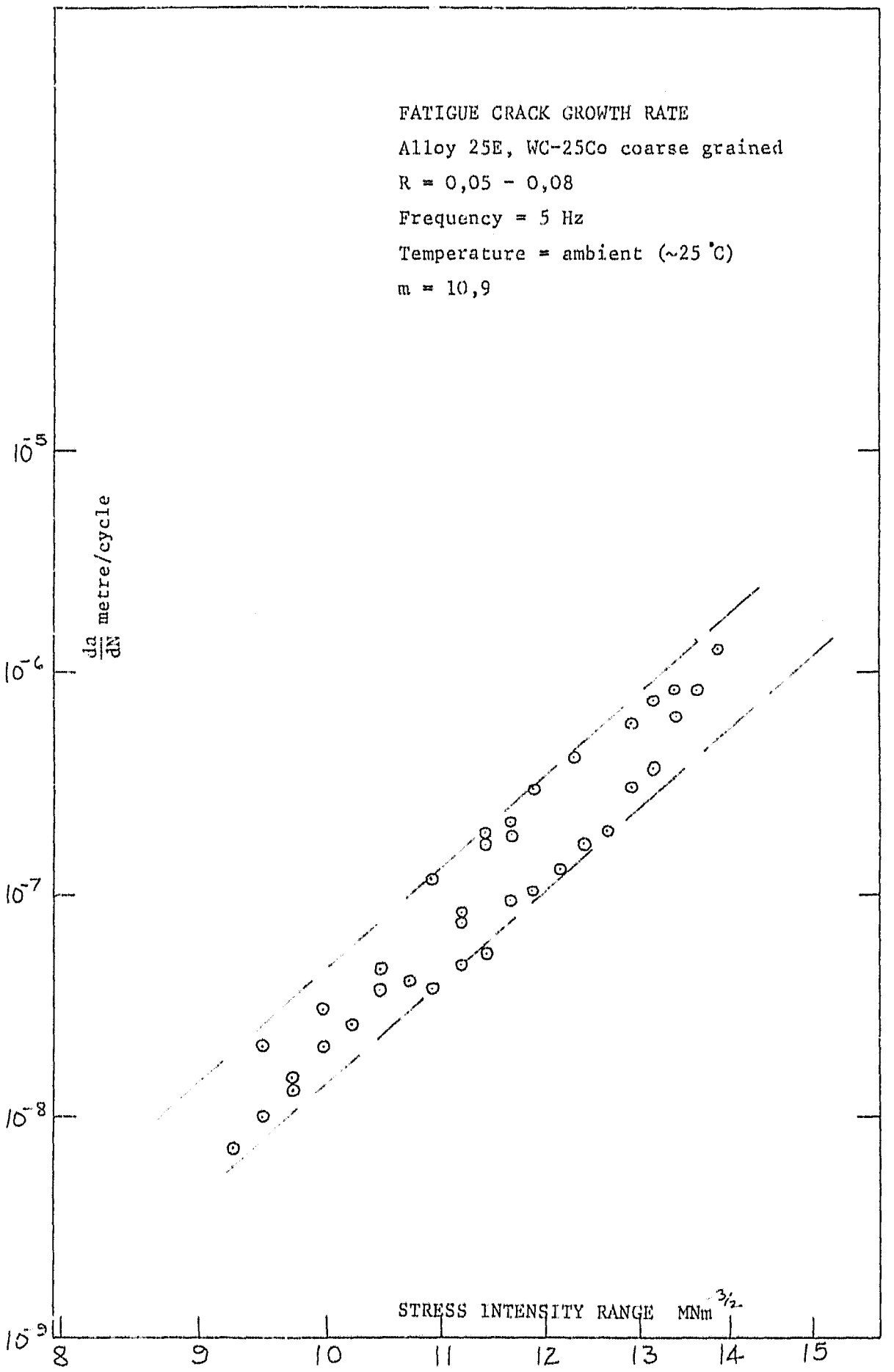
FATIGUE CRACK GROWTH RATE
Alloy 25E, WC-25Co coarse grained
R = 0,05 - 0,08
Frequency = 5 Hz
Temperature = ambient (~25 °C)
m = 10,9
10^{-5}
10^{-6}
10^{-7}
10^{-8}
10^{-9}
$\frac{da}{dN}$ metre/cycle
8
9
10
11
12
13
14
15
STRESS INTENSITY RANGE MNm$^{3/2}$

Figure A6.6